Transport in nanowire-based quantum dot systems: Heating electrons and confining holes

Dorsch, Sven

2022

Citation for published version (APA):
Dorsch, S. (2022). *Transport in nanowire-based quantum dot systems: Heating electrons and confining holes*. Department of Physics, Lund University.

Total number of authors:
1

LUND UNIVERSITY

PO Box 117
221 00 Lund
+46 46-222 00 00

Transport in nanowire-based quantum dot systems: Heating electrons and confining holes

SVEN DORSCH
DIVISION OF SOLID STATE PHYSICS | FACULTY OF ENGINEERING | LUND UNIVERSITY

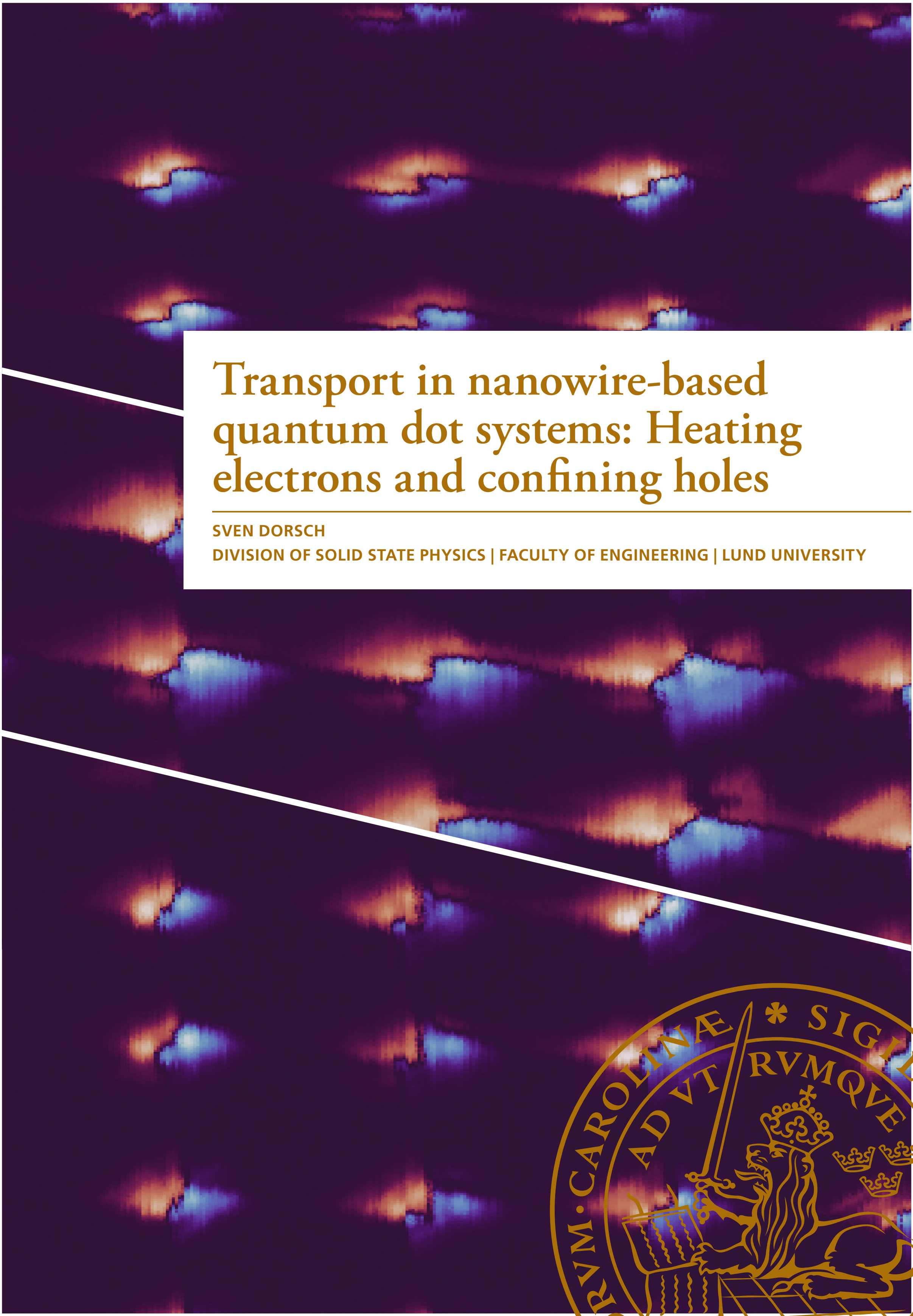

Transport in nanowire-based quantum dot systems: Heating electrons and confining holes

Transport in nanowire-based quantum dot systems: Heating electrons and confining holes

by Sven Dorsch

LUND
UNIVERSITY

DOCTORAL THESIS
To be publicly defended, with the permission of the Faculty of Engineering, Lund University, on Friday, the 17th of June, 9:15 am in the Rydberg lecture hall (Rydbergsalen) at the Department of Physics.

Thesis advisors
Associate Professor Adam Burke and Associate Professor Claes Thelander

Faculty opponent
Associate Professor Natalia Ares
University of Oxford, United Kingdom

Organization **LUND UNIVERSITY**	Document name **DOCTORAL DISSERTATION**
Department of Physics Box 118 SE–221 00 LUND Sweden	Date of disputation 2022-06-17
Author(s) Sven Dorsch	Sponsoring organization

Title and subtitle

Transport in nanowire-based quantum dot systems: Heating electrons and confining holes

Abstract

Quantum dots embedded in an electronic circuit allow precise control over the charge transport behaviour of the system: Charge carriers can be individually trapped or precisely shuffled between a series of quantum dots in a strictly sequential manner. This introduces ideal conditions to study fundamental quantum physics and such devices are in the focus of extensive efforts to develop quantum information related applications. This thesis contributes to the development of model systems enabling control of, and abiding by quantum mechanical effects. The aim of the model systems is to search and use advantages compared to devices governed purely by the laws of classical physics.

In this thesis, transport phenomena in n- and p-type III-V semiconductor nanowire quantum dot systems are explored. First, the concepts necessary to build an understanding of charge transport across quantum dot systems, namely quantum confinement in nanostructures and Coulomb blockade, are introduced. Next, the principles of transport across single and double quantum dot devices are discussed and various experimental device designs are presented. The experimental work falls into two separate research directions and the thesis includes three published papers, which are put into context and supplemented with additional experimental results.

Paper I characterizes the properties of p-type GaSb nanowires to assess the material's applicability for the realization of spin-orbit qubits as fundamental building blocks of solid state quantum computers. Experimentally, g-factors and the spin-orbit energy are determined and fabricational challenges for the realization of serial double quantum dot devices are discussed and overcome.

Papers II and III study thermally driven currents in InAs nanowire double quantum dots, where heat is essentially converted to electrical power. Such nanoscale energy harvesters operate in a regime where fluctuations are highly relevant and give insights into fundamental nanothermodynamic concepts. Thermally induced currents in double quantum dot devices are the result of three-terminal phonon-assisted transport or the two-terminal thermoelectric effect. Paper II studies the interplay of the two effects, the relevance of the interdot coupling and the impact of excited states. Paper III develops a versatile device architecture which combines bottom-gating and heating and enables the localized application of heat along the nanowire axis. Such devices provide ideal, controlled conditions for future studies of fundamental nanothermodynamics.

Key words

nanowire, quantum dot, double quantum dot, thermoelectric effect, phonon-assisted transport, GaSb, g-factor

Classification system and/or index terms (if any)		
Supplementary bibliographical information		Language English
ISSN and key title		ISBN 978-91-8039-197-9 (print) 978-91-8039-198-6 (pdf)
Recipient's notes	Number of pages 160	Price
	Security classification	

I, the undersigned, being the copyright owner of the abstract of the above-mentioned dissertation, hereby grant to all reference sources the permission to publish and disseminate the abstract of the above-mentioned dissertation.

Signature S. Date 2022-05-20

Transport in nanowire-based quantum dot systems: Heating electrons and confining holes

by Sven Dorsch

Division of Solid State Physics
Department of Physics
Faculty of Engineering
Lund University

Cover illustration front: Thermally driven currents across a bottom-heated serial double quantum dot, heated on the left/middle/right. Experimental details are given in paper III.

Faculty of Engineering, Department of Physics
Lund University, Lund, Sweden

ISBN: 978-91-8039-197-9 (print)
ISBN: 978-91-8039-198-6 (pdf)

Printed in Sweden by Media-Tryck, Lund University, Lund 2022

NORDIC SWAN ECOLABEL
Printed matter
3041 0903

Media-Tryck is a Nordic Swan Ecolabel
certified provider of printed material.
Read more about our environmental
work at www.mediatryck.lu.se

MADE IN SWEDEN

Art is how we decorate space;
Music is how we decorate time.
— Jean Michel Basquiat

Appreciate your time and the artist…
… by listening with quality headphones!

Contents

Abstract

Quantum dots embedded in an electronic circuit allow precise control over the charge transport behaviour of the system: Charge carriers can be individually trapped or precisely shuffled between a series of quantum dots in a strictly sequential manner. This introduces ideal conditions to study fundamental quantum physics and such devices are in the focus of extensive efforts to develop quantum information related applications. This thesis contributes to the development of model systems enabling control of, and abiding by quantum mechanical effects. The aim of the model systems is to search and use advantages compared to devices governed purely by the laws of classical physics.

In this thesis, transport phenomena in n- and p-type III-V semiconductor nanowire quantum dot systems are explored. First, the concepts necessary to build an understanding of charge transport across quantum dot systems, namely quantum confinement in nanostructures and Coulomb blockade, are introduced. Next, the principles of transport across single and double quantum dot devices are discussed and various experimental device designs are presented. The experimental work falls into two separate research directions and the thesis includes three published papers, which are put into context and supplemented with additional experimental results.

Paper I characterizes the properties of p-type GaSb nanowires to assess the material's applicability for the realization of spin-orbit qubits as fundamental building blocks of solid state quantum computers. Experimentally, g-factors and the spin-orbit energy are determined and fabricational challenges for the realization of serial double quantum dot devices are discussed and overcome.

Papers II and III study thermally driven currents in InAs nanowire double quantum dots, where heat is essentially converted to electrical power. Such nanoscale energy harvesters operate in a regime where fluctuations are highly relevant and give insights into fundamental nanothermodynamic concepts. Thermally induced currents in double quantum dot devices are the result of three-terminal phonon-assisted transport or the two-terminal thermoelectric effect. Paper II studies the interplay of the two effects, the relevance of the interdot coupling and the impact of excited states. Paper III develops a versatile device architecture which combines bottom-gating and heating and enables the localized application of heat along the nanowire axis. Such devices provide ideal, controlled conditions for future studies of fundamental nanothermodynamics.

Popular science summary

The era of computers began with the invention and development of transistors in the late 1940s. Today, transistors are the elementary building block of computers and great efforts are aimed at increasing the computational power by squeezing more and more transistors into the same area. In recent years, however, the trend has shifted from plain power increases to the development of new computation concepts. Many new approaches are closely linked to novel materials and the use of quantum effects. A key ingredient to the realization of a new generation of electronic devices is understanding the physics and underlying processes in the limit of tiny device dimensions. Here, this thesis contributes through studies of how current flows through tiny semiconductor segments.

Semiconductors are a type of material where the ability to conduct current can be manipulated — a principle that is used in modern transistors. In this thesis, tiny semiconductor segments with dimensions as small as a billionth of a meter, 10000 times smaller than the diameter of a human hair, are embedded in an electronic circuit. Within such structures, current flow obeys different rules compared to macroscopic conductors. Current flow, on a basic level means transporting charge. Charge is carried by electrons, which are elemental particles, essentially turning current flow into a stream of electrons.

In regular transistors, current through a semiconductor channel is controlled via a voltage applied to a so-called gate electrode. Translating this to a simple picture, we can think of a broad tunnel with a constant stream of people passing through. Changing the voltage on the gate electrode, in that picture could be translated to slowly closing a physical gate within the tunnel. The more closed the gate is, the less people can pass the tunnel at a time, but a description of the human current requires only an understanding of the crowd dynamics. This changes drastically if we introduce a paternoster, significantly confining the available area to move. Here, suddenly the nature of individual people becomes relevant. Once a person steps onto a lift car, no second will follow, respecting the concept of personal space. In order for the next person to enter, this repelling force has to be overcome, which can for instance be achieved by moving the paternoster downward, making the next lift car available.

In the same way we experience the concept of personal space, electrons are charged and thus experience the so-called Coulomb repulsion, a repelling force. Within the limited space of a tiny semiconductor segment or quantum dot, electrons cannot avoid one another and the nature of individual electrons dominates the current through the quantum dot. Only one electron at a time can enter the quantum dot and in order for the next electron to enter the segment enclosed by the metallic contacts, the first electron either has to leave or energy must be added to the system. Energy can be added to the system via the gate electrode.

The devices studied in this thesis contain two quantum dots directly connected in series. In our simple analogy, this translates to the rather unusual situation of two paternosters that have to be passed in series in order to move forward. Here, my role as a scientist mirrors that of the paternoster operator, who can precisely control the motion, position and number of electrons in these devices by aligning or detuning the metaphorical lift cars against each other via tuning voltages on gate electrodes. Based on the above described, so-called serial double-quantum dot, model system this thesis presents results on two separate topics.

The first topic makes use of the ability to precisely trap individual electrons in the lift cars of such serial double quantum dot devices. This allows scientists to look closely and study, even control the behavior of individual electrons — a concept applicable for quantum computation: Electrons possess a quantum mechanical property, the so-called spin, which at its essence means that electrons behave like tiny bar magnets. The orientation of the poles of these bar magnets can be used to encode information and by controlled rotation of the magnet‘s orientation computations can be performed. Such devices are then called spin qubits and form one approach to design the basic building block of a quantum computer. In a classical computer, information is encoded in two states, described by 0 or 1. In contrast, spin qubits can essentially take a continuum of states, where each state describes a certain rotation of the magnetic poles of the electron‘s spin. Consequently, a quantum computer running clever algorithms which make use of this continuous range of available states can solve selected problems significantly faster compared to traditional computers.

A challenge for the practical realization of a spin qubit is that the precise orientation of the electron’s magnetic orientation must remain fixed during computational processes. In many common materials, however, a variety of other bar magnets are present which interact with the electron’s spin. This unwanted interaction results in the uncontrolled rotation of the electron spin. One approach to tackle this problem is based on making use of materials where instead of electrons, vacancies of electrons, so-called holes contribute to the current flow. Holes much like electrons possess a spin, but in contrast to electrons interact less with other spins in the qubit’s host material. In this thesis, I study GaSb, a compound semiconductor material where holes carry the current. I develop suitable device designs for the realization of a GaSb spin qubit and test if the material’s properties are suitable for quantum computation.

The second research topic discussed in this thesis evolves around converting heat to currents in serial double quantum dot devices. Conventionally, electrons obtain their incentive to travel from one end of the device to the other by the application of an external voltage bias. Whether current can flow or not then depends on how the metaphorical lift cars of the two paternosters or quantum dots are positioned relative to each other. In this thesis, I study currents that are driven by local heating of the device rather then by the application of an external voltage bias.

I therefore develop device designs where tiny electrical heaters are placed on different locations along the serial double quantum dot device. Then, I identify for which lift car configurations heat driven currents, so-called thermocurrents, can flow across the device. Here, I find two effects that contribute to the thermocurrents: First, if a temperature difference within the electronic circuit of the device exists, electrons gain incentive to travel through aligned lift cars between the two quantum dots in an attempt to even out the temperatures. Second, if the surroundings of the device is hotter than the electronic circuit itself, electrons climb through misaligned lift cars and cool the environment in the process. Because both processes essentially convert heat to current, which could be used to for instance charge a battery, the devices discussed in this thesis can be seen as tiny engines which produce electrical power. Because in the here discussed quantum dot-based devices researchers have tremendous control over the current by tuning the positions of the metaphorical lift cars, these tiny engines offer an ideal experimental playground to study fundamental concepts that are otherwise only discussed theoretically.

List of publications

This thesis is based on the following publications, referred to by their Roman numerals:

I **Gate control, g factors and spin orbit energy of p-type GaSb nanowire quantum dot devices**
Sven Dorsch, In-Pyo Yeo, Sebastian Lehmann, Kimberly Dick, Claes Thelander, and Adam Burke
Physical Review B 103, L241411 (2021)

I fabricated the samples, performed the measurements and analyzed the data. I wrote the manuscript with input from all co-authors.

II **Heat Driven Transport in Serial Double Quantum Dot Devices**

Sven Dorsch, Artis Svilans, Martin Josefsson, Bahareh Goldozian, Mukesh Kumar, Claes Thelander, Andreas Wacker, and Adam Burke
Nano Letters 21, 988-994 (2021)

I performed the measurements, analyzed the data and wrote the majority of the manuscript with input regarding theoretial calculations from Andreas Wacker.

III **Characterization of electrostatically defined bottom-heated InAs nanowire quantum dot systems**
Sven Dorsch, Sofia Fahlvik, and Adam Burke
New Journal of Physics 23, 125007 (2021)

I planned the experiments, fabricated the device, performed the measurements and analyzed the data. I wrote the manuscript with input from all co-authors.

The following publications are relevant but not included in this thesis:

Side-gated, enhancement mode, InAs nanowire double quantum dot devices – toward controlling transverse electric fields in spin-transport measurements
Sven Dorsch, Bekmurat Dalelkhan, Sofia Fahlvik, and Adam Burke
Nanotechnology 30, 144002 (2019)

Acknowledgements

At this point in time, I have spent around 17% or five years of my life on my PhD studies. When spending that much time on a single project I suppose it may be easy to have regrets. Looking back at my own time at FTF, however, I immediately recall many good memories and struggle to pinpoint the bad days. PhD studies certainly come with tough times and thus my fondness of the journey goes to be a testemony of the incredibly friendly, supportive and enjoyable working environment which I have had the privilege to experience at FTF and NanoLund. This great working environment is much owed to the many people who actively contribute to the day-to-day life at FTF and I would like to express my gratitude to everyone who supported me in one way or another along the way.

First and foremost, PhD studies stand and fall with the thesis advisors. I thus want to say thank you to my main supervisor Adam Burke! Without you none of this work would have been possible and whatever I write here will certainly not do your contribution to this thesis justice. Throughout the years, your door was always open and I truly appreciate your trust and our discussions about science and other topics. Your methodic, calm and detail oriented approach to research has had a big influence on my work and I will always be amazed by your immense technical knowledge. We may not always have known what exactly we were working to achieve, but at the end of the day we had fun and without your continued support the past five years would have been considerably less successful!

I also want to thank my co-supervisor Claes Thelander. You may not think that you contributed much to the success of this thesis, but I know that my work has improved a lot due to your support. You have always made room in your schedule when I wanted to discuss science and I truly appreciate your comments and advice, both big and small. It is easy to get lost in all the exciting possibilities of research and your encouragement to also reflect on the limitations of research work have shaped my own approach to science for the better!

Supervisors aside, I was lucky to collaborate with many brilliant people throughout my PhD studies. I would like to specifically thank Martin Josefsson for introducing me to the world of nanoscale energy harvesting and finding the best equations. I also am indebted to my collaborators in past as well as in ongoing projects, Artis Svilans, Andreas Wacker, Ville Maisi, Simon Wozny, In-Pyo Yeo, Heiner Linke and many others who have directly and indirectly contributed to my research output. None of my work would have been possible without excellent nanowire growth and I would therefore like to extend my thanks to Sebastian Lehmann, Sofia Fahlvik, Mukesh Kumar and Kimberly Dick in Lund as well as the Sorba group in Pisa for supplying an endless stock of nanowires. My sincere gratitude also goes to all the technical and administrative staff at FTF and NanoLund without whom our research efforts would run considerably less smoothly.

I want to further thank all fellow PhD students, post docs, professors and other staff at

FTF. In my opinion it is a combination of the different personalities and cultures as well as the approachable and welcoming spirit at FTF that made my time so enjoyable! Thank you Dan Hessmann, our fearless and often funny leader. You may be the only person to ever chase me through the hallway just to say hello and I believe this occurrence sums up why FTF is a great place to be at. I was also fortunate enough to have the best office mate whom I get to share custody of our plants with. Thank you Jonatan!

Finally, I want to thank my colleagues Lukas, Jonatan, Irene, David B, Oskar and David A in the extended H corridor. During the past five years, you have become great friends and I hope we will get to go on many more adventures together in the future!

Introduction

My comrade caught me when I was
working empty-handed in the air
with microscopes over my eyes,
and wanted to run after the doctor.
– Microhands by B. Zhitkov [1]

In modern day popular culture, nanotechnology quite often finds itself portrayed as highly-futuristic, often dangerous or almost magical technology (see Moonfall (2022)[1], Bond (2021)[2], Spectral (2016)[3], Transcendence (2014)[4]) that is far out of reach of today's state of the art. In reality, nanotechnology has already today silently made its way into modern day life with existing applications ranging from electronics, most notably the miniaturization of transistors which drives the computational power increases of processors, to water-repellent coatings, sensors or medical applications. At its core, nanoscience and nanotechnology aim to explore, design and functionalize systems with dimensions as small as a billionth of a meter and build upon an understanding of the vastly changing properties of materials when the dimensions are reduced to the nanoscale [2].

Much of our insights into the different opto-electronic properties of nanoscale structures when compared to bulk materials date back to the early 20th century and the fundamental idea of wave-particle duality [3] — a concept central to today's interpretation of quantum mechanics. The rapid progress in the understanding of the principles of quantum mechanics, sometimes deemed the first quantum revolution [3], has led to many technological advancements. With drastic improvements to nanofabrication capabilities at the turn of the 21st century, however, a new trend away from purely using the fundamentals of quantum mechanics to explain and search for materials and systems with suitable properties has emerged in nanoscience, heralding what can be called the second quantum revolution [3].

---

[1] Nano-bots fuelled by artificial intelligence knock the moon out of its orbit and cause it to fall onto earth

[2] No time to die: Weaponized nano-bots target specific DNA markers

[3] Bose-Einstein condensate gone wild.. really, I do not know what is going on there

[4] A scientists consciousness is uploaded to a quantum computer and nano-bots remote control humans

Instead of working around quantum effects, clever device designs are now employed to actively use and control quantum effects. Ultimately, this branch of nanotechnology pursues the ability to engineer artificial material properties and push towards novel applications beyond the boundaries of classical physics.

Here, this thesis comes in and aims to contribute to the development and characterization of model systems where quantum effects are relevant. The systems discussed in this work are designed to search for and use advantages arising from quantum effects compared to devices governed purely by the laws of classical physics. Specifically, charge transport across quantum dot (QD) systems in n- and p-type III-V semiconductor nanowires are considered. Such QDs are electrically insulated, small semiconductor segments embedded in an electronic circuit. As a consequence of the quantization of charge, Coulomb interactions and confinement of the charge carrier's wave function [4], QD systems allow charge carriers to be trapped or shuffled between a series of QDs in a strictly sequential manner [5, 6]. Thus, this principle gives precise control over individual charge carriers and QD systems are an ideal platform to study fundamental quantum physics and to build applications thereon.

One such application is the development of quantum bits or qubits [7], which in contrast to classical bits can not only exist in the boolean states 0 and 1 but also a continuum of intermediate, so-called superposition states [8]. As a result, qubits can tackle complex problems out of reach for conventional computers. The spin of single charge carriers confined to a serial double quantum dot (DQD) has been proposed as a platform for the experimental realization of a qubit by Loss and DiVincenzo in 1998 [9]. Here, nanowires bring favourable properties that allow fast, all-electrical spin manipulation [10] and p-type systems are further beneficial because of an increase in the spin's coherence time as a result of a reduced hyperfine interaction with the surrounding nuclear spins [11]. This thesis contributes to the field by characterizing p-type GaSb nanowires with respect to the material properties necessary for the realization of spin-orbit qubits and the development of suitable double quantum dot device architectures.

In conventional transport studies on QD devices, electrons obtain their incentive to travel across the device from a voltage bias applied between two electrical contacts on either side of the QD system. In contrast, the second model system developed in this thesis aims to deliver a comprehensive description of transport across a DQD, driven by temperature differences between different parts of the device. This situation is achieved by the introduction of local Joule heater electrodes. Thermally induced transport across DQDs is interesting for a variety of reasons. First, the ability to drive currents by an external heat source allows operation of the device as an energy harvester, converting waste heat into useful electrical power [12]. Conversely, this also implies the ability for active cooling of for example a quantum electronic circuit [13]. Finally, nanoscale devices coupled to their thermal environment give access to a regime where fluctuations are highly relevant and together with quantum effects govern the properties of the device. For conceptually comparable systems, so called thermodynamic uncertainty relations, describing an interplay between energy dissipation and current fluctuations, have been predicted to give insight into non-equilibrium behaviours [14]. Because boundaries described by thermodynamic uncertainty relations are often derived based on the principles of classical physics, violations would directly link to quantum effects and enable the definition of a quantum advantage.

Three published and peer-reviewed papers are included in this thesis, which aims to introduce and put the experiments presented therein into context. The thesis is organized as follows: First, in the remainder of this introduction, sections 1 and 2 describe the concepts of quantum confinement of charge carriers in nanostructures as well as the Coulomb blockade effect. With the help of these concepts the principles of charge transport across single- and serial double quantum dots are qualitatively derived in section 3 and quantified via rate equations in section 4. The design considerations and fabrication techniques for the devices in this thesis are introduced in sections 5 and 6. Sections 7 and 8 present the experimental results of paper I, associated with the characterization and development of p-type GaSb nanowire quantum dot devices. The results of papers II and III, where thermally induced currents across serial double quantum dots and suitable heater architectures are studied, are summarized in section 9. Finally, section 10 gives an outlook and introduces experiments where thermodynamic uncertainty relations are probed with quantum-dot based energy harvesters.

1 Low dimensional systems - from 3D to 0D

As humans, we perceive the world and our surrounding space as three-dimensional and as a result the concept of lower dimensional, especially zero-dimensional, objects may not be obvious to the unfamiliar reader. In the context of solid-state physics, the dimensionality of a system is classified according to the number of spatial directions along which particles can travel freely. A reduction of the dimensionality by confining the free electron or hole motion in one or more spatial directions results in altered opto-electronic properties and the understanding and application of that principle is at the core of modern semiconductor technology. The origin of the altered properties of lower dimensional systems compared to bulk is found within quantum mechanics and this section aims to introduce briefly the physics of low dimensional semiconductors from three- to zero-dimensions. The following chapter is based on the description in ref. [15] with additional input from refs. [16, 17].

Understanding of how free charge carriers, electrons or holes, in a solid-state system experience their environment requires a description of the interactions of the charge carriers and their host system. Such systems are described by the laws of quantum mechanics according to which all particles are, in addition to their particle nature, also associated with a wave nature a wavelength described by the de Broglie relation $\lambda_{\mathrm{dB}} = h/p$ [18]. Here, p is the particle's momentum and h denotes Planck's constant. This wavelength λ_{dB} is usually in the range of tens of nanometers for valence electrons in semiconductors at the Fermi-energy [18, 19]. The de Broglie wavelength allows to make a first estimate of whether the charge carriers experience their surroundings as three- or lower-dimensional. For systems with one or more spatial dimensions in the order of or smaller than λ_{dB}, charge carriers are subjected to quantum confinement effects which limit their freedom of motion and they experience their world as low-dimensional. In contrast, in bulk systems where all spatial dimensions are large compared to λ_{dB} the charge carriers are subjected to a seemingly infinite ionic lattice, which allows them to move freely.

Electrons in bulk crystals

In order to understand confinement effects, first the electronic behaviour of bulk solid-state systems must be considered. Even in bulk systems, free electrons are not unconstrained but bound by the laws of quantum mechanics. A complete description entails studying the cloud of valence electrons in the ionic lattice of the solid-state crystal. Such systems are described by the many-body wave function $\Phi(\{\vec{r}_i\}, \{\vec{R}_j\})$, where $\{\vec{r}_i\}$ denote the coordinates of valence electrons and $\{\vec{R}_j\}$ of ions. Solutions to the time independent Schrödinger equation

$$\hat{\mathrm{H}}\Phi(\{\vec{r}_i\}, \{\vec{R}_j\}) = \mathrm{E}\Phi(\{\vec{r}_i\}, \{\vec{R}_j\}) \tag{1}$$

then yield information about the steady-state energy spectrum of the system, a quantity that is relevant for the description and explanation of many opto-electronic properties. Here, $\hat{\mathrm{H}} = \hat{\mathrm{H}}_{\mathrm{e}} + \hat{\mathrm{H}}_{\mathrm{ion}} + \hat{\mathrm{H}}_{\text{e-ion}}$ is the many-body Hamiltonian and E the total energy of the system. The Hamiltonian contains contributions of the kinetic and potential energy of the system and describes the interactions within the valence electron cloud ($\hat{\mathrm{H}}_{\mathrm{e}}$), the ionic system ($\hat{\mathrm{H}}_{\mathrm{ion}}$) and the electron-ion interactions ($\hat{\mathrm{H}}_{\text{e-ion}}$). Solving the Schrödinger equation for the many-body wave functions and energy, however, is a highly complex problem which cannot be treated exactly and requires approximations.

The Born-Oppenheimer approximation [20] uses the fact that ions have a significantly higher mass compared to electrons and allows adiabatic decoupling of the electronic from the ionic system. This approximation reduces the problem to a many-electron system in an effective ionic potential. Whilst simplified, the many-electron Schrödinger equation can still not be solved exactly and thus, in an additional mean-field approximation, only a single electron in a potential $\mathrm{V}(\vec{r})$ is considered. Instead of solving complex many-body interactions, the single-particle potential $\mathrm{V}(\vec{r})$ combines the average effects of all ions as well as the evenly distributed valence electron cloud, which act on the electron under consideration. This single-particle picture remains sufficient to qualitatively describe the electronic properties of a bulk solid-state system as well as alterations introduced by confinement effects and provides a suitable knowledge base to discuss the later-introduced experimental system and results in this thesis.

The single-electron Schrödinger equation reads

$$\hat{\mathrm{H}}_{1\mathrm{e}}\phi_\nu(\vec{r}) = \left[-\frac{\hbar^2\Delta}{2m} + \mathrm{V}(\vec{r})\right]\phi_\nu(\vec{r}) = \mathrm{E}_\nu\phi_\nu(\vec{r})\ , \tag{2}$$

where $\hbar = h/(2\pi)$ is the reduced Planck's constant, m the electron mass and ν represents a quantum number, indexing bands in the systems bandstructure, and is now solvable for the single-electron wave functions $\phi_\nu(\vec{r})$ and energies E_ν. Because $\mathrm{V}(\vec{r})$ describes a periodic lattice, it mirrors the crystalline translation symmetry $\mathrm{V}(\vec{r}) = \mathrm{V}(\vec{r}+\vec{R})$ with respect to a lattice vector $\vec{R}$. Following the Bloch theorem [21], wave functions solving eq. (2) for a periodic potential are given by Bloch functions

$$\phi_{\vec{k},\nu} = \mathrm{u}_{\vec{k},\nu}(\vec{r}) \cdot e^{i\vec{k}\vec{r}} \tag{3}$$

which consist of a plane wave component, describing a free electron, multiplied by a central cell function $\mathrm{u}_{\vec{k},\nu}(\vec{r}) = \mathrm{u}_{\vec{k},\nu}(\vec{r}+\vec{R})$ following the lattice periodicity. The wave vector $\vec{k}$ in the Bloch function describes the electron momentum and the eigenvalues $\mathrm{E}_\nu(\vec{k})$ yield the electronic bandstructure of the bulk crystal. Based on these results and by considering the translation symmetry and crystalline structure, all energetic states of the system can be mapped within the first Brillouin zone and characteristic material properties such as the band curvatures and bandgap are recovered for the system within the framework of the the above discussed approximations.

Finally, the effective mass

$$m_\nu^* = \hbar^2\left(\frac{\partial^2 E_\nu(\vec{k})}{\partial\vec{k}^2}\right)^{-1} \tag{4}$$

in band ν remains to be defined as inversely proportional to the energy dispersion. For the discussion of many opto-electronic properties of semiconductors only energies close to the band extrema and for small wave vectors around $\vec{k} = 0$ are of interest. For these conditions, close to the bandgap, the curvature can often be approximated as isotropic and parabolic and with the effective mass one obtains

$$\mathrm{E}_{\vec{k},\nu} = \mathrm{E}_{0,\nu} + \frac{\hbar^2\vec{k}^2}{2m_\nu^*}\ . \tag{5}$$

Eq. (5) resembles the solution of the Schrödinger equation for a free particle ($\mathrm{V}(\vec{r}) = 0$, see for example ref. [16]) with mass m_ν^*, offset by the band extrema $\mathrm{E}_{0,\nu}$. This implies that in common bulk semiconductor systems, it can often be sufficient to treat electrons as free moving particles where all effects of the periodic ionic lattice are bundled in an alteration of the electron mass and electrons experience their world as three-dimensional.

Low dimensional systems and envelope function approximation

Based on the previous discussion, it now is possible to explore how spatial confinement alters the system's electronic properties. In contrast to the bulk system, a lower dimensional system has a limited spatial extent along one or more dimensions of the order of λ_{dB}. Because for many semiconductors λ_{dB} is in the order of tens of nanometers [18], the confinement structure is in many experimental realizations, including the ones in this thesis, of much larger scale than the lattice constant. The resulting structures are, due to their dimensions, referred to as nanostructures. In nanostructures, the confinement effects are introduced by a perturbation potential $\mathrm{V}_{\mathrm{nano}}(\vec{r})$ and the new energy spectrum is obtained by solving the single-electron Schrödinger equation $[\hat{\mathrm{H}}_{1\mathrm{e}} + \mathrm{V}_{\mathrm{nano}}(\vec{r})]\phi_\nu(\vec{r}) = \mathrm{E}\phi_\nu(\vec{r})$. The Bloch theorem, however, no longer offers solutions for the wave function as the confinement potential breaks the translational symmetry of the ionic lattice.

Instead, a spatial decoupling scheme in the form of the so called envelope function approximation can be used to solve the perturbed single-electron Schrödinger equation. The envelope function approximation is based on the assumption that the perturbation-induced energy shift is small compared to the energetic difference between individual bands in the bandstructure and thus the perturbed wave function is similar to the unperturbed wave function. Further, because $\mathrm{V}_{\mathrm{nano}}(\vec{r})$ varies slowly compared to the lattice constant, it is assumed that states for small $\vec{k}$ dominate. Then, the wavefunction to solve the perturbed single-electron Schrödinger equation

$$\phi_\nu(\vec{r}) \approx \mathrm{u}_{\nu,0} \cdot \mathrm{F}_\nu(\vec{r}) \tag{6}$$

is approximated by the central cell function for $\vec{k} = 0$ multiplied by an envelope function $\mathrm{F}_\nu(\vec{r})$. In the effective mass approximation, it now becomes possible to separate the periodic lattice potential $\mathrm{V}(\vec{r})$ from $\mathrm{V}_{\mathrm{nano}}(\vec{r})$ and the envelope function enters the Schrödinger equation

$$\left[-\frac{\hbar^2}{2m_\nu^*}\Delta + \mathrm{V}_{\mathrm{nano}}(\vec{r})\right] \mathrm{F}_\nu(\vec{r}) = (\mathrm{E} - \mathrm{E}_{0,\nu})\mathrm{F}_\nu(\vec{r}) \ . \tag{7}$$

Equation (7) allows to discus the relevant physics to understand the effect of confinement on the electronic structure of bulk systems and comes with interesting implications: 1) $\mathrm{V}_{\mathrm{nano}}(\vec{r})$ introduces an energy shift compared to the unperturbed band extrema $\mathrm{E}_{0,\nu}$ and 2) The energy shift of the perturbed state depends only on the envelope function $\mathrm{F}_\nu(\vec{r})$.

In the following, the example of electrons in the conduction band of a semiconductor with the band minimum E_{C} and an effective mass m^* is discussed. The lattice constant of the semiconductor is given by a_0 and the spatial extent of the semiconductor along the x and y directions is significantly larger than λ_{dB}. Along the z-axis the semiconductor has a length L such that $\lambda_{\mathrm{dB}} \geq L \gg a_o$.

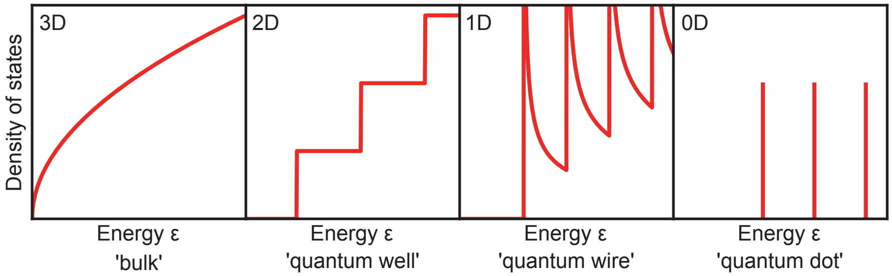

Figure 1: Density of states in systems of different dimensionality.

This confinement introduces the boundary condition $\mathrm{F_C}(x, y, 0) = \mathrm{F_C}(x, y, L)$ for the envelope function and the problem can be separated into electron motion perpendicular and parallel to unconfined electron motion. According to the Bloch theorem, in x and y direction, the envelope function is given by plane waves and can thus be expressed as $\mathrm{F_C}(x, y, z) = e^{i\vec{k}_x\vec{x}}e^{i\vec{k}_y\vec{y}}\chi(z)$ with a standing wave $\chi(z)$, the textbook result for confined particles (see for example ref. [16]), along the z axis. With $\vec{k}_{\|}^2 = \vec{k}_x^2 + \vec{k}_y^2$, the resulting energy shift relative to the conduction band minimum

$$\mathrm{E} - \mathrm{E_C} = \mathrm{E}_n + \frac{\hbar\vec{k}_{\|}}{2m^*}\ , n \in \mathbb{N}_{>0} \tag{8}$$

in eq. (7) becomes the sum of two parts: 1) A discrete energy contribution, the solution for the standing wave component of the wave function and characterized by a quantum number n which is induced by confinement of the electronic wave function along z as well as 2) the kinetic energy of the free electron motion within the (x, y)-plane comparable to a two-dimensional bulk system.

These results for a two-dimensional nanostructure imply that confinement effects introduce a series of discrete energies E_n which shift the electron energies against the unperturbed conduction band minimum with an energy dispersion $\mathrm{E}(\vec{k}_{\|})$ resembling that of free electrons in reduced dimensions. Consequently, subbands form within a given band ν (the conduction band in the presented example) in which electrons can move freely along the unconstrained dimensions.

Following the same scheme, eq. (7) can also be solved for one-dimensional (assume spatial confinement in z and y direction) and zero-dimensional (confinement in all dimensions) nanostructures. One then obtains the single-electron conduction band energy spectrum

$$E = E_C + \begin{cases} \dfrac{\hbar^2 \vec{k}^2}{2m^*} & \text{3D} \\ E_n + \dfrac{\hbar^2 \vec{k}_{\parallel}^2}{2m^*} & \text{2D} \\ E_n + E_m + \dfrac{\hbar^2 \vec{k}_x^2}{2m^*} & \text{1D} \\ E_n + E_m + E_l & \text{0D} \end{cases} \tag{9}$$

for an electron in the effective mass and envelope function approximation, where $E_{n,m,l}$ denote the discrete energy contributions originating from confinement in x, y and z-direction. This result demonstrates that while for a three-dimensional bulk crystal the energy spectrum is continuous, subbands are formed for two- and one-dimensional nanostructures. In the case of zero-dimensional nanostructures the single-particle energy spectrum is independent of $\vec{k}$ and is thus fully discretized. Because this resembles the atomic spectrum rather than describing a crystals bandstructure, zero-dimensional systems are also referred to as artificial atoms [22].

It is noteworthy, that $E_{n,m,l}$ depend strongly on the shape and energetic height of the confinement potential $V_{\text{nano}}(\vec{r})$ and therefore the experimental implementation of the low-dimensional system. While, for example, material constricted nanostructures and heterostructures will have sharp potential walls, electrostatically defined structures can be more smooth. For the textbook example of infinitely high potential walls confining the particle to a well of length L, the discrete energies $E_{j=n,m,l} = \frac{\hbar^2 \pi^2}{2m^*} \frac{j^2}{L}$ are obtained (see for example ref. [16]).

Many opto-electronic properties and effects in semiconductors are closely linked to the density of states. The density of states of band ν, neglecting spin, $n_\nu(\epsilon) = \frac{1}{V} \sum_{\vec{k}} \delta(\epsilon - E_{\nu,\vec{k}})$ describes a density of available states at a given energy ϵ per volume V [17] and can be calculated directly from eq. (9). Here, $\delta(x)$ denotes the Dirac delta function. Assuming an isotropic parabolic dispersion the conduction band density of states reads

$$n(\epsilon) \propto \begin{cases} \Theta(\epsilon - E_C)\sqrt{\epsilon - E_C} & \text{3D} \\ \sum_n \Theta(\epsilon - E_n) & \text{2D} \\ \sum_{n,m} \Theta(\epsilon - E_{n,m}) \frac{1}{\sqrt{\epsilon - E_{n,m}}} & \text{1D} \\ \sum_{n,m,l} \delta(\epsilon - E_{n,m,l}) & \text{0D} \end{cases} \tag{10}$$

with the Heaviside step function $\Theta(x)$. The density of states for different dimensionalities is indicated in fig. 1. Figure 1 illustrates a few key properties and differences of low-dimensional compared to bulk systems. In comparison to bulk systems, the energy ground state is shifted in low-dimensional systems and $n(\mathrm{E})$ is continuous as long as electrons can move freely in at least one spatial direction. For two- and one-dimensional systems sudden increases of $n(\mathrm{E})$ arise when a new subband is energetically available. Zero-dimensional systems are fully quantized and exhibit atom-like properties.

Finally, it should be noted that for the description of many opto-electronic properties not only the electronic structure of a system but also the occupation of the available electronic states is relevant. In equilibrium, electrons follow the Fermi-Dirac statistics and the occupation probability of an energy state at energy ϵ is given by

$$f(\epsilon, \mu, \mathrm{T}) = \frac{1}{e^{\frac{\epsilon-\mu}{k_\mathrm{B}\mathrm{T}}} + 1} \,. \tag{11}$$

Here, μ is the system's electro-chemical potential, T is the temperature and k_B is the Boltzmann constant.

2 The Coulomb blockade effect

Early experiments in the 1950s on transport through grains in thin films at low temperatures revealed that the so far discussed single-particle picture is insufficient to explain the resistance behavior of small systems and transport can become dependent on the Coulomb interactions between individual charge carriers [23, 24]. With rapid advancements in device fabrication techniques and miniaturization in the 1980s [19], these effects became accessible through studies of transport across individual nanoscale islands, insulated from the electronic circuit by tunnel barriers. These studies led to a quickly emerging, detailed understanding of Coulomb blockade, a phenomena based on the quantization of charge and Coulomb interactions between electrons in spatially confined, often zero-dimensional systems, giving rise to single-electron tunneling and a many-particle energy spectrum within nanoscale systems [25–28].

It should be noted that for Coulomb blockade to occur, a quantum dot defined by a discrete single-particle energy spectrum as a result of confinement of the electronic wave function in all three dimensions [19], is not required. Instead, Coulomb blockade is observable also in larger structures at sufficiently low temperatures and a more distinguishable nomenclature for systems exhibiting Coulomb blockade is Coulomb island [22]. This distinction is not always made sufficiently clear in literature. In line with the experimental system discussed later in this thesis, in the following the term quantum dot is used to refer to systems where both Coulomb blockade and a zero-dimensional single-particle energy spectrum are present and this thesis finds itself in excellent company in choosing simplicity over accurate nomenclature.

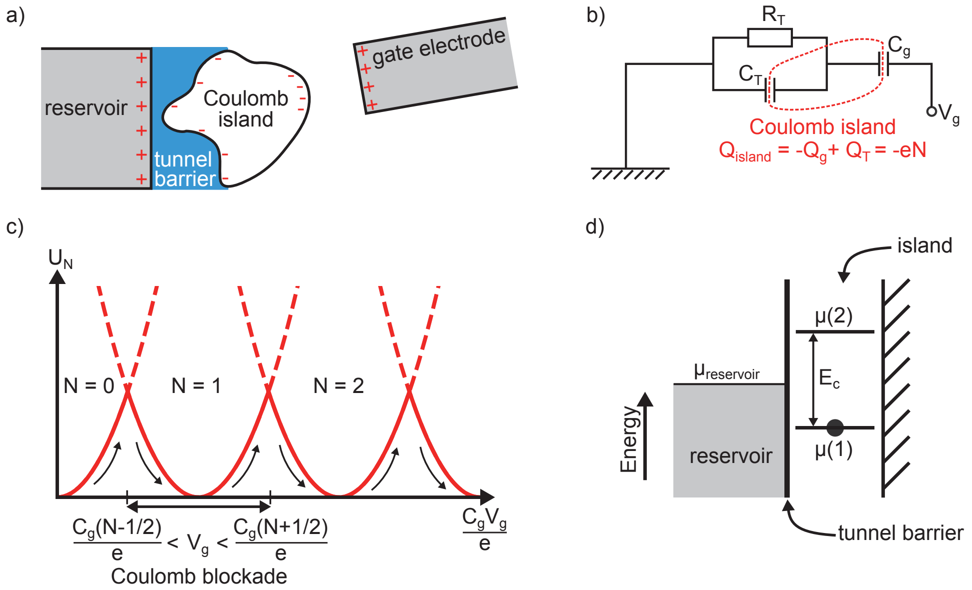

Figure 2: The single electron box (SEB). a) Schematic illustration of a SEB. b) Classical equivalent circuit of (a). c) N-dependent electrostatic energy contribution U_N plotted against $\frac{C_gV_g}{e}$. d) Schematic level diagram of a SEB.

A simple approach to visualize and understand Coulomb blockade is to consider the exemplary system of a single electron box (SEB). A detailed description of a SEB is found for example in refs. [29–32]. A SEB is schematically illustrated in fig. 2(a) and consists of a small metallic Coulomb island tunnel coupled to a large electron reservoir. An additional gate-electrode is capacitively coupled to the island such that no current can flow between the gate-electrode and the island. In the following, the principles of Coulomb blockade are introduced for a Coulomb island in the framework of the constant interaction model [19]. The constant interaction model is based on two assumptions: All relevant interactions between electrons or holes on the Coulomb island as well as between electrons or holes on the island and its charge environment are described by capacitances. Further, the capacitances are considered independent of the number of electrons on the island [19].

In the constant interaction model, the system in fig. 2(a) can be described by a classic equivalent circuit, shown in fig. 2(b). The capacitive coupling of the gate electrode, with an applied voltage V_g, to the Coulomb island is characterized by the gate capacitance C_g. The tunnel barrier connecting the electron reservoir (here at ground potential) to the island is described by a tunneling resistor R_T and a tunneling capacitor with capacitance C_T in parallel. It should be noted that in order for the charge carrier wave function to be localized on the island, a requirement for the observation of well-defined single-charge tunneling, R_T must be much larger than the resistance quantum $\frac{h}{e^2}$ [29].

The charge Q_{island} present on the Coulomb island is given by the sum of the charges found on the capacitor plate corresponding to the island of the tunneling (Q_T) and gate (Q_g) capacitor. Because the island is electrically insulated from the rest of the circuit and charge is quantized in the form of electrons carrying the elemental charge e,

$$Q_{\text{island}} = Q_T - Q_g = -eN \tag{12}$$

is constant for a given V_g and described by an integer number of electrons N on the island [31]. Based on that concept, the total electrostatic energy of the Coulomb island with a set number of electrons N at a gate voltage V_g

$$U(N) = \int_0^{-Ne} \Phi(Q_{\text{island}})dQ_{\text{island}} = \frac{e^2}{2C_\Sigma}\left(N - \frac{C_gV_g}{e}\right)^2 - \frac{C_gV_g^2}{2} \tag{13}$$

can be obtained [25]. Here, $\Phi(Q_{\text{island}})$ is the electrostatic potential of the Coulomb island and $C_\Sigma = C_T + C_g$ denotes its self capacitance. The electrostatic energy U(N) consists of a component dependent on N which is, for different N, plotted against $\frac{C_gV_g}{e}$ in fig. 2(c) and an N-independent offset [32].

Figure 2(c) illustrates that $U_N(\frac{C_gV_g}{e})$ yields a set of parabolas for each charge state N [30]. The ground state of the system, defined as the charge state with the lowest electrostatic energy, shifts through different electron numbers N on the Coulomb island via variation of the gate voltage V_g. Consequently, in between the parabola crossing points within a range $\frac{e}{C_g}(N - \frac{1}{2}) < V_g < \frac{e}{C_g}(N + \frac{1}{2})$ the number of electrons on the island remains constant and no electron exchange with the reservoir occurs. The system is in a Coulomb blockade state. In contrast, if V_g is chosen such that it matches the crossing point of two parabolas corresponding to successive N and N+1, a single electron can tunnel between the Coulomb island and the electron reservoir.

The Coulomb blockade effect can be understood qualitatively by considering the repulsion between the electrons located on the Coulomb island and an electron waiting to enter the island, which has to be overcome by the attractive force exerted by the gate electrode. For spatially small islands, the involved capacitances are small and thus the Coulomb blockade effect induces a discrete energy spectrum to the island: By following the definition of the electro-chemical potential μ(N+1) as the minimum energy required to add the (N+1)th electron to an island with N electrons [19],

$$\mu(N+1) = U(N+1) - U(N) = \frac{e^2}{2C_\Sigma}(2N+1) - e\alpha_g V_g \tag{14}$$

a ladder of discrete energy levels on the island is obtained. Each level can be occupied by one electron only and the energetic position depends linearly on V_g. In eq. (14), $\alpha_g = \frac{C_g}{C_\Sigma}$ is the lever arm of the gate and relates the voltage applied to the gate electrode to the energy shift induced on the Coulomb island's electrochemical potentials. The relevant energy scale for the Coulomb island is given by its charging energy [30]

$$E_c = \mu(N+1) - \mu(N) = \frac{e^2}{C_\Sigma} \tag{15}$$

defined as energy difference between two consecutive levels μ(N+1) and μ(N) and is independent of N and V_g.

Figure 2(d) shows the schematic energy level diagram of a SEB. The Coulomb island is separated by a tunnel barrier from the electron reservoir with the electro-chemical potential $\mu_{\text{reservoir}}$ and is characterized by a series of discrete levels μ(N) spaced by the charging energy E_c. Levels on the island can be energetically shifted down (up) by increasing (decreasing) the gate voltage V_g. All island levels that are energetically below $\mu_{\text{reservoir}}$ are occupied by an electron, all levels above $\mu_{\text{reservoir}}$ are empty. The system is in Coulomb blockade unless V_g is chosen such that $\mu_{\text{reservoir}} = \mu(N)$ lifts the Coulomb blockade and allows the exchange of a single electron with the reservoir. Comparable schematic energy level diagrams will in the following be sufficient to explain the characteristic transport properties of single- and double quantum dot devices.

Finally, the Coulomb blockade effect is only observable at low temperatures T such that the energetic smearing of the electron distribution in the reservoir is small compared to the charging energy of the Coulomb island, $k_B T \ll E_c$. In the opposite limit, if $k_B T \gg E_c$, the energy spectrum of the Coulomb island can be treated as continuous [27].

Charge transport through quantum dot systems

At its core, the experimental work in this thesis discusses transport across single QD and DQD devices, tunnel coupled to two charge carrier reservoirs. This chapter aims to introduce the concepts necessary to understand the experimental work first qualitatively, based on the constant interaction model before quantifying currents across QD systems via rate equations. Although, both n- and p-type material systems are used for the experimental realization of QD systems in papers I to III, the following discussion is limited to the description of n-type QD and DQD. The qualitative description of transport can nevertheless be directly transferred to p-type systems by considering an opposite sign for the charge of the charge carriers.

3 Qualitative description: Constant interaction model

This section discusses the characteristics of transport across QD and DQD devices in the framework of the constant interaction model [19]. In contrast to the previous discussion, now the single-particle energy spectrum of the QDs has to be taken into account. In the constant interaction model, the many-particle spectrum is described by the single-particle spectrum of the QD or DQD with all degeneracies lifted by the Coulomb interactions. The constant interaction model provides sufficient tools to qualitatively understand and predict many transport phenomena in QD systems.

Transport through single quantum dots

The simplest QD system to study transport phenomena is conceptually close to the so far discussed SEB and consists of a QD tunnel coupled to two electron reservoirs (source and drain) and capacitively coupled to a gate electrode as illustrated in fig. 3(a). In contrast

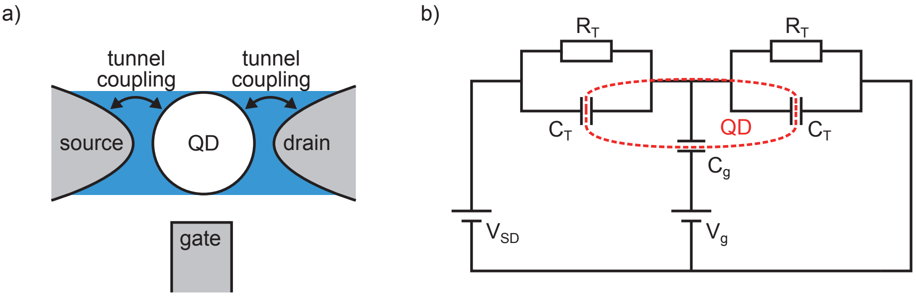

Figure 3: Schematic illustration of a single quantum dot device. a) Schematic illustration of a single quantum dot tunnel coupled to a source and drain reservoir and capacitively coupled to a gate electrode. b) Classical equivalent circuit of the single quantum dot device.

to a SEB the QD device allows for electrons to flow across the QD which also exhibits a single-particle energy spectrum. The classical equivalent circuit for a device with symmetric tunnel barriers is shown in fig. 3(b) and a detailed description of the electronic and transport properties can be found in refs. [4, 6, 27] as well as in the appendix of ref. [5].

A discussion of the transport properties across the QD in the framework of the constant interaction model follows the same scheme as presented for the SEB in the previous section. The total electrostatic energy of the system illustrated in fig. 3(b), $U(N, V_g, V_{SD})$, now not only depends on the number of electrons on the quantum dot and the gate voltage but also the voltages applied between the source and drain contacts. In the following, the drain contact remains grounded and a bias of V_{SD} is applied to the source. With the self capacitance of the QD $C_\Sigma = C_T + C_T + C_g$ the electro-chemical potential for the Nth QD level can be written as

$$\mu_n(N) = \frac{e^2}{2C_\Sigma}(2N - 1) + \epsilon_n - e\sum_i \alpha_i V_i \tag{16}$$

and consists of three parts: The first term corresponds to the contribution of the Coulomb-interaction induced discrete energy spectrum and the second term ϵ_n is the energy of the single-particle level with index n which the Nth electron occupies. The last term accounts for all external capacitive contributions from electrodes acting as gates at a voltage V_i, where $\alpha_i = \frac{C_i}{C_\Sigma}$ is the lever arm and C_i the capacitance attributed to the coupling of the QD with the electrode. In general the source and drain contact can act as a gate to the QD but for simplicity capacitive contributions from the tunnel contacts are here considered negligible such that $e\sum_i \alpha_i V_i = e\alpha_g V_g$. Finally, it should be noted that $\mu_n(N)$ only denotes a ground state of the system if ϵ_n is the energetically lowest available single-particle level for the Nth electron and otherwise describes an excited state of the QD.

In line with the description of the SEB, the relevant spacing between two successive ground

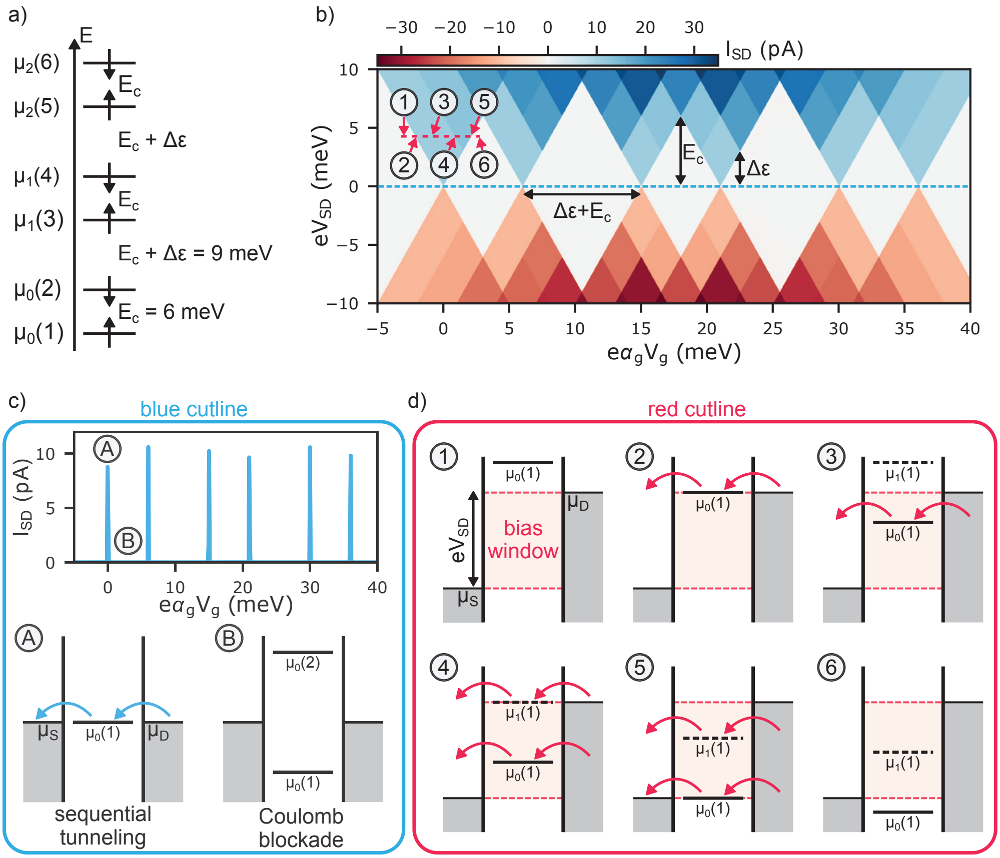

Figure 4: The QD charge stability diagram. a) Ground state energy spectrum of the QD. b) Charge stability diagram. c) Transport in the low bias regime and Coulomb oscillations at $V_{SD} = 100\ \mu V$. d) Transport in a high bias regime.

states is given by the addition energy

$$E_{add} = \mu_m(N+1) - \mu_n(N) = E_c + (\epsilon_m - \epsilon_n) = E_c + \Delta\epsilon \tag{17}$$

with the Coulomb interaction induced charging energy $E_c = \frac{e^2}{C_\Sigma}$ and a contribution from the single-particle energy spectrum $\Delta\epsilon$. The latter only yields a nonzero contribution if two consecutive electrons occupy different single-particle levels, $m \neq n$.

Electron transport through the device is only possible if the system is not in a Coulomb blockade state. This requires a ground state level $\mu_n(N)$ to be located in between the electrochemical potentials of the source (μ_S) and drain (μ_D) contact. Then, electrons can flow from source to drain (drain to source) if the condition $\mu_S \leq \mu_n(N) \leq \mu_D$ ($\mu_S \geq \mu_n(N) \geq \mu_D$) is fulfilled [6]. A bias difference applied between the source and drain tunnel contacts opens an energetic transport window, $eV_{SD} = \mu_D - \mu_S$ and thus fulfillment of the transport conditions depend on the bias V_{SD} across the device and the gate voltage V_g. Consequently, mapping the current I_{SD} across the device as a function of V_{SD} and V_g reveals regions in which the QD is in Coulomb blockade and the QD's charge remains fixed. The resulting current map is thus referred to as the charge stability diagram of the device and directly reveals information about the charge state of the device, the charging energy and the single-particle energy spectrum.

To demonstrate the transport behavior of QD devices, the so-far derived properties are used to discuss an exemplary QD device with three spin-degenerate single-particle energy levels. The Coulomb interactions between electrons on the QD lift the degeneracy of the single-particle levels and the ground state energy spectrum of the device for a charging energy of $E_c = 6\,\text{meV}$ and

$$\Delta\epsilon = \begin{cases} 0\,\text{meV}, & \text{N odd} \\ 3\,\text{meV}, & \text{N even} \end{cases} \tag{18}$$

is illustrated in figure 4(a). Figure 4(b) shows the charge stability diagram calculated for the energy spectrum in (a). To understand the characteristic shapes observed within the QD's charge stability diagram, it helps to consider two specific cases.

First, a negligibly small positive bias, just sufficient enough to give electrons an incentive to move from drain to source is applied to the device and the gate voltage remains variable. This condition describes the blue cutline in the charge stability diagram in fig. 4(b) and the transport mechanism is schematically illustrated in (c). If V_g is chosen such that a ground state $\mu_n(N)$ is aligned with the contacts' electrochemical potentials, $\mu_S \approx \mu_D$ a current across the device is detected. It should be noted that only one electron at a time can be transported across the QD due to the non-degenerate nature of $\mu_n(N)$. Thus, this transport process is referred to as sequential tunneling, illustrated in Ⓐ. In contrast, if no QD level $\mu_n(N)$ is available within the transport window, the system is in Coulomb blockade, see Ⓑ. Consequently, continuous variation of V_g gives rise to an oscillatory current, the so-called Coulomb oscillations [22]. The spacing between two neighboring current peaks is given by $\Delta V_g = \frac{1}{\alpha_g e}(E_c + \Delta\epsilon)$.

Second, if the bias window is increased, $V_{SD} > 0$, the balance between regions of zero and non-zero current along V_g is shifted as exemplary illustrated along the red cutline in fig. 4(b). The transport mechanisms along the cutline are shown in fig. 4(d). Initially, see ①, no level $\mu_n(N)$ is accessible within the transport window and the device is in Coulomb blockade. Once the gate bias is changed such that $\mu_n(N) = \mu_D$ (②) electrons can tunnel from drain to source in a sequential manner and the onset of a conductive region in the charge stability diagram is observed. The device remains conductive while $\mu_D \leq \mu_n(N) \leq \mu_S$ ③ and re-enters a Coulomb blockade state once point ⑤ where the QD level is aligned with the source electro-chemical potential, $\mu_S = \mu_n(N)$, is surpassed.

If the bias window is chosen such that $eV_{SD} > \Delta\epsilon$, a situation were both a ground state

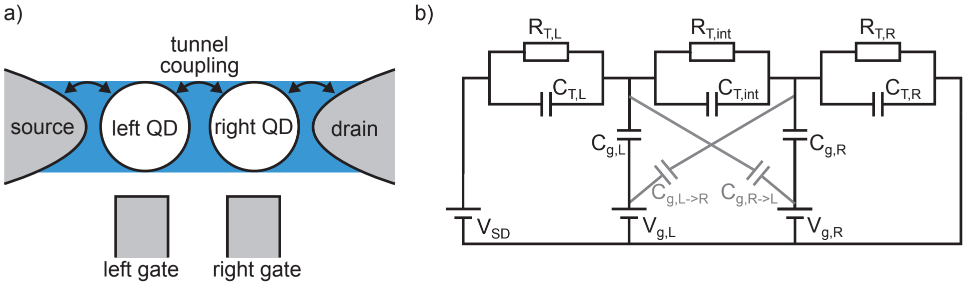

Figure 5: Schematic illustration of a DQD. a) Schematic illustration of a DQD consisting of two QDs in series tunnel coupled to a source and drain electron reservoir. Each QD has a dedicated gate electrode. b) Classical equivalent circuit of (a).

μ_n(N) and an excited state μ_m(N) are within the bias window can be obtained, see ④. Although, unless $eV_{SD} \leq E_c$ is fulfilled still only one electron can pass the device at a time but the overall transmission probability for an electron is increased if an excited state is energetically accessible. Consequently, the single-particle energy spectrum manifests as a distinct pattern within the conductive regions of the charge stability diagram in fig. 4(b).

By consideration of different V_{SD}, the charge stability diagram of a QD is mapped. Regions of Coulomb blockade, in which the charge state N of the QD remains fixed are, due to their characteristic shape, referred to as Coulomb diamonds. The height height and width of the Coulomb diamonds correspond directly to the addition energy. A detailed discussion of a variety of additional features that manifest in the charge stability diagram of QDs is found in ref. [33].

Transport through serial double quantum dots

By combination of two QDs in series, a DQD is formed. The DQD, schematically illustrated in fig. 5(a) can conceptually be described as an extension of the QD device by a second QD and gate. The source (drain) contact is tunnel coupled exclusively to the left (right) QD and the two QDs are connected by a tunnel barrier. Thus, to transport charge carriers from the source to the drain contact or vice versa, the charge carriers have to pass through both QDs and the conditions to enable transport discussed in the previous section must be fulfilled for each of the two QDs. Further, both QDs are equipped with a dedicated gate, referred to as left and right plunger gate to shift the electro-chemical potentials on the left and right QD, respectively.

Fig. 5(b) shows the classical equivalent circuit of the DQD. The interdot tunnel coupling is described by $R_{T,int}$ and $C_{T,int}$ and enables tunneling between the left and right QD. Each of the two plunger gates in the system is coupled capacitively to its respective dot via $C_{g,L/R}$, but can also affect the other dot via a capacitive cross-coupling $C_{g,L/R\rightarrow R/L}$. The left (right) QD is characterized by its self capacitance $C_{\Sigma,L(R)} = C_{T,L(R)} + C_{g,L(R)} + C_{T,int} + C_{g,R(L)\rightarrow L(R)}$. The total electrostatic energy of the DQD $U(N, M, V_{SD}, V_{g,L}, V_{g,R})$ depends on the number of electrons N on the left and M on the right dot as well as the bias across the device and voltages applied to the plunger gate electrodes.

Although for many experimental device architectures both the plunger gate cross coupling and the bias V_{SD} affect the energy levels on the QDs, these effects do not conceptually alter the transport properties of the device. Thus, in the following these two effects are neglected, reducing the total electrostatic energy to $U(N, M, V_{g,L}, V_{g,R})$ and the QD self capacitance to $C_{\Sigma,L(R)} = C_{T,L(R)} + C_{g,L(R)} + C_{T,int}$. A detailed description of the here introduced DQD system in the framework of the constant interaction model can be found in refs. [5, 6] and the following discussions are based mainly on ref. [5].

Information regarding the discrete energy level structure of the two QDs in the system is, in analogy with the treatment of QDs and the SEB, contained within their electrochemical potentials. As a result of the capacitive coupling between the two QDs, however, the electro-chemical potential of the left QD with N electrons charged to the QD can not be treated independent of the occupancy number M of the right QD and vice versa. Consequently, the electrochemical potential of the left dot

$$\mu_n^L(N,M) = \left(U(N,M) + \sum_i^N \epsilon_{n(i)}^L\right) - \left(U(N-1,M) + \sum_i^{N-1} \epsilon_{n(i)}^L\right) = \\ = \left(N - \frac{1}{2}\right) E_{c,L} + ME_{c,int} - \frac{1}{e}\left(C_{g,L}V_{g,L}E_{c,L} + C_{g,R}V_{g,R}E_{c,int}\right) + \epsilon_n^L \quad (19)$$

is defined as energy required to add the Nth electron to the left QD with a constant number of M electrons charged to the right QD [5]. In complete analogy, the electrochemical potential of the right QD is then given by

$$\mu_n^R(N,M) = \left(M - \frac{1}{2}\right) E_{c,R} + NE_{c,int} - \frac{1}{e}\left(C_{g,R}V_{g,R}E_{c,R} + C_{g,L}V_{g,L}E_{c,int}\right) + \epsilon_n^R\,. \quad (20)$$

Here, ϵ_n^L is the single particle energy of the Nth electron on the left QD (ϵ_m^R of the Mth electron on the right QD) and $\epsilon_{n(i)}^L$ ($\epsilon_{m(i)}^R$) denotes the single particle energy of the ith electron on the left (right) QD. The energy scales are set by $E_{c,L}$, $E_{c,R}$ and $E_{c,int}$, which take the role of the charging energies of the left and right as well as the interdot coupling energy, respectively. The interdot coupling energy sets the energy scale by which the energy of one QD is adjusted when an electron is charged or discharged from the other QD [5].

The energy scaling factors $E_{c,L}$, $E_{c,R}$ and $E_{c,int}$ are given by:

$$E_{c,L} = \frac{e^2}{C_{\Sigma,L}} \left(\frac{1}{1 - \frac{C_{T,int}^2}{C_{\Sigma,L} C_{\Sigma,R}}} \right) \tag{21}$$

$$E_{c,R} = \frac{e^2}{C_{\Sigma,R}} \left(\frac{1}{1 - \frac{C_{T,int}^2}{C_{\Sigma,L} C_{\Sigma,R}}} \right) \tag{22}$$

$$E_{c,int} = \frac{e^2}{C_{T,int}} \left(\frac{1}{\frac{C_{\Sigma,L} C_{\Sigma,R}}{C_{T,int}^2} - 1} \right) \tag{23}$$

The addition energies for the left and right QD, again defined as difference in energy between two successive ground states in the left or right QD [5],

$$E_{add,L} = \mu_{n'}^{L}(N+1, M) - \mu_{n}^{L}(N, M) = E_{c,L} + \left(\epsilon_{n'}^{L} - \epsilon_{n}^{L}\right) = E_{c,L} + \Delta\epsilon_{L} \tag{24}$$

$$E_{add,R} = \mu_{m'}^{R}(N, M+1) - \mu_{m}^{R}(N, M) = E_{c,R} + \left(\epsilon_{m'}^{R} - \epsilon_{m}^{R}\right) = E_{c,R} + \Delta\epsilon_{R} \tag{25}$$

resemble the form of eq. (17) for a single QD device. In eqs. (24) and (25), ϵ_{n}^{L} (ϵ_{m}^{R}) denotes the single-particle energy of the Nth (Mth) electron on the left (right) QD and $\epsilon_{n'}^{L}$ ($\epsilon_{m'}^{R}$) denotes the single-particle energy of the (N+1)th ((M+1)th) electron on the QD. Consequently, $\Delta\epsilon_{L/R}$ only yields a non-zero contribution to the addition energy if two consecutive electrons on one dot occupy different single-particle states. The resemblance of eqs. (24) and (25) to the QD case in turn justifies the previous definition of the charging energy where the capacitive coupling between the two individual QDs introduces a correction factor [5].

The charge stability diagram

By studying its charge stability diagram, an overview as well as experimental access to many properties, including the charge occupancies and the energetic structure of the DQD device can be obtained. In analogy to the QD device the charge stability diagram illustrates regions of non-vanishing conductance and Coulomb blockade of the DQD device dependent on the externally applied voltages. While for a QD, only the source-drain and gate voltage is relevant and the charge stability diagram is of three-dimensional nature, the situation is more complex for a DQD. With the second QD and gate in play, the current through the device depends on three voltages and the complete charge stability diagram becomes four-dimensional. For the visualization of many device properties of the DQD, however, it is sufficient to fix the source-drain bias at a constant value and study the transport behaviour as a function of the left and right plunger gate.

The characteristic shape of regions of constant charge in the ($V_{g,L}$-$V_{g,R}$)-plane are readily described in the situation where $V_{SD} = 0$ and the electro-chemical potentials of the source

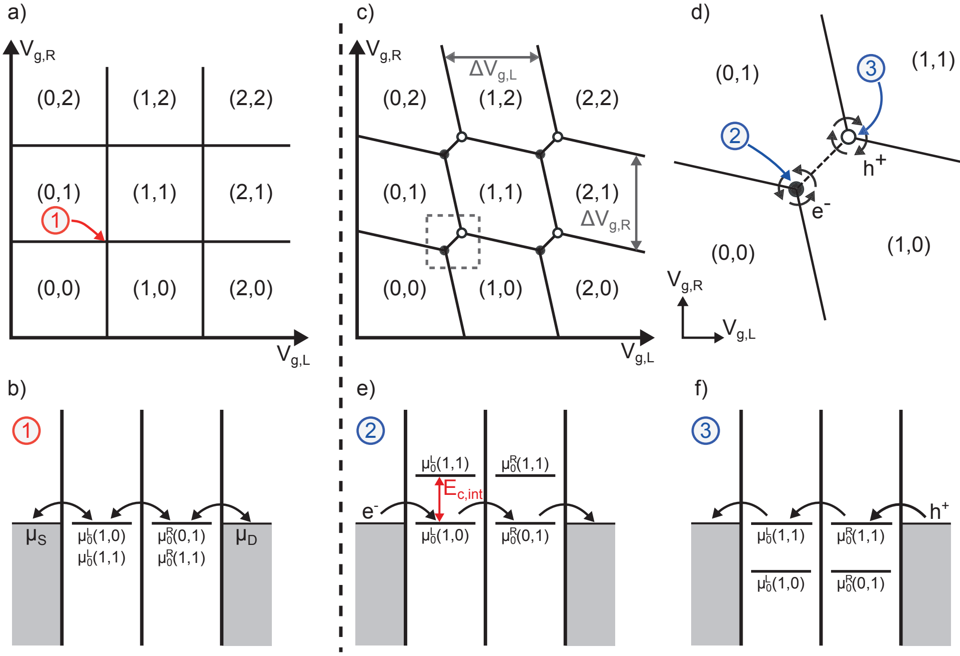

Figure 6: **The DQD charge stability diagram.** a) Charge stability diagram in the limit of vanishing capacitive coupling between the two QDs. b) Illustration of the DQD level diagram on the fourfold-degenerate charge state points in (a). c) Charge stability diagram for a non-negligible capacitive interdot coupling. d) Illustration of the electron and hole transport cycle triple points. e) Illustration of the electron transport cycle. f) Illustration of the hole transport cycle. In b/e/f index 0 denotes a ground state of the DQD. (a/c) are inspired by [5].

and drain contact coincide, $\mu_S = \mu_D = \mu_{SD}$. First, the simplified case of vanishing capacitive coupling between the two individual QDs, $C_{T,int} \rightarrow 0$ is considered. Then, the interdot coupling energy also vanishes, $\lim_{C_{T,int}\rightarrow 0} E_{c,int} = 0$, and the electro-chemical potential of each QD becomes independent of the occupation of the second QD. The correction factors to the charging energies in eqs. (21) and (22) then equal to one and the charging energies of the left and right dot are given by $E_{c,L/R} = \frac{e^2}{C_{\Sigma,L/R}}$. Thus, the description of the DQD system is reduced to the discussion of single QDs at vanishing bias, as described in fig. 4(c).

Upon variation of the left (right) plunger gate $V_{g,L(R)}$ the electro-chemical potentials of the left (right) QD are energetically shifted. The charge state of the left (right) QD remains constant and the QD is in Coulomb blockade unless the condition $\mu_{S(D)} = \mu_{n(m)}^{L(R)}(N, M)$, where n, m denote ground states, is fulfilled. If the electro-chemical potential of the reservoir coupled to the left (right) QD is aligned with a ground state QD level, the Nth (Mth) electron can be exchanged with the reservoir and the charge state of the QD can be changed by one while the right (left) QD remains unaffected. Consequently, in the ($V_{g,L}$-$V_{g,R}$)-plane this behavior yields a chessboard pattern of regions of constant charge (N, M) on the DQD as illustrated in fig. 6(a). Because on the outlines of each chessboard tile the total charge state (N, M) of the DQD is changed by one, these lines are referred to as charging lines in the charge stability diagram. The extent $\Delta V_{g,L}/\Delta V_{g,R}$ of the regions of constant charge along the $V_{g,L}/V_{g,R}$-axis is, in full analogy to the discussions in 3, given by $e\alpha_{g,L/R}\Delta V_{g,L/R} = E_{add,L/R}$.

Non-vanishing conductivity across the DQD is not observed at every point in the charge stability diagram of the DQD where a charge state transition is possible. Instead, for a charge carrier to be transported through the DQD, both QDs must be in a conductive state. In the absence of a bias between the reservoirs this imposes the transport condition $\mu_{SD} = \mu_n^L(N, M) = \mu_m^R(N', M')$ for the ground state energy levels on the left and right QD, as illustrated in fig. 6(b) for the $(0, 0) \rightarrow (1, 1)$ charge transition. Within the charge stability diagram, see fig. 6(a), the transport condition is only fulfilled for points where four charge states (N, M), (N+1, M), (N, M+1) and (N+1, M+1) are energetically degenerate. As a result, non-vanishing conductance of the DQD is only found on the crossing points of charging lines.

In many DQD systems the capacitive coupling between the two QDs does not vanish, $C_{T,int} > 0$, and the simple picture of two independent QDs in series no longer holds. Instead, if an electron is added to or removed from one QD, the levels on the second QD are shifted by $E_{c,int}$. This energy shift removes the possibility to obtain points where the charge states (N, M) and (N+1, M+1) are energetically degenerate. Consequently, the fourfold degenerate points in the charge stability diagram for capacitively uncoupled QDs are split into two points where three charge states are energetically degenerate, the so-called triple points (TPs) [6]. In the resulting charge stability diagram, regions of constant charge are then hexagonal and yield a honeycomb pattern in the ($V_{g,L}$-$V_{g,R}$)-plane as illustrated in fig. 6(c). The dimensions of a honeycomb-cell $\Delta V_{g,L/R}$ and the separation between the triple points $\Delta V^{TP}_{g,L/R}$ along the left/right plunger gate axis

$$e\Delta V_{g,L/R} = \frac{e^2}{C_{g,L/R}} \left(1 + \frac{\Delta\epsilon_{L/R}}{E_{c,L/R}}\right) \tag{26}$$

$$e\Delta V^{TP}_{g,L/R} = \frac{e^2 C_{c,int}}{C_{g,L/R} C_{\Sigma,R/L}} \left(1 + \frac{\Delta\epsilon_{L/R}}{E_{c,int}}\right) \tag{27}$$

directly relate to the energy spectrum of the two QDs [5].

Cross-capacitances between the left gate and right QD as well as between the right gate and left QD lead to a shift in the electro-chemical potentials of both QDs when the voltage on one gate is adjusted. This effect introduces an additional, overall tilt to the outline of regions of constant charge, which is not considered in fig. 6(a/c) [5] but can often be seen within experimental data.

The two TPs, illustrated schematically for the $(0, 0) \rightarrow (1, 1)$ transition region in fig. 6(d) define the points in the charge stability diagram where the (N, M), (N+1, M) and (N, M+1) charge states (black dot) as well as where the (N+1, M), (N, M+1) and (N+1, M+1) (white dot) charge states are degenerate. The condition for transport across the DQD is fulfilled in each of the TPs and the TPs can be distinguished according to their transport cycle. The electron transport cycle, illustrated in fig. 6(e) describes an electron entering the left QD from the source, tunneling into the right QD and finally leaving into the drain reservoir. This transport cycle occurs at the TP corresponding to degenerate (N, M), (N+1, M) and (N, M+1) charge states (black dot in fig. 6(d)). In contrast, the TP marking the (N+1, M+1), (N+1, M), (N, M+1) degeneracy (white dot in fig. 6(d)) in the charge stability diagram can be attributed to the transport of a hole from the drain, through the right into the left QD to the source reservoir[5, 6], see 6(f).

Finally, in contrast to the charging lines, along the newly introduced boundaries of regions of constant charge, connecting an electron- and hole-cycle TP corresponding to the same charge transition within the DQD charge stability diagram, the overall charge of the DQD remains unchanged. Instead a charge is shifted from one QD to the other and this line is thus referred to as charge transfer line.

The finite bias triangles

If a bias V_{SD} is applied between the source and drain reservoir, non-vanishing conductance is not only observed at the exact locations of the TPs, but in regions forming around the TPs. Within these regions, the charge state of the DQD is no longer well defined because electron exchange between the two QDs and between the DQD and its reservoirs is possible [32]. The exact location of the conductive regions within the charge stability diagram with respect to the TPs depends on how the DQD is biased and thus a clear bias convention is important to describe the DQD charge stability diagram in a constant, non-zero bias configuration. In the following, in agreement with the experiments and fig. 5(b), V_{SD} is applied to the source contact and the drain contact remains at constant ground potential.

The energetic difference between the source and drain electro-chemical potentials is given by $eV_{SD} = \mu_D - \mu_S$ which opens up a transport window across the DQD and sets the boundaries of the transport conditions. For simplicity of notation and readability, here $\mu_0^{L/R}$ denote ground states and $\mu_1^{L/R}$ denote excited states of the left/right QD. In case of positive bias, $\mu_D > \mu_S$, transport across the DQD is possible if levels on the left and right QD are within the bias window such that the condition $\mu_D \geq \mu_0^R(N', M') \geq \mu_0^L(N, M) \geq \mu_S$ is fulfilled. In the case of a negative voltage bias the condition is altered to $\mu_S \geq \mu_0^L(N, M) \geq \mu_0^R(N', M') \geq \mu_D$. For positive (negative) bias, this condition essentially describes an effective, variable transport window for the left (right) QD in between the ground state level on the right (left) QD as well as the electro-chemical potential of the source (drain) reservoir. Consequently, non-vanishing conductance in the charge stability diagram is limited

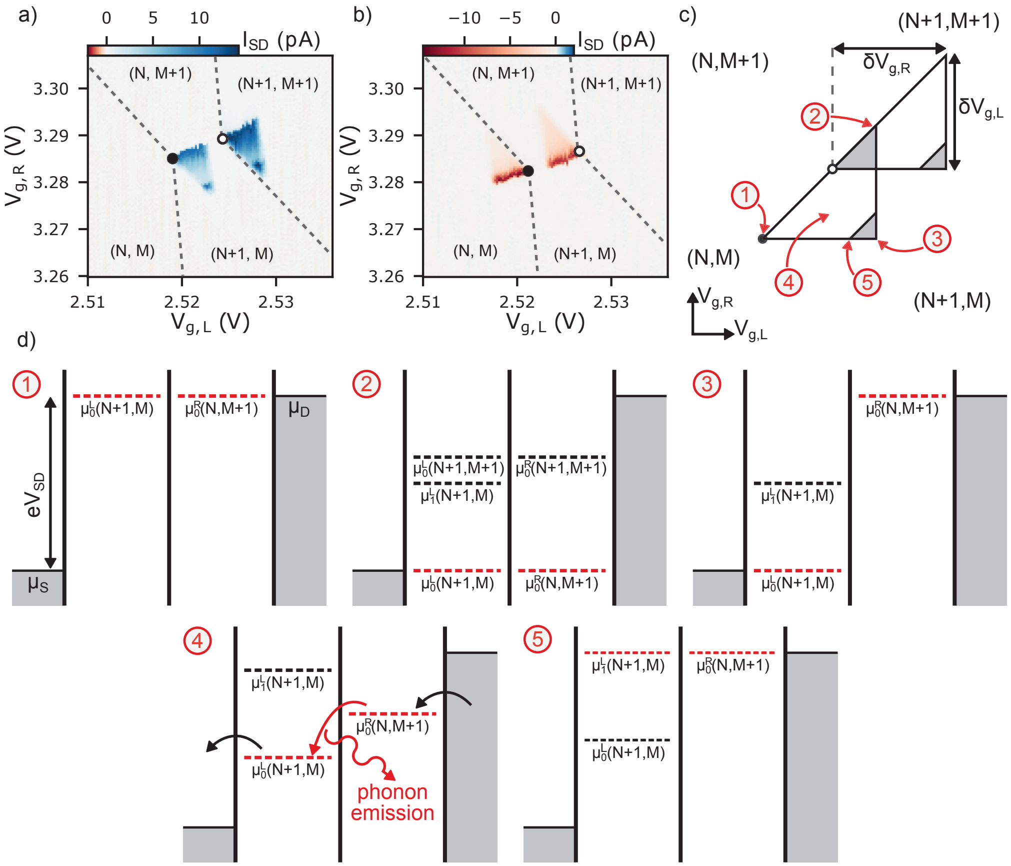

Figure 7: Illustration of the finite bias triangles. a/b) Measured current at a (N, M)→(N+1, M+1) charge transition for a bias of $V_{SD} = 1\,\mathrm{mV}$ (a) and $V_{SD} = -1\,\mathrm{mV}$ (b). c) Schematic illustration of the finite bias triangles. c) Illustration of transport within the finite bias triangles. Levels causing the relevant features or boundaries marked in (c) are labelled in red. Index 0 denotes a ground- and index 1 an excited state of the DQD.

to triangular regions, the so-called finite bias triangles.

Fig. 7(a) and (b) show the current measured through a positively (a) and negatively (b) biased DQD near a (N, M) → (N+1, M+1) charge transition. Non-vanishing current is indeed observed in triangular regions, defined by the transport conditions given above, which extend outward from the TPs. By comparing the transport conditions for positive and negative bias it becomes immediately obvious that the TPs, where ground state levels on both QDs are aligned with μ_D, act as either upper or lower bound for transport under positive or negative bias. Consequently, the triangles for positive and negative bias grow out of the TPs in opposite direction and are shifted against each other.

A detailed description of the boundaries and transport mechanisms leading to the formation of and structure within the finite bias triangles is schematically given in fig. 7(c) and (d) for the exemplary electron transport cycle of the (N, M) → (N+1, M+1) transition of a positively biased DQD. The corner points of the finite bias triangle are given by the TP ①, where $\mu_D = \mu_0^R(N+1, M) = \mu_0^L(N, M+1)$, and ② where $\mu_S = \mu_0^R(N+1, M) = \mu_0^L(N, M+1)$ as well as the point of maximum detuning ③ between the ground state level on the left and right QD for which transport is still possible, $\mu_D = \mu_0^R(N+1, M) > \mu_0^L(N, M+1) = \mu_S$.

These corner point boundaries clearly illustrate that the dimensions of the finite triangles depend directly on the magnitude of the bias window eV_{SD} and the extent of the triangles along the left and right plunger gate axis ($\delta V_{g,L/R}$)

$$eV_{SD} = \alpha_{g,L/R}\delta V_{g,L/R} \tag{28}$$

allows the separate experimental extraction of the lever arms for the two plunger gates [5].

Within the finite bias triangles, both elastic and inelastic transport occurs [34, 35]. The condition for elastic transport, $\mu_D \geq \mu_0^R(N+1, M) = \mu_0^L(N, M+1) \geq \mu_S$, is fulfilled only along the baseline of the triangle, connecting point ① to ②. Along this line, the ground states on both QDs remain aligned but their energetic position is varied. In contrast, within the finite bias triangle, see ④, the ground states on the two QDs are energetically detuned and the inelastic transport condition, $\mu_D \geq \mu_0^R(N+1, M) > \mu_0^L(N, M+1) \geq \mu_S$, is valid. Because energy must be conserved, this transport process requires exchange of energy with the DQDs environment [35], which occurs through the emission of an acoustic phonon [34]. It is noteworthy, that this process depends on the available phonon modes in the DQDs host system and can therefore be used to experimentally probe the phonon mode spectrum in the DQDs environment[36–38]. The difference between elastic and inelastic transport within the finite bias triangle explains the higher current along the baseline compared to the remaining triangle area in fig. 7(a) and (b).

Finally, in analogy to single QDs, the single-particle energy spectrum of the QDs manifests within the finite bias triangles. If the transport window eV_{SD} exceeds the ground-to-excited state spacing $\Delta\epsilon_{L/R}$ in the left or right QD and the ground states are sufficiently detuned, additional transport channels become available. While still in a sequential transport regime, this results in an increased current in the tip of the finite bias triangle and is illustrated in fig. 7(c), see ⑤, and observed in fig. 7(a) for an excited state $\mu_1^L(N+1, M)$ in the left QD. The distance from the triangle baseline to the ground state - excited state resonance can thus be used to gain insight on the single particle energy spectrum of the QDs. A detailed description of the finite bias triangles including excited states is found in ref. [5].

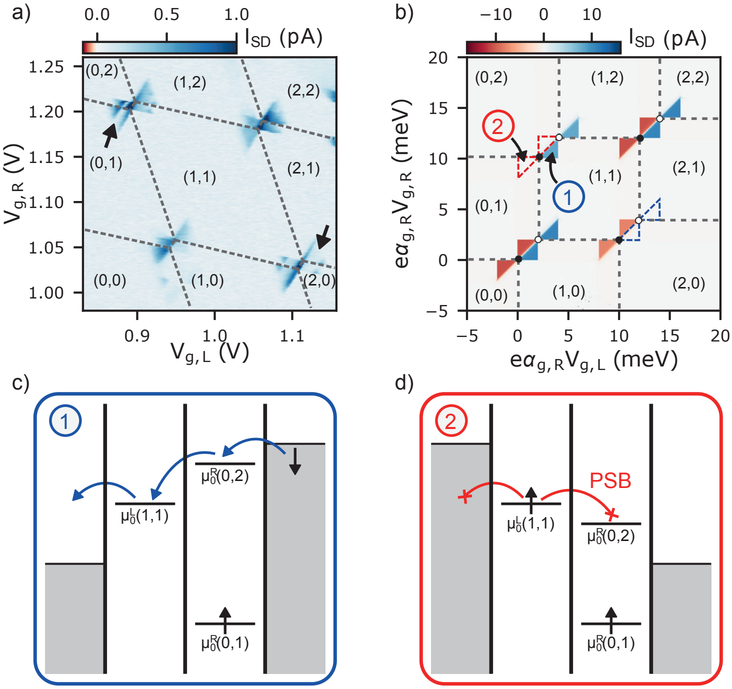

Figure 8: **Pauli spin blockade (PSB).** a) Experimentally detected current through a DQD using an AC excitation of $V_{SD} = 2\,\mathrm{mV}$ rms. Black arrows indicate PSB. b) Simulated currents in the charge stability diagram of a DQD with a spin degenerate level on each QD at a bias of $V_{SD} = \pm 2\,\mathrm{mV}$. Triangles for both bias polarities are plotted in the same figure. c) Allowed transport for positive bias along the (0, 1)→(1, 2) charge transition. d) Pauli spin blockade for negative bias along the (0, 1)→(1, 2) charge transition.

Pauli spin blockade

Figures 8(a) (experiment) and (b) (simulation) further reveal an additional transport-restricting phenomenon in DQDs: At the (0, 1)→(1, 2) charge transition the finite bias triangles corresponding to negative a negative bias, marked by a black arrow, are partially suppressed compared to their positive bias counterpart in the experimental data. Conversely, at the (1, 0)→(2, 1) charge transition current suppression is found for positive bias. This effect is more pronounced in the simulation in fig. 8(b), where current, which is (merely) suppressed in the experimental finite bias triangles, completely vanishes. The current blockade is based on the spin properties of electrons. According to the Pauli exclusion principle, two electrons of parallel spin cannot occupy the same single spatial orbital [39], which introduces additional constraints for electron transport across the DQD system and the effect observed in figs. 8(a) and (b) is referred to as Pauli spin blockade (PSB) [6].

For a current rectification due to the Pauli exclusion principle to occur, a spatial orbital must be partially filled such that the next available ground state only accepts an electron with a predetermined spin orientation [40]. In the case of conventional odd-even spin filling, current blockade is found for interdot charge transitions along which the total combined number of electrons on both QDs is even [41]. In the following, the principle of PSB is exemplarily discussed for the (0,1)→(1,2) charge transition, where one electron occupies the right QD and the total number of electrons on the DQD during the interdot charge transition is two.

Because the spin blockade effect is of many-particle nature, a description requires consideration of the two-electron spin states in the system: The two electrons can either form a spin singlet (anti-parallel spins in the same spatial orbital) or a spin triplet (parallel or anti-parallel spins in different orbitals). Transport across the DQD for a positive voltage bias is schematically illustrated in fig. 8(c). A spin-down electron is situated in the right QD outside the transport window. Because the triplet T(0,2) state is not available, only a spin-down electron can selectively tunnel from the drain reservoir into the ground state on the right QD to form the singlet state S(0,2). The left QD is unoccupied and in the limit of small tunnel coupling between the two QDs the singlet and triplet states S(1,1) and T(1,1) are nearly energetically degenerate (and the split is not resolvable) within the ground state level of the left QD. Consequently, aside from the drain-to-DQD tunneling process, no further spin selective restrictions apply and transport across the DQD is recovered within the finite bias triangles.

In contrast, if a negative voltage bias is applied across the DQD, an electron entering the left QD from the source can either form the S(1,1) or T(1,1) state and thus its spin orientation is arbitrary. If a spin down electron enters the left QD, it can flow through the singlet states S(1,1) and S(0,2) without restrictions [39]. Once a spin-up electron enters the left QD it forms the T(1,1) state, but the right QD only offers the spin singlet S(0,2) and transport from the left to the right QD is blocked by the Pauli exclusion principle. This situation is illustrated in fig. 8(d). Unless the level on the left QD is aligned with μ_S and the T(1,1) state can be exchanged for a S(1,1) state, the electron on the left QD becomes trapped and transport through the DQD is blocked [41]. Finally, if the bias window is sufficiently large such that the triplet T(0,2) is accessible, spin blockade is lifted [41]. Neglecting contributions from the exchange interaction, this lifting of the spin blockade occurs if an excited state $\mu_0^\mathrm{R}(0,2)$ (not included in fig. 8(b/d)) enters the transport window [40] and a fraction of the finite bias triangles remains conductive as can be seen in the experimental data in fig. 8(a), where current in the finite bias triangle tips is not suppressed for the spin blockaded features.

PSB provides direct experimental access to spin states in DQDs and has thus been studied theoretically and experimentally for a variety of regimes and material systems, see for example refs. [39, 41–44]. A detailed description of the two-electron spin singlet and triplet states and their relevance for Pauli spin blockade is found in ref. [6].

Variation of the interdot tunnel coupling

Up until this point the DQD system has been described in the framework of the constant interaction model, assuming negligible tunnel coupling with respect to the electrostatic coupling between the left and right QD [6]. Interactions between the two QDs are then limited to purely capacitive effects. This holds true in the so-called weak interdot coupling limit, where electronic wave functions are fully localized and confined to either the left or right QD and the DQD acts as an artificial molecule with ionic bonds [45]. In contrast, if the interdot tunnel coupling exceeds the weak coupling limit, wave functions extend across both QDs and electrons in the DQD become delocalized. These delocalized electrons resemble valence electrons in molecules. Consequently, the DQD behaves like an artificial molecule with covalent bonds [45, 46]. A detailed theoretical description of a DQD including both, tunnel- and capacitive-coupling related effects can be found in refs. [5, 47].

To introduce the impact of the interdot tunnel coupling, in the following, the simplified description of a DQD based on tunnel couplings and illustrated in fig. 9(a) is considered: The left and right QD have one ground state energy level E_L and E_R each and the two QDs are coupled by the interdot tunnel coupling Ω. The level E_L is tunnel coupled to the source- and E_R to the drain-contact, characterized by the tunneling rates Γ_L and Γ_R. The tunnel rates essentially describe at what rate electrons are expected to hop across the respective tunnel barrier. Further, the energetic level detuning between the two QDs is given by $\Delta = E_L - E_R$.

The hamiltonian $\hat{H} = \hat{H}_0 + \hat{H}_T$ where $\hat{H}_0$ is the Hamiltonian of the uncoupled DQD system and $\hat{H}_T$ introduces the finite tunnel coupling between levels on both QDs [5] describes the DQD system outlined in fig. 9(a). Eigenstates of this Hamiltonian are given by the delocalized molecular bonding (B) and antibonding (AB) states

$$\begin{aligned} \psi_B &= \alpha\Phi_L + \beta\Phi_R \\ \psi_{AB} &= \beta\Phi_L + \alpha\Phi_R \end{aligned} \tag{29}$$

which are the result of a superposition of the single QD states $\Phi_{L/R}$ [6]. The energy of the bonding orbital is decreased compared to the lower of the two levels $E_{L/R}$ while the energy of the antibonding orbital is increased compared to the energetically higher unperturbed level [46]. The energetic difference

$$\Delta E_{AB\text{-}B} = E_{AB} - E_B = \sqrt{\Delta^2 + (2\Omega)^2} \tag{30}$$

depends on the detuning Δ [45].

Figure 9(b) illustrates the relation between the energetic position of the bonding and antibonding states and the uncoupled QD levels $E_{L/R}$ as a function of the detuning Δ. While

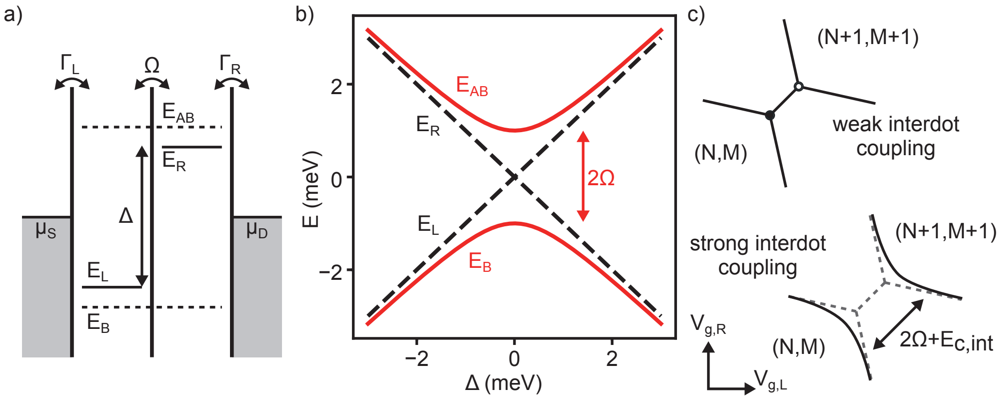

Figure 9: Impact of the interdot tunnel coupling. a) Schematic illustration of a simplified DQD in a tunnel coupling framework. b) Calculated energies of the bonding and antibonding orbitals as a function of the level detuning Δ for $\Omega = 1\,\mathrm{meV}$. c) Charge stability diagram in the limit of weak and strong interdot tunnel coupling.

for large Δ, the energetic position of the bonding and antibonding orbitals approaches that of the unperturbed states, the minimum energetic distance is bound by 2Ω at $\Delta = 0$. Consequently, finite tunnel coupling between the two QDs introduces an avoided-crossing behavior for eigenenergies of the DQD [5]. The avoided-crossing manifests directly in the DQDs charge stability diagram. First, the TPs corresponding to the electron- and hole-transport cycle are further split by an additional 2Ω. Second, the charging lines directly follow the hyberbolic behavior shown in fig. 9(b), which introduces a bending most visible in close vicinity to the unperturbed TP positions [46]. This change introduced to the charge stability diagram by including the interdot tunnel coupling is schematically illustrated in fig. 9(c).

Finally, the interdot tunnel coupling introduces the possibility to detect currents along the charging lines in the charge stability diagram. In the absence of a voltage bias across the device, an unperturbed level of the left (right) QD is aligned with the source (drain) reservoir along charging lines. With wave functions extending across both QDs, however, electrons may enter a delocalized state from the source (drain) reservoir and leave the DQD through the drain (source) reservoir. If a finite voltage bias is applied, this effect can give rise to a detectable current band with an energetic width corresponding to the transport window eV_{SD} along the charging lines. With increasing Δ, the bonding and antibonding molecular states become more localized in one of the QDs and thus the probability of an electron traveling across both QDs decreases [48]. In the case $\Delta \gg \Omega$ the tunneling rates for a state mainly localized in the left (right) QD can then be approximated by

$$\begin{aligned}\Gamma'_{L(R)} &\approx \Gamma_{L(R)}\\ \Gamma'_{R(L)} &\approx \frac{\Gamma_{R(L)}\Omega^2}{\Delta^2}\end{aligned} \tag{31}$$

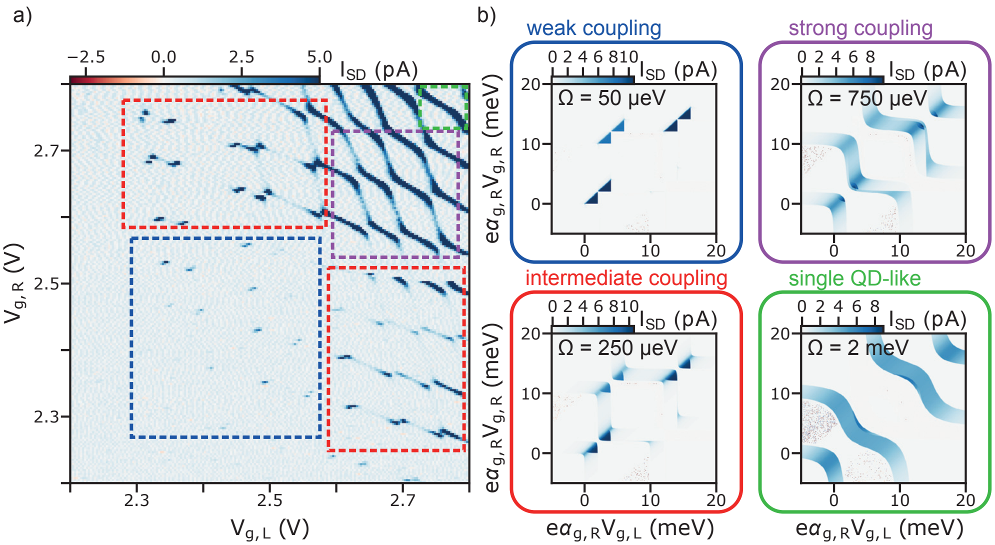

Figure 10: Charge stability diagram of a DQD at different interdot tunnel couplings. a) Measurement on a DQD with an AC excitation of $V_{SD} = 2\,\mathrm{mV}$ rms. For increasing occupancies the tunnel barriers effectively decrease in height and different interdot coupling regimes are accessed. b) Simulations of the current through a DQD with one spin degenerate level on each QD with different interdot couplings Ω.

where Γ'_L and Γ'_R describes the tunneling rate between the molecular state and the source and drain contact, respectively [48].

Experimentally two methods can be employed to tune the interdot tunnel coupling: Direct, electrostatic tuning of the tunnel barrier between the two QDs is possible via gate control and an effective decrease of the tunnel barrier height can be obtained by increasing the QD occupancies. Fig. 10(a) shows the experimentally detected charge stability diagram of a DQD over a wide range of occupancies (N, M). As a result of the decreased barrier height and thus mainly increasing Ω, the current signals undergo significant changes and can be sorted into separate regimes. The different characteristic interdot coupling regimes are illustrated by simulations of a DQD with $E_C = 10\,\mathrm{meV}$ and different Ω in fig. 10(b). For low DQD occupancies/Ω the DQD is in a weak coupling regime (labelled in blue), characterized by well defined finite bias triangles. As Ω increases, currents manifest along charging lines and first indications of an avoided crossing reshape the finite bias triangles. This characteristic range (see red label) is in this work attributed to an intermediate coupling regime. As Ω approaches the order of magnitude of E_C, first finite bias triangles vanish and clear avoided-crossings occur near the TP locations, indicating a strong interdot coupling regime (purple label). Finally, for further increased Ω, charging lines become more diagonal and regions of constant charge no longer appear in a well-defined honeycomb-pattern (see green label). In this last regime, the QD states are widely delocallized across the DQD and the system effectively behaves like a single QD coupled to two plunger gates. It is noteworthy that in experiments, currents can also be observed along the charge transfer line for increasing tunnel couplings. These currents are then the result of higher order cotunneling transport processes [43] and are not accounted for in the simulations in fig. 10(b).

4 Quantitative description: Rate equations

A qualitative understanding of transport phenomena in QD systems was developed in the previous section based on the constant interaction model. Practically, however, a quantitative description is needed for a direct comparison between experiments and theory, which in turn can give valuable insights into parameters of the experiment, such as temperatures and tunnel couplings. A quantitative approach based on classical rate equations for sequential electron transport across voltage [25, 49] and thermally [50] biased QDs was introduced in the early 1990s when experimental progress made controlled measurements on metal [51] and semiconductor [52–54] single electron transistors possible [55–57].

The underlying concept of classical rate equations is based on the time evolution of the occupation probability

$$\frac{dP_\alpha}{dt} = \sum_\beta (W_{\beta\to\alpha}P_\beta - W_{\alpha\to\beta}P_\alpha) \tag{32}$$

of a state $|\alpha\rangle$ [58], described by the total transition rates $W_{\alpha\to\beta}$ at which the system changes from state $|\alpha\rangle$ to other states $|\beta\rangle$ [59]. For a vector $\vec{P}$ containing the occupation probabilities of all relevant states of a system, eq. (32) can be expressed in matrix form

$$\frac{d\vec{P}}{dt} = \mathbf{W}\vec{P} \tag{33}$$

where the elements of the transition matrix are given by $W_{\alpha\beta} = W_{\beta\to\alpha}$ for $\alpha \neq \beta$ and $W_{\alpha\alpha} = -\sum_{\beta\neq\alpha} W_{\alpha\to\beta}$ [58]. For the stationary case, $d\vec{P}/dt = 0$, where on average all P_α remain constant in time and in combination with the normalization condition $\sum_\alpha P_\alpha = 1$, eq. (33) results in set of homogeneous equations which can be solved for the occupation probabilities of a given system [60]. With both the rates and the occupation probabilities known, arbitrary particle currents within the system can directly be calculated by summation of the relevant rates, weighted by the occupation probabilities of states involved in the transitions.

The applicability of classical rate equations to QD systems is in the following demonstrated by considering the example of a single electron transistor (SET), consisting of a QD, weakly tunnel coupled to a left (L) and right (R) electron reservoir via energy independent $\Gamma_{L/R}$ and capacitively coupled to a gate electrode. This example is of particular interest not only for its illustrative simplicity but because it often suffices to accurately reproduce and fit experimental data. As such, the following model is extensively used for thermometry and fits for tunnel couplings in papers ii and iii. Suppose for simplicity that the Fermi-energy is set to zero and assume that the single-particle energy spacing of the QD is sufficiently large such that only one spin degenerate resonance is accessible for transport and $\Gamma_{\mathrm{L,R}} \ll k_{\mathrm{B}}\mathrm{T}_{\mathrm{L,R}}$, where T_{L} and T_{R} denote the temperatures in the left and right electron reservoir. The latter condition ensures negligible lifetime broadening of the QD states in relation to the other energy scales in the system [61]. The QD resonance can be populated by $\mathrm{N} = 0, 1, 2$ electrons with its electro-chemical potentials $\mu_1 = -e\alpha_{\mathrm{g}}\mathrm{V}_{\mathrm{g}}$ and $\mu_2 = \mathrm{E}_{\mathrm{C}} - e\alpha_{\mathrm{g}}\mathrm{V}_{\mathrm{g}}$ corresponding to the many-particle QD states, obtained from the constant interaction model. Further, the lead electron reservoirs are assumed in a fully thermalized state and thus the occupation probability of lead states is described by the Fermi-Dirac distribution, $f_{\mathrm{L/R}}(\mu_{\mathrm{N}}) = f(\mu_{\mathrm{N}}, \mp e\mathrm{V}_{\mathrm{SD}}/2, \mathrm{T}_{\mathrm{L/R}})$ in eq. (11). The electro-chemical potential of the left and right lead is determined by the value of a symmetric bias V_{SD} applied between the two leads.

In a strict sequential tunneling framework, where no cotunneling effects are present (small $\Gamma_{\mathrm{L,R}}$) only transitions between QD states differing in electron occupancy by exactly one remain relevant if the charging energy $\mathrm{E}_{\mathrm{C}} \gg e\mathrm{V}_{\mathrm{SD}}, k_{\mathrm{B}}\mathrm{T}_{\mathrm{L,R}}$ greatly exceeds the external bias and temperatures [58]. A change of the QD occupancy occurs via transport processes involving either the left or right lead and four charge state transitions remain possible: $0 \to 1$, $1 \to 0$, $1 \to 2$ and $2 \to 1$. Thus, the eight possible total transition rates

$$\begin{aligned} \mathrm{W}_{\mathrm{L/R}}^{0\to1} &= 2\Gamma_{\mathrm{L/R}} f_{\mathrm{L/R}}(\mu_1) & \qquad \mathrm{W}_{\mathrm{L/R}}^{1\to2} &= \Gamma_{\mathrm{L/R}} f_{\mathrm{L/R}}(\mu_2) \\ \mathrm{W}_{\mathrm{L/R}}^{1\to0} &= \Gamma_{\mathrm{L/R}}\left(1 - f_{\mathrm{L/R}}(\mu_1)\right) & \qquad \mathrm{W}_{\mathrm{L/R}}^{2\to1} &= 2\Gamma_{\mathrm{L/R}}\left(1 - f_{\mathrm{L/R}}(\mu_2)\right) \end{aligned} \tag{34}$$

of the system are a function of the tunnel couplings $\Gamma_{\mathrm{L/R}}$ between the QD and the leads, weighted by the probability of finding either a populated or a vacant state in the leads for electrons to tunnel from or to [58, 62]. The factor of two in selected rates in eq. (34) is a result of the spin degeneracy: Transitions into (out of) the empty (full) QD resonance, $\mathrm{N} = 0$ ($\mathrm{N} = 2$), allow for an electron of either spin orientation to enter (leave) the QD. In contrast, if $\mathrm{N} = 1$ transport into and out of the QD is spin selective.

Because either only μ_1 or μ_2 is considered accessible for transport at any given voltage bias and temperature, the $0 \leftrightarrow 1$ and $1 \leftrightarrow 2$ QD charge state transitions become fully independent. Then, the probability $\mathrm{P}_{\mathrm{N}}^{\mathrm{N}'\leftrightarrow\mathrm{N}}$, of finding N electrons on the QD if the $\mathrm{N}' \leftrightarrow \mathrm{N}$ charge state transition is accessible as a function of the total transition rates

$$\begin{aligned} \mathrm{P}_0^{0\leftrightarrow1} &= \frac{\sum_{i=\mathrm{L,R}} \mathrm{W}_i^{1\to0}}{\sum_{i=\mathrm{L,R}}\left(\mathrm{W}_i^{0\to1} + \mathrm{W}_i^{1\to0}\right)} & \qquad \mathrm{P}_1^{1\leftrightarrow2} &= \frac{\sum_{i=\mathrm{L,R}} \mathrm{W}_i^{2\to1}}{\sum_{i=\mathrm{L,R}}\left(\mathrm{W}_i^{1\to2} + \mathrm{W}_i^{2\to1}\right)} \\ \mathrm{P}_1^{0\leftrightarrow1} &= \frac{\sum_{i=\mathrm{L,R}} \mathrm{W}_i^{0\to1}}{\sum_{i=\mathrm{L,R}}\left(\mathrm{W}_i^{0\to1} + \mathrm{W}_i^{1\to0}\right)} & \qquad \mathrm{P}_2^{1\leftrightarrow2} &= \frac{\sum_{i=\mathrm{L,R}} \mathrm{W}_i^{1\to2}}{\sum_{i=\mathrm{L,R}}\left(\mathrm{W}_i^{1\to2} + \mathrm{W}_i^{2\to1}\right)} \end{aligned} \tag{35}$$

[62] is the result of the normalization conditions $\mathrm{P}_0^{0\leftrightarrow1} + \mathrm{P}_1^{0\leftrightarrow1} = 1$ and $\mathrm{P}_1^{1\leftrightarrow2} + \mathrm{P}_2^{1\leftrightarrow2} = 1$ [63]. With all relevant transition rates and occupation probabilities now expressed by the

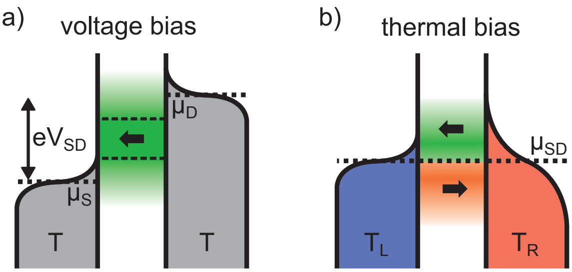

Figure 11: Transport window under voltage and thermal bias. a) Schematic illustration of the transport window for a voltage biased QD. Dashed lines enclose the current-saturated region. b) Schematic illustration of the transport window for a thermally biased QD. Black arrows in (a) and (b) indicate the direction of the net electron flow through a QD level situated in the indicated energy range.

bare tunnel couplings and the bias and temperature applied to the leads, currents through the system can be quantified via experimentally accessible parameters only. In the stationary case, the current through the left- equals that through the right tunnel barrier [58, 63] and an electron travelling through the system from the right- to the left lead defines a positive current contribution. Consequently, with eqs. (34) and (35), the charge current through μ_1

$$\begin{aligned} \mathrm{I}_{0\leftrightarrow 1} &= e\left(\Gamma_\mathrm{L}\left(1-f_\mathrm{L}(\mu_1)\right)\mathrm{P}_1^{0\leftrightarrow 1} - 2\Gamma_\mathrm{L} f_\mathrm{L}(\mu_1)\mathrm{P}_0^{0\leftrightarrow 1}\right) = \\ &= 2e\frac{\Gamma_\mathrm{L}\Gamma_\mathrm{R}}{\Gamma_\mathrm{L}+\Gamma_\mathrm{R}+\Gamma_\mathrm{L} f_\mathrm{L}(\mu_1)+\Gamma_\mathrm{R} f_\mathrm{R}(\mu_1)}\left(f_\mathrm{R}(\mu_1)-f_\mathrm{L}(\mu_1)\right) \end{aligned} \tag{36}$$

is calculated from the probability current [58, 62, 63]. Conversely, the current through μ_2 is given by

$$\begin{aligned} \mathrm{I}_{1\leftrightarrow 2} &= e\left(2\Gamma_\mathrm{L}\left(1-f_\mathrm{L}(\mu_2)\right)\mathrm{P}_1^{0\leftrightarrow 1} - \Gamma_\mathrm{L} f_\mathrm{L}(\mu_2)\mathrm{P}_0^{1\leftrightarrow 2}\right) = \\ &= 2e\frac{\Gamma_\mathrm{L}\Gamma_\mathrm{R}}{2\Gamma_\mathrm{L}+2\Gamma_\mathrm{R}-\Gamma_\mathrm{L} f_\mathrm{L}(\mu_2)-\Gamma_\mathrm{R} f_\mathrm{R}(\mu_2)}\left(f_\mathrm{R}(\mu_2)-f_\mathrm{L}(\mu_2)\right) \end{aligned} \tag{37}$$

[62] and the total current in the system is $\mathrm{I}_\mathrm{SD} = \mathrm{I}_{0\leftrightarrow 1} + \mathrm{I}_{1\leftrightarrow 2}$.

Eqs. (36) and (37) immediately highlight a key concept: Net currents through a QD level μ_N are driven by an occupation difference between the leads, described by the Fermi-Dirac distributions, at the energetic position of the QD level. The amplitude and sign of the current through μ_N is determined by the magnitude and sign of $f_\mathrm{R}(\mu_\mathrm{N}) - f_\mathrm{L}(\mu_\mathrm{N})$. A non-vanishing difference $f_\mathrm{R}(\mu_\mathrm{N}) - f_\mathrm{L}(\mu_\mathrm{N}) \neq 0$ defines a transport window, describing the energy range where a non-zero net current flows through available QD levels located therein, and can be achieved either by an applied voltage- or thermal bias between the left and right lead. The resulting transport window is illustrated for a voltage- and thermal bias in fig. 11(a) and (b), respectively, where the Fermi-Dirac distributions in the leads are indicated by coloured areas.

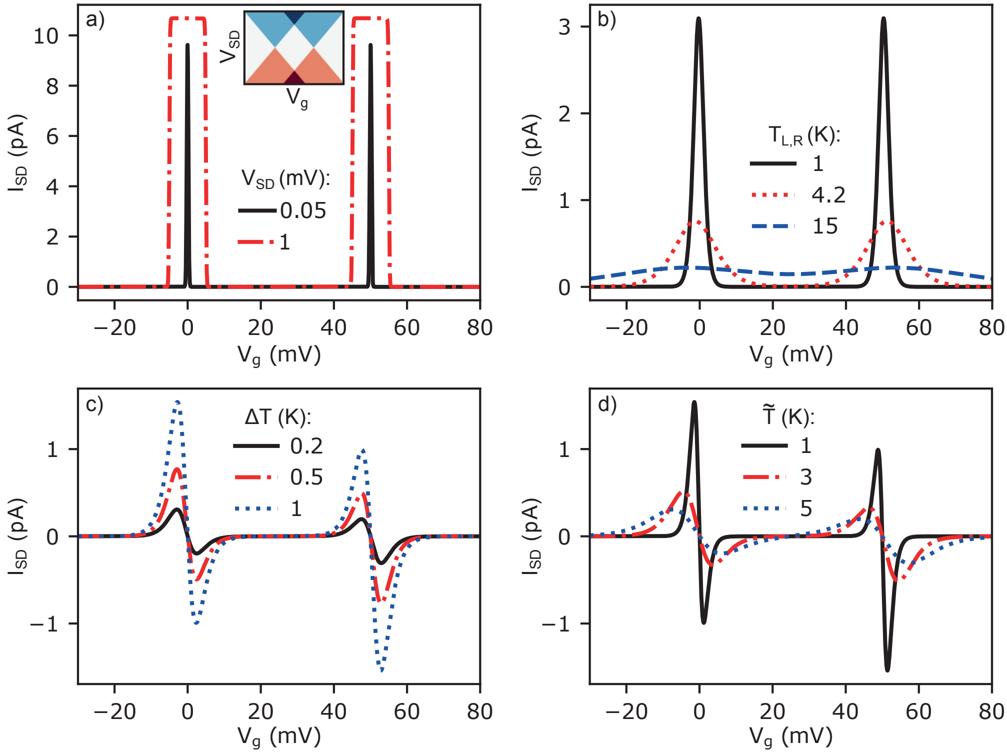

Figure 12: **Interplay between bias and temperature in thermally and voltage biased QDs.** Current through a spin degenerate resonance $I_{0\leftrightarrow1} + I_{1\leftrightarrow2}$, calculated based on classical rate equations with $\Gamma_{L,R} = 100\,\mathrm{MHz}$, $\alpha_g = 0.1$ and $E_C = 5\,\mathrm{meV}$. a) $T_{L,R} = 100\,\mathrm{mK}$ and varying V_{SD}. Inset: Calculated charge stability diagram. b) $V_{SD} = 0.1\,\mathrm{mV}$ and varying $T_{L,R}$. c) $V_{SD} = 0$, $\tilde{T} = (T_L + T_R)/2 = 2\,\mathrm{K}$ and varying $\Delta T = T_R - T_L$. d) $V_{SD} = 0$, $\Delta T = 0.5\,\mathrm{K}$ and varying $\tilde{T}$.

For a voltage bias, the electro-chemical potentials of the source and drain leads, μ_S and μ_D shift against each other, spanning open a unidirectional transport window as illustrated in fig. 11(a) for a positive bias. In contrast to the previous qualitative discussions, the transport windows size extends beyond $eV_{SD} = \mu_D - \mu_S$ by several $k_B T_{L/R}$ as a result of the finite temperatures T_L and T_R in the source and drain leads, smearing the respective electron distributions. The current magnitude through a QD resonance in the transport window subsequently depends on the interplay of V_{SD} and $T_{L/R}$. To illustrate this concept, the current through the voltage biased model system $I_{0\leftrightarrow1} + I_{1\leftrightarrow2}$ as a function of the gate voltage V_g is calculated for experimentally realistic parameters ($E_C = 5\,\mathrm{meV}$, $\Gamma_{L,R} = 100\,\mathrm{MHz}$, $\alpha_g = 0.1$) in fig. 12(a) and (b). The results demonstrate that both, an increase in the voltage bias (fig. 12(a)) and overall temperature $T_{L,R}$ (fig. 12(b)) independently widen the transport window. While an increase of V_{SD}, however, retains the sharpness of Coulomb peaks, an increasing $T_{L,R}$ leads to considerable smearing of the features to the point where for $T_{L,R} \sim E_C$ the coulomb blockade effect is no longer observable.

Fig. 12(a) further illustrates that for $E_C \gg eV_{SD} \gg k_B T_{L,R}$ (red curve) the currents $I_{0\leftrightarrow 1}$ and $I_{1\leftrightarrow 2}$ saturate and become independent of the temperature in the leads. In eqs. (36) and (37), this corresponds to the regime where $f_R \approx 1$ and $f_L \approx 0$ ($f_L \approx 1$ and $f_R \approx 0$) for $V_{SD} > 0$ ($V_{SD} < 0$) and if further $\Gamma_L \sim \Gamma_R$, the saturation currents

$$\begin{aligned} I_{+}^{0\leftrightarrow 1} &= \frac{2e\Gamma_L\Gamma_R}{2\Gamma_R + \Gamma_L} & \qquad I_{+}^{1\leftrightarrow 2} &= \frac{2e\Gamma_L\Gamma_R}{\Gamma_R + 2\Gamma_L} \\ I_{-}^{0\leftrightarrow 1} &= \frac{-2e\Gamma_L\Gamma_R}{\Gamma_R + 2\Gamma_L} & \qquad I_{-}^{1\leftrightarrow 2} &= \frac{-2e\Gamma_L\Gamma_R}{2\Gamma_R + \Gamma_L} \end{aligned} \tag{38}$$

are found for a positive (+) and negative (-) voltage bias [58]. This saturation regime is interesting because instead of fits to Coulomb peaks with up to four free parameters ($\Gamma_{L/R}$, $T_{L/R}$), which often do not yield unique results, the problem of finding tunnel couplings is reduced to a simple comparison of $I_{+/-}^{N'\leftrightarrow N}$. A unique estimation of Γ_L and Γ_R, however, still requires knowledge on whether the measured currents originate from a $0 \leftrightarrow 1$ or $1 \leftrightarrow 2$ type charge transition. In experiments clear identification of the transition type is not necessarily trivial.

Insight into the transition type is accessible from currents observed in a thermally biased configuration ($\mu_{SD} = \mu_S = \mu_D$, $T_L \neq T_R$). The transport window under thermal bias has an an energetic extent corresponding to the smearing of the Fermi-Dirac distributions and is no longer unidirectional. Instead, $f_R(\mu_N) - f_L(\mu_N)$ is of opposite polarity for $\mu_N > \mu_{SD}$ compared to $\mu_N < \mu_{SD}$ and vanishes for $\mu_N = \mu_{SD}$. The sketch in fig. 11(b) illustrates the transport window for the case $T_R > T_L$ and conceptually visualizes how each QD level μ_N yields a distinct thermoelectric current wiggle when pulled through the transport window by variation of V_g. In 12(c) and (d) calculations of the thermoelectric currents are plotted for realistic experimental parameters (compare to paper III) and demonstrate the interplay of the temperature difference $\Delta T = T_R - T_L$ and the average temperature $\widetilde{T} = (T_L + T_R)/2$. The width of the thermally induced current signal along V_g is found to scale with $\widetilde{T}$, while the peak amplitudes are dependent on ΔT. Because electrons flow from hot to cold above μ_{SD} and vice versa, knowing the sign of the thermoelectric current at any given energetic QD level position relative to μ_{SD} is sufficient to immediately identify the hot electron reservoir in experiments.

Further information about the QD system is contained in the distinct asymmetry between the current amplitudes associated with a single level μ_N above or below μ_{SD} in the transport window [64]. The asymmetry is characteristically different for $0 \leftrightarrow 1$ and $1 \leftrightarrow 2$ type charge transitions and is a result of spin degeneracy: In a configuration where $\mu_N - \mu_{SD} \gtrsim k_B T_{L,R}$ transport occurs through a mostly unoccupied QD level ($P_{N-1} > P_N$) [65] and thus the overall current through the level is predominantly determined by the tunneling process of an electron into the resonance. For a $1 \leftrightarrow 2$ type transition, this process is spin selective and thus the current is suppressed compared to a $0 \leftrightarrow 2$ type charge transition. The situation is reversed in a configuration where $\mu_\mathrm{N} - \mu_\mathrm{SD} \lesssim -k_\mathrm{B}\mathrm{T}_\mathrm{L,R}$ where the QD level is mostly occupied ($\mathrm{P}_\mathrm{N-1} < \mathrm{P}_\mathrm{N}$) and the current is suppressed in a $0 \leftrightarrow 1$ type transition as a result of the spin selective tunneling process out of the resonance [65]. Consequently, the thermoelectric current amplitude asymmetry in a purely thermally biased QD provides direct access to distinguish between $0 \leftrightarrow 1$ and $1 \leftrightarrow 2$ type charge transitions and highlights the application of measurements under thermal bias for complementary spectroscopy purposes.

The previous calculations demonstrate that classical rate equations are a capable tool to quantify transport in quantum dot systems. Further details of classical rate equations applied to a single QD are provided in refs. [58, 62, 63] and for a comparable description of transport phenomena in a serial DQD the interested reader is referred to ref. [66]. While the concept of classical rate equations is illustrative and reproduces various transport phenomena in quantum dot systems, it can quickly become obscure for complex models. Therefore, more general rate based descriptions, capable of describing the full time evolution of the many-particle states including various higher order transport processes such as cotunneling effects are needed. In particular, models described by so called generalized master equations [67, 68] are applicable to quantum dot systems described by a hamiltonian $\hat{\mathrm{H}} = \hat{\mathrm{H}}_\mathrm{S} + \hat{\mathrm{H}}_\mathrm{leads} + \hat{\mathrm{H}}_\mathrm{C}$ consisting of terms describing the QD system, $\hat{\mathrm{H}}_\mathrm{S}$, the leads, $\hat{\mathrm{H}}_\mathrm{leads}$ as well as the coupling between the leads and the QD system, $\hat{\mathrm{H}}_\mathrm{C}$ [69]. A more generalized version of eq. (33) is then given by the von Neumann equation

$$i\hbar\frac{d}{dt}\hat{\rho} = -[\hat{\rho}, \hat{\mathrm{H}}] \tag{39}$$

which describes a kinetic equation for the density operator $\hat{\rho}$ of the full system [68]. For the purpose of studying transport in QD systems, the relevant physics is contained in the time evolution of the quantum dot system alone and thus the problem can be simplified by tracing out the lead degrees of freedom to obtain a reduced density operator $\hat{\rho}_\mathrm{r} = \mathrm{Tr}_\mathrm{leads}(\hat{\rho})$ [70]. The task of finding the equation of motion, corresponding to the right hand side of eq. (39) is, for the reduced density operator $\hat{\rho}_\mathrm{r}$ not necessarily trivial to solve and there exist a variety of approximate approaches [67–69, 71] differing widely in the choice of assumptions and complexity [70].

For instance, by restriction to diagonal elements of $\hat{\rho}_\mathrm{r}$ and uncorrelated transitions only, one obtains what is known as Pauli master equation, which resembles exactly the classical rate equation approach [68]. An expansion of the Pauli rate equation to further consider correlated transitions by systematically including all second order terms in the tunnel coupling yields the real time diagrammatic (RTD) technique, which is capable of describing co- and pair-tunneling processes [69, 72]. The inclusion of coherences in the system, contained within off-diagonal elements of $\hat{\rho}_\mathrm{r}$, requires more complex treatments by so called quantum master equations [68, 73], among other Lindblad, Redfield and von Neumann-

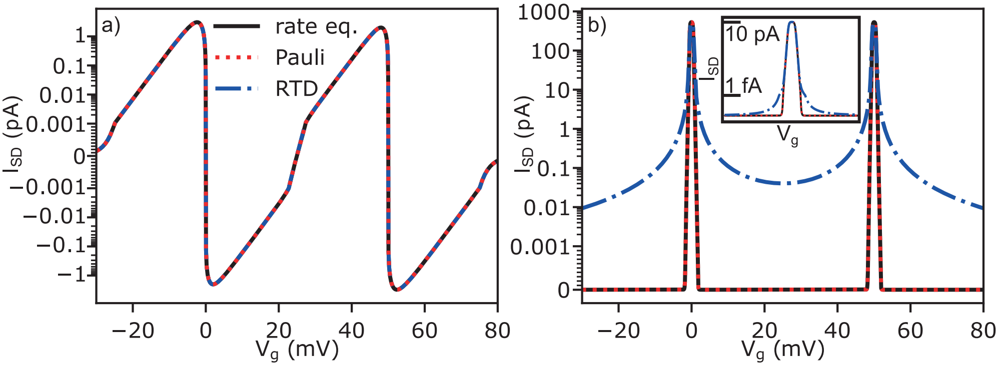

Figure 13: Comparison of classical rate equations to QmeQ calculations. Calculations of $I_{0\leftrightarrow 1}+I_{1\leftrightarrow 2}$ based on the classical rate equation model compared to currents calculated using different master equation approaches implemented in QmeQ. a) $\Gamma_{L,R} = 100\,\mathrm{MHz}$, $V_{SD} = 0$ and $T_L = 1\,\mathrm{K}$, $T_R = 3\,\mathrm{K}$. b) $\Gamma_{L,R} = 5\,\mathrm{GHz}$, $V_{SD} = 100\,\mu\mathrm{V}$ and $T_{L,R} = 0.1\,\mathrm{K}$. Inset: $\Gamma_{L,R} = 100\,\mathrm{MHz}$, $V_{SD} = 100\,\mu\mathrm{V}$ and $T_{L,R} = 0.1\,\mathrm{K}$. The scale in (a), (b) and the inset is logarithmic with a linear range between $\pm 1\,\mathrm{fA}$.

type approaches [67, 68, 70]. A variety of different master equation approaches are implemented in the open source python package QmeQ (short for Quantum master equation for Quantum dot transport calculations) [74] with the possibility to further include electron-phonon coupling effects [75]. The Pauli rate equation approach via QmeQ is used extensively for the simulations in paper III and to illustrate transport concepts in this thesis. Relevant parameters for simulations shown in this thesis are detailed in the appendix.

Because the simple model based on classical rate equations presented here is used to fit experimental data in papers II and III a comparison to more advanced master equation approaches is of interest. Therefore, fig. 13(a) compares thermoelectric currents for parameters comparable to those most demanding for the model found in paper III, calculated by classical rate equations as well as Pauli master equations and RTD with QmeQ. The results confirm that the inclusion of higher order effects does not lead to deviations between RTD and classical rate equations for parameters present in the experiment. Deviations between RTD and the more simple models become clear when the tunnel couplings are increased from $\Gamma_{L/R} = 100\,\mathrm{Mhz}$ to $\Gamma_{L/R} = 5\,\mathrm{Ghz}$ in fig. 13(b), where voltage bias driven currents calculated by RTD show significant cotunneling in the Coulomb blockaded gate range. In contrast, for $\Gamma_{L/R} = 100\,\mathrm{Mhz}$ (see inset) the magnitude of cotunneling currents is found to be in the single digit fA range, which is around two orders of magnitude lower than the noise floor in experiments. Consequently, the simple classical rate equation model is deemed sufficient to fit experimental data for temperatures and tunnel couplings. Finally, it should however be noted that while first order calculations yield good results for charge currents, lifetime broadening and cotunneling effects are highly relevant for the accurate calculation of energy currents [76]. For instance, this becomes relevant for efficiency estimates of the thermoelectric power generation in quantum dot devices, where knowledge of the heat current is required and lowest order classical rate equations no longer give realistic results [65, 76, 77].

Design of nanowire based quantum dot systems

Up to this point in the thesis, the conceptual introduction of transport through QDs clearly demonstrates a key ability of such systems: Individual electrons (or holes) can precisely be controlled and shuffled between QDs, thus giving direct access to quantum mechanical properties and phenomena. Consequently, QD systems provide promising platforms for fundamental research as well as quantum electronic and spintronic applications and have gained tremendous popularity within the nanoscience community[4–6, 78]. With modern-day nanofabrication capabilities [79] experimental realizations of electronic QD-based devices are available in a vast variety of materials and conceptual designs adapted for numerous different applications. These device implementations range from lateral QDs based on two-dimensional electron and hole gases in planar heterostructures [80, 81] and material confined [82–85] as well as electrostatically defined QDs in nanowires [86] to single atom transistors [87, 88]. Other prominent examples include self-assembled [89–92] and vertical [93] QDs, molecular junctions [94–96] and donor defined QD regions in silicon [97, 98]. A complete list or detailed discussion of the numerous approaches to the design of QD systems, however, could fill a thesis of its own. For the interested reader, the review articles in refs. [6, 99–101] are recommended as a starting point for further information beyond the scope of this chapter.

Three common building blocks are required across the various different devices: (1) The QD system itself, which can be vastly different, depending on the device purpose. This QD system can contain among other single- or numerous serial- [102, 103], purely coulomb coupled- [104] as well as parallel tunnel-coupled QDs [105, 106] or hybrid systems between the aforementioned [107]. (2) Electron (or hole) reservoirs, serving as source and drain contact, tunnel coupled to the QD system. (3) An electrostatic gate structure in close spatial vicinity to the QDs to individually address each QD in the device and to optionally tune the tunnel couplings between the QDs as well as between the QDs and the contacts. In this thesis, only III-V semiconductor nanowire based serial QD systems are explicitly discussed and some of the devices include, in addition to these building blocks, means to

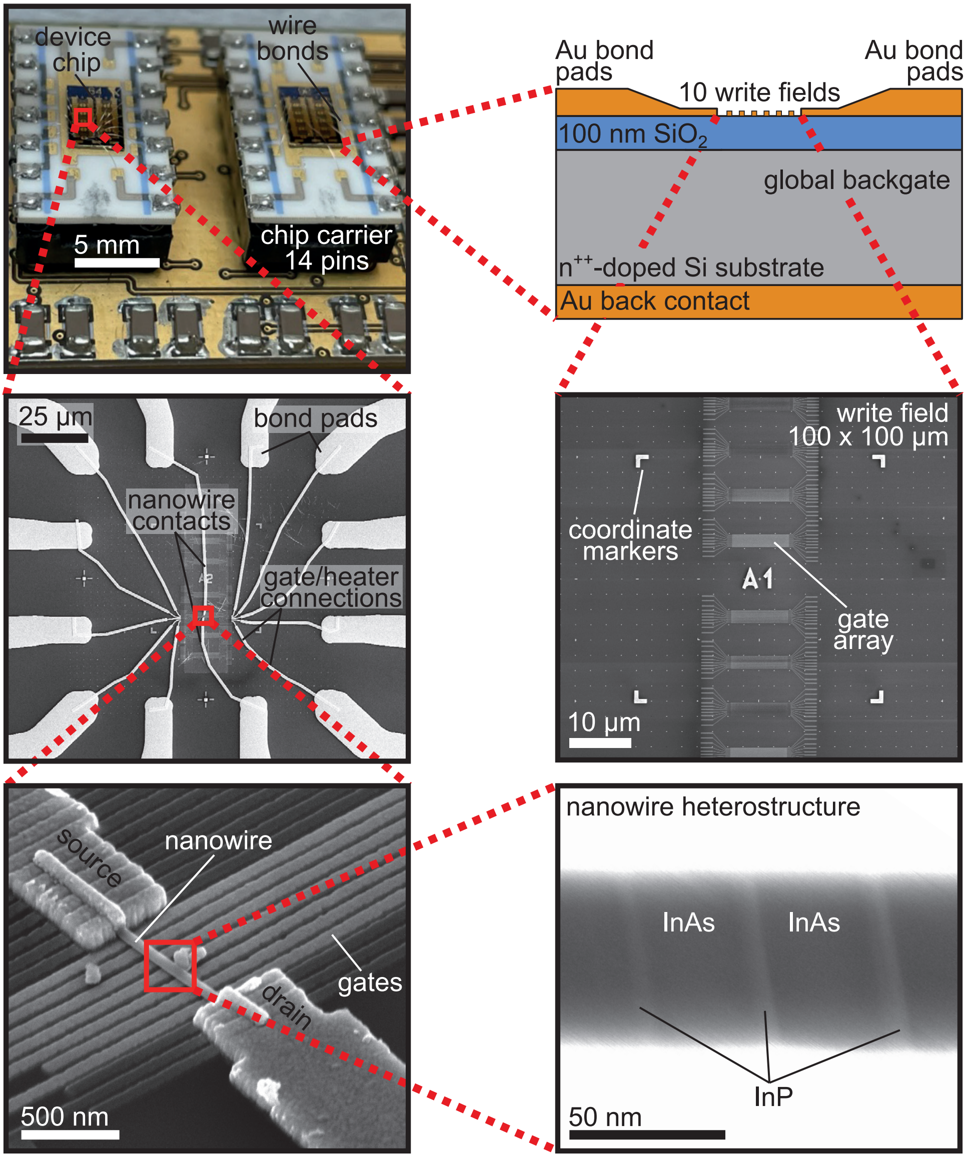

Figure 14: Device layout and dimensions. Schematic illustration of device dimensions with relevant components labelled. Panels on the left side are based on a real device. Panels on the right side are for illustrative purposes only and come from different devices.

locally introduce heat.

The basic dimensions and layout of the devices discussed in this work are introduced in fig. 14. Devices are fabricated on a silicon-based device chip, which is glued and wire bonded to a 14-pin chip carrier. This chip carrier is compatible to various measurement setups, including the sample mount for an Oxford Instruments Triton 200 dilution refrigerator as shown in fig. 14. The device chip consists of a degenerately n-doped silicon substrate, which together with a gold back contact serves as a global backgate to all individual nanowire devices on the chip. A thermally oxidized 100 nm thick SiO_2 layer electrically insulates the backgate from the nanowire device circuits. On the surface, the device chip contains ten $100\,\mu\mathrm{m} \times 100\,\mu\mathrm{m}$ write fields, each surrounded by 12 gold contacts leading to bond pads. The write fields contain coordinate markers used to identify and connect nanowires located therein to the bond pads. Within each write field individual devices are located: A III-V semiconductor nanowire, hosting the QD system, is contacted by a source and drain electrode and surrounded by gate- and optionally heater structures designed to explore specific research questions. The smallest dimension to be considered for devices is finally the material structure of the nanowire itself.

Nanowires are defined as high aspect ratio structures with two dimensions (in the following referred to as diameter) on the nanometer scale and lengths of up to tens of micrometers. For diameters sufficiently small to introduce quantum confinement, these structures act as one-dimensional conductors and thus bring ideal properties for the relative simple realization of QD systems. Two viable approaches exist for the fabrication of semiconductor nanowires: In a top-down approach, a larger block of semiconductor material is etched to nanowire dimensions. This can result in surface defects and non-uniformity, which play an important role in nanoscale structures with a high surface-to-volume ratio [108]. Thus, the group III-V semiconductor nanowires discussed in this work are grown by controlled crystallization using epitaxy [108], a bottom-up approach, based on the vapour-liquid-solid (VLS) mechanism [109].

The VLS nanowire growth is seeded by liquid gold particles, deposited on a suitable substrate and introduced to a controlled precursor molecule atmosphere in either a chemical beam epitaxy or a metal organic vapour phase epitaxy reactor [110]. The gold particle then catalyses the decomposition of the precursor molecules in the gas phase, absorbs the elements and ultimately forms a supersaturated liquid alloy [111]. Then, atoms are expelled from the seed particle and nanowire growth is initiated and maintained [110, 111]. Advantages of epitaxial nanowire growth are, aside from the high crystalline quality, access to both wurzite (WZ) and zinc-blende (ZB) crystal structures for many III-V materials [108], enabling the formation of homostructures, as well as the ability to combine lattice mismatched materials to form both radial and axial heterostructures, which may not be available in planar structures [99, 112]. The nanowires discussed in this work were grown by collaborating material scientists in Lund and in Pisa. The following sections introduce the necessary considerations and techniques for the design and fabrication of nanowire quantum dot devices.

5 Device design considerations

In this work, three main components are considered for the device layout: (1) The implementation of the QD system itself, (2) the gate structure and (3) an optional heater structure, for which trade-offs between flexibility, the available degree of control over experimental parameters and simplicity are discussed in detail in the following. Because the gate and heater structure need to be designed around the QD's requirements, the specific QD system implementation is considered first. The quasi one-dimensional nature of the nanowires (in this work: diameters between $35\,\mathrm{nm}$ and $50\,\mathrm{nm}$) only requires the introduction of additional confinement of the free electron motion along the axial direction of the nanowire via tunnel barriers in order to form a serial QD system [99]. Tunnel barriers are formed by means of epitaxially defined heterostructures, electrostatic gating or by Schottky-barriers at the contact metal-semiconductor nanowire interface for certain materials. Single QD devices based on these concepts are shown in fig. 15.

Epitaxial tunnel barriers (for the nanowires used in this thesis) are defined by heterostructures in the form of thin InP segments grown into otherwise InAs nanowires. Because of an approximately $600\,\mathrm{meV}$ conduction band offset between InAs and InP [112] sufficiently thin InP segments act as tunnel barriers within the nanowire. The combination of two closely spaced InP segments then results in a QD forming in the enclosed InAs segment — an elegant approach developed in 2002 [112]. The high quality, sharp material transitions in the heterostructures give well defined, box-shaped potential barriers, which can be grown in a highly symmetric manner, thus coupling the QD to the source and drain leads with a near ideal symmetry [113, 114]. Further, the barrier thickness is controllable with single digit nanometre precision and close axial placement is possible to introduce strong quantum confinement along the axial direction in the enclosed InAs segment. An exemplary device is shown in fig. 15(a) and illustrates the simplicity of epitaxially defined QD devices: Because the QD implementation is completely integrated in the nanowire the only additional required device components to define and control a SET are electrical (ohmic) contacts to either side of the InP barrier structure as well as a global backgate. This simplicity however comes at cost of control over the tunnel couplings. Barrier height and width are widely fixed and limited direct control over tunnel couplings can only be achieved by complex reordering of QD orbitals [115] or indirectly by operating the device at higher QD occupations, effectively reducing the barrier height [84, 85].

Electrostatically defined QDs in nanowires, on the other hand, enable simple and direct control over the barrier height and thus also the relevant tunnel couplings. An exemplary single QD device is shown in fig. 15(b). For the electrostatic definition of QDs, barriers are formed in homogeneous nanowires by means of local barrier gate electrodes, capacitively coupled to the nanowire and biased such that electrons (or holes for p-type devices) are repelled in the direct vicinity of the barrier gate electrode (labelled BL and BR in fig. 15(b)).

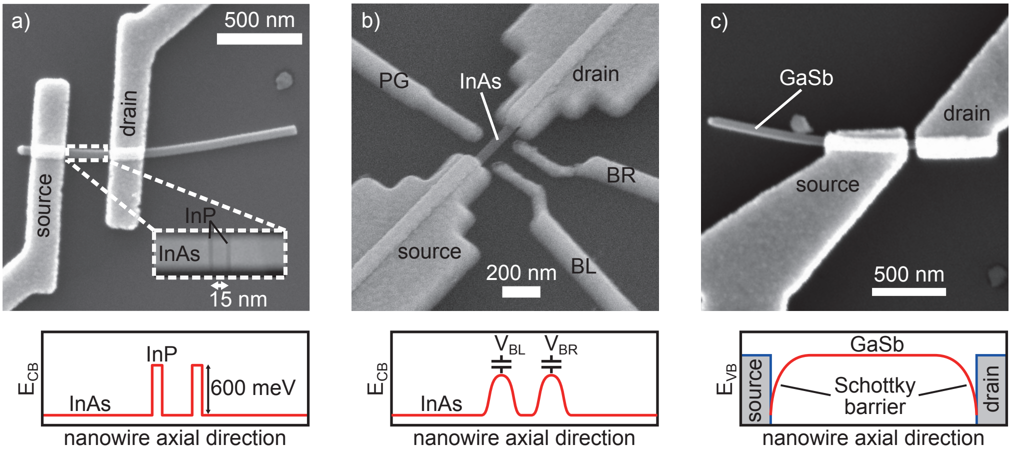

Figure 15: **Illustration of different QD implementations.** (a) Epitaxially defined QD in a InAs/InP heterostructure nanowire. (b) Electrostatically defined QD in an InAs nanowire. (c) Schottky-barrier defined QD in a p-type GaSb nanowire.

The coupling between the QD and its leads is then controllable directly by variation of the barrier gate voltage without the necessity of changing the QD occupancy [86]. Further, the QD can, depending on the gate placement, be arbitrarily positioned along the nanowire axis [86, 116]. Capacitive control over the electro-chemical potentials of the QD in such systems requires a local gate electrode, referred to as plunger gate (labelled PG in fig. 15(b)) as use of a global backgate would interfere with the barrier gates and hinder the possibility to precisely control tunnel couplings. In direct comparison to epitaxially defined QDs, electrostatically defined potential barriers are less sharp and the axial QD dimension are often larger and limited by the resolution of the gate-defining lithography process. The QD dimensions, however, directly relate to the single-particle energy scale and thus quantum effects may become harder to resolve in experiments for larger QDs.

Schottky barriers, which may form at the interface between the certain metallic contacts to the semiconductor nanowire are employed as a third method to define QDs for experiments presented in this thesis. If Schottky contacts are placed at a sufficiently narrow distance, the enclosed, electrically insulated nanowire segment forms QD states. Given the right interplay between the barrier height and width, the electron temperature in the system as well as the QD occupation, the QD can be tunnel coupled to the metallic contacts with an adequate coupling strength to resolve currents in experiments. This method exerts the least amount of control over the barrier and QD parameters and comes with significant constraints on the device design as is discussed in detail in paper I and further detailed in section 7. For the GaSb nanowires characterized as part of the experimental work discussed in the next chapter, Schottky barriers are prominently present in low temperature transport experiments. Thus employing Schottky barriers to define QD systems is the default for GaSb nanowire devices [117]. A simple single hole transistor (SHT), which makes use of the global backgate and a Schottky-defined QD in a GaSb nanowire is shown in fig. 15(c).

Equally important to the design of single QDs is the definition of more than one QD in series, for instance to obtain a DQD, which remains in principle possible with all three approaches. While for electrostatically defined barriers, the implementation of multiple QDs is straight forward and only requires additional plunger- and barrier gates, the device design becomes more complex for the remaining approaches. Where previously no gate structures were required in the write-fields, a global backgate alone no longer suffices to provide individual control over several QDs. In the case of Schottky-contact defined outer barriers, the separation of the enclosed nanowire segment into two (or more) QDs necessitates the introduction of both, an electrostatic barrier via a barrier gate as well as separate plunger gates for the individual QD nanowire segments. Thus, careful consideration of the contact-to-contact distance and choice of gate architecture is required for the QD segments to remain short, placing strict constraints on the device design. For epitaxially defined serial QD systems in InAs nanowires, in principle additional InP segments can directly be introduced during nanowire growth. Individual gating of the resulting epitaxial QDs, which entails gate electrodes aligned with each QD, is challenging: Thin InP barriers are not visible in regular scanning-electron micrographs and precise gate alignment with the QDs is not trivial. The problem is solvable for example by the use of epitaxial markers to visualize the barrier locations, for instance by selective shell growth [85], but introduces more complexity to both the nanowire growth and the device fabrication process. An alternative solution is the placement of various gate electrodes in the vicinity of the estimated location of the serial QD system in the nanowire. While the latter approach remains easy to handle from a device processing point of view, device characterization requires the identification of selected gates which couple sufficiently different to each QD for individual capacitive control. Thus, often significant cross coupling between gates and QDs is introduced due to misalignment and success can vary from device to device.

The previous considerations highlight that a global backgate alone does not provide a desirable degree of control over nanowire-based QD devices outside the most simple single QD geometries. Consequently, more advanced localized gating approaches which fulfill the requirements for different QD implementations and with the capability of addressing individual nanowire segments separately are needed. Aside from intuitive side-gates, local gating of nanowires is possible by bottom- [86], top- [116], and wrap-gate [118–120] electrodes. The latter two approaches involve the deposition of an insulating gate-oxide layer on the nanowire surface, which may change the opto-electronic behavior of the system. In this thesis, side- and bottom-gate structures are used and exemplary devices are shown in fig. 16(a) and (b), respectively.

Local side-gates are either distributed asymmetrically (see fig. 15(b)) or symmetrically around the nanowire to increase the capacitive coupling to the nanowire (see fig. 16(a)). Both approaches remain simple from a device-fabrication point of view as the gates can be designed

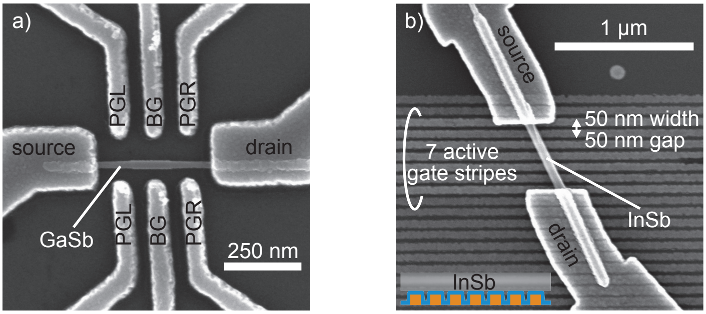

Figure 16: Illustration of side- and bottom-gates. a) Symmetrically side-gated, Schottky-contacted GaSb nanowire. The outer gates act as plunger gates (PGL, PGR), the middle gates as barrier-gates (BG). b) Bottom-gated InSb nanowire with 7 active gates. Inset: Device cross-section.

and deposited around a nanowire located at an arbitrary location within the write-fields. This gating approach, however, comes at considerable drawbacks: First, the capacitive coupling to the nanowire remains relatively small and gate electrodes need a sufficient metal thickness, in turn limiting the resolution of the lithographic gate definition and the ability to shrink the gate dimensions. Second, owed to the open design in vicinity of the nanowire, cross-talk between even distant gates is not well screened leading to cross-coupling between different gates and QDs.

Bottom-gated devices, fig. 16(b), are more complex to fabricate. First, gate arrays are defined in the write-fields and covered by an 8 nm HfO_2 gate oxide layer. Next, nanowires must be deposited atop the gate arrays in an intricate alignment process. Finally, the nanowire and a selection of the gates are electrically contacted and connected to the bond pads on the device chip. The reward for the fabricational complexity arrives in the form of various advantages compared to a side-gate design: The capacitive coupling is found to be increased by up to ten-fold, the gate electrodes can be more densely packed as a consequence of the reduced metal thickness (around 10 nm Ti/Au) and non-neighbouring gates are efficiently screened by the in-between gate stripes. The latter significantly reduces cross-coupling effects in measurements on serial QD systems.

An additional device component, which is necessary to conduct thermally biased experiments on QD systems, is a local heating element. For the specific experiments discussed in papers II and III, it is essential that the heating element can (1) introduce a temperature difference between the electron reservoirs coupled to the QD system and (2) introduce a temperature difference such that the phonon temperature at the precise location of a DQD, in the following referred to as the phonon reservoir, is elevated compared to the electronic temperature of the contact electron reservoirs. Thermal biasing of QD devices brings several requirements for a heating technique to be viable as detailed in refs. [121, 122]. First, the heater design must be compatible to the gate architecture and biasing of, as well as current measurements through, the QD system. Second, in order for QD features to re-

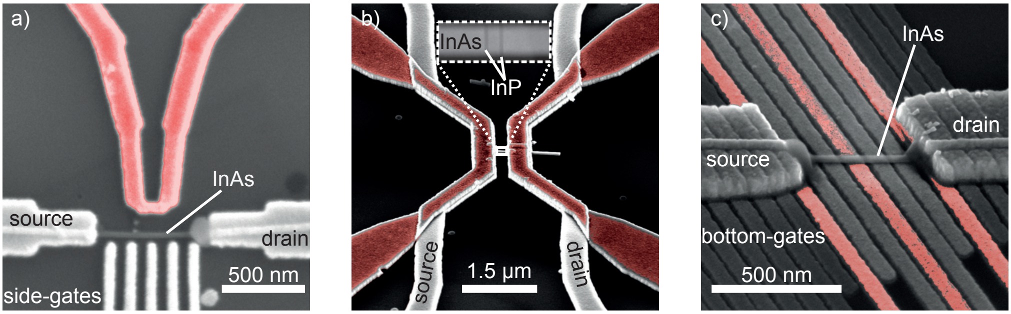

Figure 17: Illustration of different heater designs. a) Side heaters. b) Top heaters. c) Bottom-heaters. The heater electrodes are false-colored.

main resolvable in electrical measurements, the heat supply should operate at sufficiently small heating powers to maintain low average electron temperatures in the QD's electronic circuit. Finally, the heat should be applied in a highly local manner such that unheated reservoirs remain close to the cryostat base temperature and the temperature difference to the heated reservoir is maximized. A comparison of common heater designs is found in ref. [121].

Conceptually, two different heating techniques can be distinguished: Heat can be supplied directly to the QD's electronic circuit by an internal heating mechanism or externally, decoupled from the QD's electronic circuit via a nearby Joule-heater electrode. Internal heating is achieved by running a current through one of the device contacts, which in turn heats the electrons in the reservoir via electron-electron interactions [123, 124]. While this method is particularly suitable for low temperature experiments because it only requires minimal heating powers [121], it interferes with voltage biasing of the device [123] and is not designed to raise the temperature of the phonon reservoir above that of the electronic reservoirs.

Consequently, for the work presented here only external heating concepts were viable, which are based on currents flowing through Joule-heater electrodes. These Joule-heaters deposit most of the applied heating power at the point of highest resistance, controlled by defining the narrow-most electrode segment and are traditionally designed in a side-heater [125] geometry, shown in fig. 17(a). By alignment of a side-heater electrode with a DQD, paper II demonstrates that it is possible to heat the phonon bath in the vicinity of the DQD more than the electron reservoirs. Side-heaters, however, act rather globally, introduce significant heating to the substrate, thus requiring larger heating powers [121] and the presence of a large heater electrode can interfere with local gating [126]. A more local version of external heating with a top-heater design was introduced by Gluschke et al. in 2014 [121], where the heater electrodes are directly placed on top of the nanowire contacts, electrically insulated by an oxide layer. This approach has been demonstrated to offer ideal conditions for the localized heating of contact electron reservoirs and thus the thermal biasing of single QD devices [77, 121]. In contrast to a side-heater geometry this design again cannot fulfill the need to supply heat mainly to the phonon bath. An exemplary, top-heated device is shown in fig. 17(b).

In paper III an alternative heater design is introduced, where the heating element is directly integrated with a bottom-gate design: Selected gate stripes are connected on both ends and thus can be operated as local Joule-heaters. By applying the heating bias, used to drive the current through the gate stripe symmetrically around the gate potential required for the gating of the nanowire, both gating and heating remain simultaneously possible. This merged bottom heater and gate design combines the advantages of top-heater designs with the ability to introduce highly localized heat at near arbitrary locations of the QD system or below the metallic contacts to reproduce the top-heater functionality. Furthermore, if the QD system is electrostatically defined, the heat sources are naturally perfectly aligned with the QDs. An exemplary bottom-heated device is shown in fig. 17(c) and further details are discussed in section 9.

6 Principles of nanowire device processing

The fabrication process for devices in this work follow a simple scheme: Nanowires are either randomly dry-distributed within the write fields of an empty device chip or aligned with pre-defined bottom-gate arrays using a micromanipulator. The coordinate markers in each write field, see fig. 14, are then used to identify the exact position of suitable nanowires and the contact, gate and possible heater architecture are designed and transferred onto the write-field. The fabrication steps can essentially be broken down to a modular, layer-by-layer fabrication scheme which is illustrated in fig. 18. Each modular layer consists of an electron-beam lithography (EBL) defined metallic pattern, electrically insulated by a dielectric from structures belonging to different layers. Details of the process parameters and flow required to reproduce the above discussed gate and heater structures are given in the appendix and for a detailed description of the different nanofabrication techniques readers are referred to ref. [127].

The basic process to define a layer, consisting of metallic structures within the write fields, is simple: The device chip is spin coated with a positive, electron-beam (e-beam) sensitive resist. The pattern, intended for transfer onto the write-field is then exposed to an electron beam, which causes a change in the chemical structure of the resist, increasing its solubility by a developer chemical as compared to the non-exposed resist. During the subsequent resist development, the e-beam exposed resist areas are removed, uncovering the device chip's surface. Next, thermal metal evaporation is used to metallize the sample surface and by following with a lift-off process, removing the resist and metal deposited thereon, metal

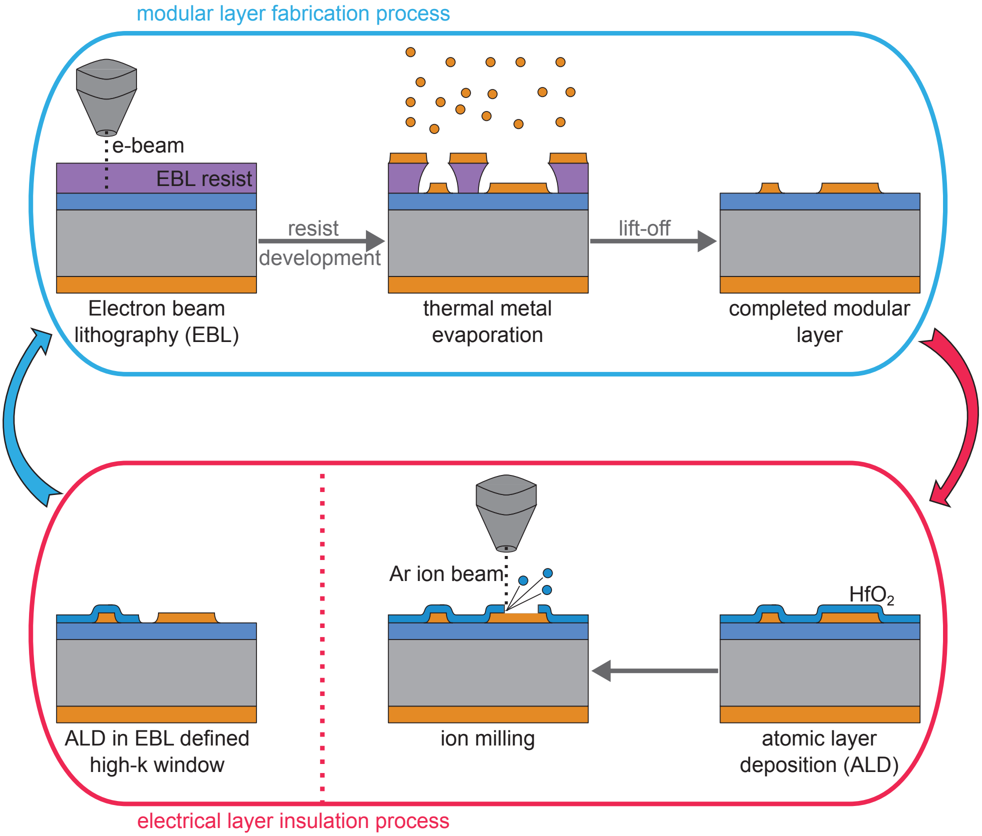

Figure 18: Schematic illustration of the modular device fabrication scheme. Modular layers are fabricated using a combination of electron beam lithography (EBL), thermal metal evaporation and a lift-off process, see top panel. Modular layers are separated by an insulating oxide layer deposited via atomic layer deposition (ALD). To connect to lower layers, the insulating oxide can either only be deposited in an EBL defined window or ion milled at selected locations.

remains only in the EBL defined patterns.

For device architectures requiring an additional layer, for instance top heaters or the nanowire device circuit defined atop of bottom-gate arrays, electrical insulation is necessary. This is achieved by depositing a dielectric HfO_2 oxide layer using atomic layer deposition (ALD), a process during which the sample surface is exposed to sequential flow of precursor gases, initiating a molecular layer-by-layer oxide growth. The deposition of an oxide layer covering the complete device chip surface, however, prevents the subsequently fabricated metallic structures to be electrically connected to patterns in a lower layer, which is important to connect to bond pads. Consequently, openings in the insulation layer are needed. In this work, two different approaches are used to define openings as illustrated in fig. 18: (1) After continuous ALD oxide coverage of the device chip surface, select areas are exposed to a focused argon ion beam, milling through the HfO_2 layer. With the correct dose, the argon milling process enables the opening of windows in the dielectric layer without milling the underlying metal. (2) Alternatively, the HfO_2 layer can be deposited only in select areas. Therefore, first an EBL step defines a so called high-k window and with a subsequent ALD process combined with resist lift-off the dielectric remains only in the desired area on the chip surface.

Repetition of the modular layer fabrication and electrical layer insulation process, as outlined above, allows the definition of arbitrary metallic, stacked structures within the device chip's write fields, including the electrical contacts to individual nanowires. Before nanowire contacts can be metallized, however, an additional crucial fabrication step is required. After removal from the growth reactor, semiconductor nanowires oxidize and form a surface native oxide layer, which prevents electrical contact to the semiconductor material. Thus, the native oxide must be removed before contact metallization. In this work, InAs and GaSb nanowires are contacted and their respective oxide etching procedures differ drastically. For InAs nanowires ohmic contacts can reliable be formed by a chemical self-terminating surface etch and passivation process based on ammonium polysulfide water solutions [128].

The oxide removal process for GaSb nanowires is less developed. Here, one challenge is the material's sensitivity to water exposure [129], as illustrated in fig. 19(a) and (b): A 10-minute dip in water suffices for the near complete decomposition of the nanowire's GaSb segment, while the Au seed and the InAs stem remain visibly unaffected. Consequently, many common chemical etchants, which are dissolved in water, result in damage to the GaSb nanowire surface and poor electrical contact. Instead, alcohol diluted etchants are applicable and hydrogen chloride in 2-propanol has been demonstrated to offer digital etch properties for GaSb nanowires [129, 130].

In this work, a dip in a 1.25 M hydrogen chloride – 2-propanol solution followed by a 2-propanol rinse is used directly prior to the contact metallization for the oxide removal. Fig. 19(c) and (d) show contacted, nominally undoped nanowires after a 90 and 60 second etch, respectively. The scanning electron micrographs indicate that for too long etch times, visible thinning of exposed nanowire segments occurs, deviating from a digital etch regime. Because the contact resistance is found to decrease with increasing etch times, a 60 second etching step is considered ideal for nominally undoped nanowires. It should be noted that although alcohol-based etchants significantly enhance the contact quality compared to aqueous solutions, the ideal process time can vary for the individual nanowires, possibly dependent on the diameter or dopant concentration as well as the contact spacing, and thus over-etching cannot always be avoided. For the zinc-doped GaSb nanowires used in paper I an optimized oxide etch time of 35 s is found.

As a result of the expected Fermi-level pinning in the valence band for p-type GaSb, all metals are expected to result in ohmic contact, which has been demonstrated for Ni/Au, Pt/Au, Ti/Au and Pd/Au biliayers on bulk GaSb [131]. For nanowires, the lowest contact

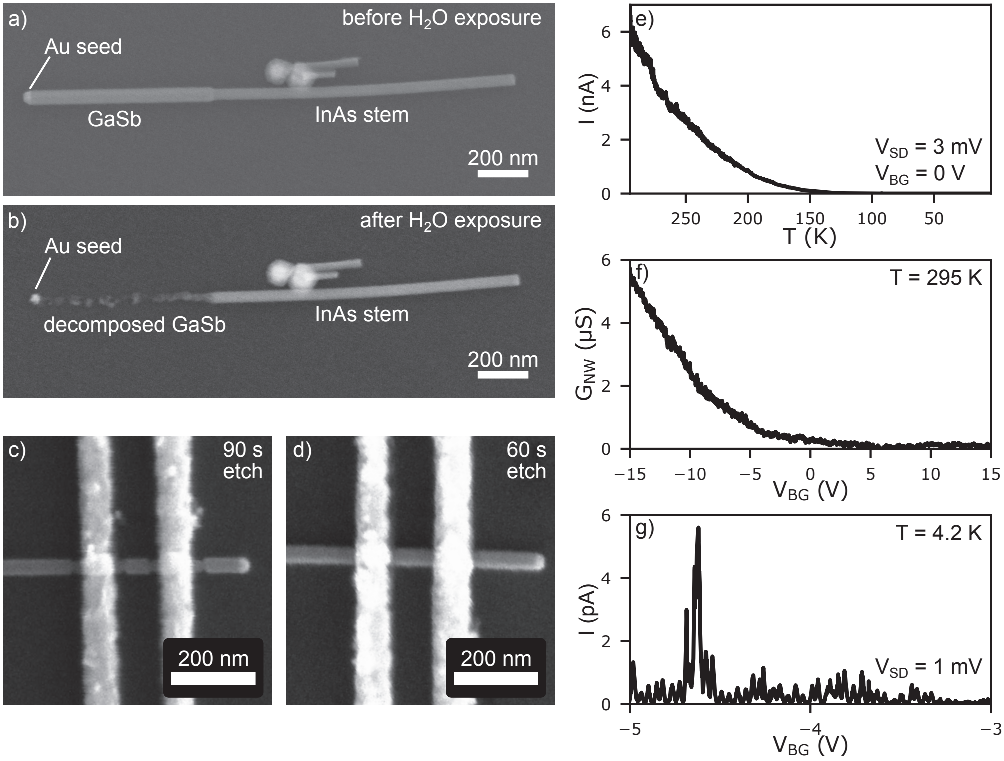

Figure 19: GaSb native oxide removal. (a/b) Undoped GaSb nanowire before (a) and after (b) a 10 minute H_2O dip. (c/d) Contacted, nominally undoped GaSb nanowire after a (c) 90 s and (d) 60 s HCl:IPA etch. (e) Temperature dependent two-probe current, (f) room temperature nanowire conductance and (g) low-temperature Coulomb oscillations measured on backgated GaSb nanowire devices.

resistances are found for Pd contacts [132], which however degrade rapidly over time. Thus, in this work, Ni/Au contacts are used. At room temperature, the outlined contact method results in ohmic behaviour. Backgated devices can thus be operated as field-effect transistors, which is shown by demonstrating the gate-dependent conductance in fig. 19(f) for a GaSb nanowire. As the temperature is decreased, see fig. 19(e), devices appear to freeze out around 130 K. Currents are still detected down to millikelvin temperatures in a sufficiently negative gate regime, but as a function of the backgate voltage V_{BG} now exhibit distinct Coulomb oscillations if contacts are closely spaced. The device is thus operated as a single hole transistor. The observation of Coulomb oscillations, plotted in fig. 19(g) at 4.2 K, is characteristic for QD formation and indicates the presence of barriers at the contacts. Considering that for over-etched nanowires residual oxide layers are unlikely, these barriers are attributed to Schottky contacts, which could not be avoided in the experiments presented here.

Further optimization of the etching process could be beneficial. Here, near ph-neutral aqueous buffer oxide etcher (BOE) [130] and in-situ N2 plasma cleaning [133] or argon milling as is commonly applied to contact InSb nanowires [134] are promising alternatives.

Towards p-type GaSb spin-orbit qubits

Serial double quantum dots have, since the late 1990s, been in the extensive focus of experimental efforts to realize semiconductor-based solid state quantum bits or qubits, the fundamental building block of a quantum computer. In contrast to classical computers, which operate on information stored in classical states and represented by binary digits (bits), a quantum computer operates on quantum information. A bit defines the smallest unit of information and can take a value of 0 or 1 [135]. This information is physically encoded through a network of transistors and the 0 and 1 states are defined by the output current or voltage of each physical bit. During a computation process, the value of each bit can be individually changed by logical operations. Consequently, at any given point in time n bits can be described by a list of n numbers, each either 0 or 1 [135].

A qubit on the other hand is physically implemented in form of a quantum mechanical two-level system (TLS) with clearly distinguishable states $|0\rangle$ and $|1\rangle$. The advantage of a TLS is rooted in the possibility to form superposition states $a\,|0\rangle + b\,|1\rangle$, where the amplitudes a and b directly relate to the probability of finding the TLS in the state $|0\rangle$ or $|1\rangle$. Although both the initialization and read-out of a qubit state is only possible in either the $|0\rangle$ or $|1\rangle$ state, thus resembling exactly the information stored in classical bits, logic operations can be performed on superposition states of entangled qubit systems. Consequently, during a computation step the description of n entangled qubits requires 2^{n} complex numbers — a concept enabling quantum parallelism [135] which allows quantum computers running clever algorithms to tackle selected problems that are out of reach for classical computers [136]. These principles of quantum computing pose stringent requirements for the physical implementation of qubits [135, 137]. First, the TLS have to be sufficiently decoupled from their environment to coherently remain in a well defined state for a period of time longer than the duration of logic operations. Second, qubits must be strongly coupled to one another to allow for entanglement and information transfer. Finally mechanisms for the controlled initialization, manipulation and read-out of the TLS states must be available [135].

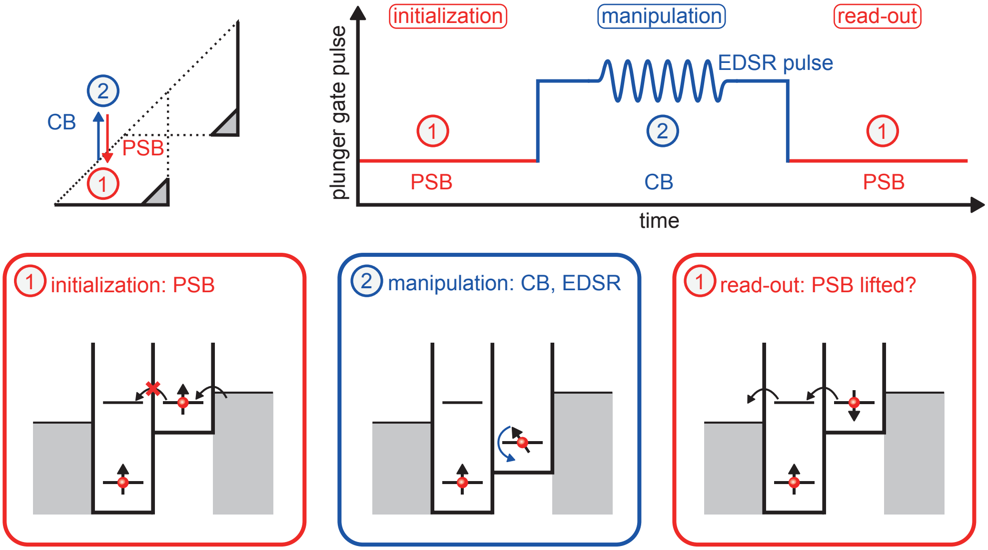

Figure 20: Schematic illustration of the operation cycle of a spin-orbit qubit.

This is where DQDs come in: Because a DQD enables precise, individual control and confinement of single charge carriers it is naturally possible to define and control various TLS implementations. One such TLS is defined by the two charge states of a DQD populated by a single charge carrier, $|L\rangle$ and $|R\rangle$, differing only in which QD is occupied [138]. These so-called charge qubits are controlled, initialized and read-out purely by elements (gates and charge sensor) capacitively coupled to the DQD [139] and are based on the principle of shifting the weight of the wavefunction of molecular states between the two QDs. A drawback of charge qubits, however, is their sensitivity to the DQDs charge environment, which can result in short coherence times.

A more robust implementation of a qubit was suggested by Loss and DiVincenzo in 1998 and uses the natural TLS defined by the spin state of a charge carrier confined to a QD [9]. Here, the spin up $|\uparrow\rangle$ and spin down $|\downarrow\rangle$ states define the so-called spin qubit and the first experimental spin state initialization and measurement was based on Zeeman-split levels in a single QD [140]. Today, DQDs are commonly employed for the implementation of spin qubit because PSB provides the tools to initialize or read-out spin state with relative ease and high fidelity [141, 142] and spin qubits exist in various closely related forms (single spins, singlet-triplet, spin-orbit, g-tensor modulation and exchange-only qubits) [143].

Figure 20 illustrates the operation cycle of a spin-orbit qubit based on a DQD with a spin-up electron permanently trapped in the left QD [144]. A constant magnetic field is applied to the system to lift spin-degeneracy. To prepare a $|\uparrow\rangle$ state in the right QD, the DQD is idled in a PSB regime to initialize a parallel spin configuration between the two electrons on the DQD [145]. Conversely, if in the same level configuration a transition from the right to the left QD is observed, this indicates a $|\downarrow\rangle$ state of the qubit and thus PSB enables high fidelity qubit initialization and read-out.

For the manipulation of the spin state, the DQD is tuned into a Coulomb blockade (CB) regime to confine the electron to be manipulated in the right QD. A controlled rotation of the qubit state within the Bloch sphere is then commonly induced either by application of an ac magnetic field via electron spin resonance (ESR) [146] or by an ac electric field via electric dipole spin resonance (EDSR) [147, 148], which act on the spin. ESR requires relatively large power which dissipates, possibly resulting in heating effects, and acts on large scales compared to typical device dimensions. Addressing individual qubits with ESR is thus challenging. EDSR on the other hand uses ac electric excitations which can directly be supplied by a gate in a low-power and localized manner (see fig. 20), but requires a strong link between the electron's spin and momentum [145]. A link between the spin and momentum of a charge carrier is naturally present in systems with strong spin-orbit coupling [148] or can be artificially induced by micromagnets introducing a local magnetic field gradient across the DQD [149]. In such systems, an EDSR pulse results in a periodic displacement of the electron's wave function [144] which in turn results in a controlled spin rotation if the frequency matches the Larmor frequency [145].

The above outlined principle-of-operation of a spin-orbit qubit defines ideal properties for the qubit's host material: large g factors lift spin degeneracies at small magnetic fields and in combination with strong intrinsic spin-orbit interactions enable fast spin manipulation and high Rabi frequencies [143]. Another stringent requirement relates to the time scale on which the spin orientation is maintained, which has to significantly exceed the time needed for spin manipulation during logic operations [10]. The fidelity of spin-based qubits is reduced by spin relaxation or dephasing processes, leading to a loss of control over the qubit. Notable mechanisms reducing the spin coherence times are electrostatic charge fluctuations or coupling to nuclear spins in the qubit's environment [138, 143]. Strong spin-orbit interactions couple the spin to it's charge environment and in combination with electrostatic fluctuations or phonon-mediated processes result in an EDSR-like process and spin dephasing or relaxation [143, 145, 150]. Consequently, spin-orbit coupling introduces a trade-off between fast control and the fidelity of spin-orbit qubits.

Nuclear spins in the DQD's host material interact with the spin of charge carriers confined to the DQD via hyperfine interactions, which in turn leads to spin dephasing [151]. This dephasing process can be tackled by using isotopically pure group IV semiconductors to minimize the number of nuclei with non-zero spin [138, 143]. Another approach to reduce the hyperfine interaction mediated dephasing makes use of hole- instead of electron spins in p-type DQD devices. Hole spins, due to the predominantly p-orbital Bloch wavefunctions in the valence band, experience vanishing contact hyperfine interaction [152], promising improved qubit fidelity. This concept has in recent years sparked interest in p-type QD systems and led to various qubit demonstrations. Here, encouraging results have been achieved in the Si and Ge material systems, which further benefit from an enhanced spin-orbit interaction for holes as compared to electrons [101]. For a detailed introduction and summary of recent work the interested reader is referred to the reviews in refs. [101, 138, 143].

III-V semiconductor nanowires are another interesting material platform for DQDs and spin-orbit qubits have been successfully demonstrated in n-type InAs [145] and InSb [153]. These qubit implementations benefit from large *g* factors [154, 155] and spin-orbit coupling [156, 157], which enable rapid spin control [10]. In zinc blend InAs and InSb nanowires, Campos et al. [158] suggest that the application of an external electric field can enhance the spin-orbit coupling significantly and further impacts the orientation of the spin-orbit field. Although only a fraction of an external electric field is expected to transmit into nanowires [159], indications of a link between the orientation of the spin-orbit field and gate-induced electric fields have been reported [157, 160, 161]. Enhancement-mode nanowires allow for electric fields to be engineered because plunger- and barrier gates require opposite voltage polarities and for nanowires clever, three-dimensional gate architectures are possible. This combination could provide a path for all-electrical manipulation of the spin-orbit field in III-V semiconductor nanowires [160]. Such devices have the potential for faster spin control and higher qubit fidelities, achieved by alignment of the spin-orbit field with an external magnetic field [145, 161].

While based on the III-V semiconductor material platform, n-type QD systems are today commonly studied in literature, significantly less effort is devoted to p-type devices. To date, the only reported p-type III-V nanowire spin qubit is realized in ambipolar InSb [162]. Another interesting and naturally p-type III-V nanowire material is GaSb. On paper, GaSb has the highest hole mobilities in the III-V family [163] and high hole mobilities up to $1028\,\mathrm{cm^2V^{-1}s^{-1}}$ have been indeed been reported in ref. [164]. At low temperatures, ohmic contacts to GaSb have, however, only been achieved to planar GaSb quantum wells [165]. The realization of GaSb nanowire QD systems in nanowires thus proves to be experimentally challenging. To date, QDs in GaSb nanowires have only been realized via closely spaced Schottky contacts [117] or by providing electrical contact through in InAs shell [166] making use of a broken bandgap alignment in GaSb/InAs core-shell nanowires [167].

7 Summary: Paper I

Here, the study presented in paper I comes in and aims to overcome the challenges associated with the design of high quality QD devices in Schottky-contacted GaSb nanowires. We employ bottom-gates, a common gate architecture for the electrostatic definition of QDs in nanowires, and probe the formation of single- and serial multi-QD systems in enhancement mode GaSb:Zn nanowires. We further study the magneto-transport properties of a single QD and extract *g* factors as well as spin-orbit energies. The results of paper 1 are summarized in figs. 21 and 22.

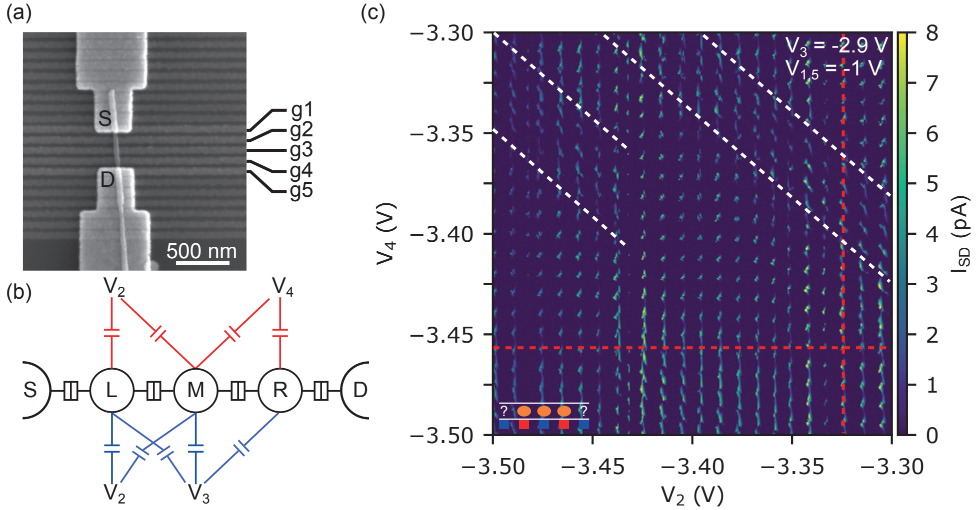

Figure 21: Gate control of GaSb nanowires. a) Scanning electron micrograph of a Schottky-contacted GaSb nanowire atop 5 underlying bottom-gate stripes g1-5 (device A). b) Measurement configuration for panel (c) (red) as well as a test configuration (blue) to probe a QD formed atop g3. c) Charge stability diagram in the red measurement configuration in (b) at $V_{SD} = 1\,\mathrm{mV}$ and $V_{BG} = -10\,\mathrm{V}$. Adapted from paper 1.

Figure 21 demonstrates a key challenge, which we identify, for the electrostatic definition of multi-QD systems in GaSb nanowires: Gates act on the nanowire only in their direct vicinity and can induce conductive islands, while gaps in gate arrays result in the uncontrolled formation of barriers in the axial nanowire direction. This can be seen based on device A, shown in fig. 21(a), which consists of five gate stripes, g1-5 underneath a Schottky contacted GaSb:Zn nanowire. By design, g1 and g5 are placed beneath the source and drain contacts to control the tunnel coupling through the Schottky barriers. G3 is intended as barrier gate to split the Schottky-defined GaSb segment into two separate, a left (L) and a right (R) QD for which g2 and g4 serve as plunger gates.

In practise, we find that in any gate configuration where currents can be detected, see fig. 21(c), triple QD features are present [103] and no control over the interdot coupling regime is achievable in what should be a standard DQD configuration. This behaviour indicates that in order to obtain a detectable current across the QD system, the voltage applied to g3 has to be set sufficiently negative to form a third (M) QD. We find additional evidence by testing different measurement configurations, outlined in fig. 21(b) and further show that g1 and g5 can induce additional QDs underneath the metallic nanowire contacts. We believe the suppressed gate control to be the result of a combination of the low mean free paths for holes (see supplemental material, paper I) in our nanowires and possibly surface trap states that may efficiently screen the nanowire's core from the gate potential.

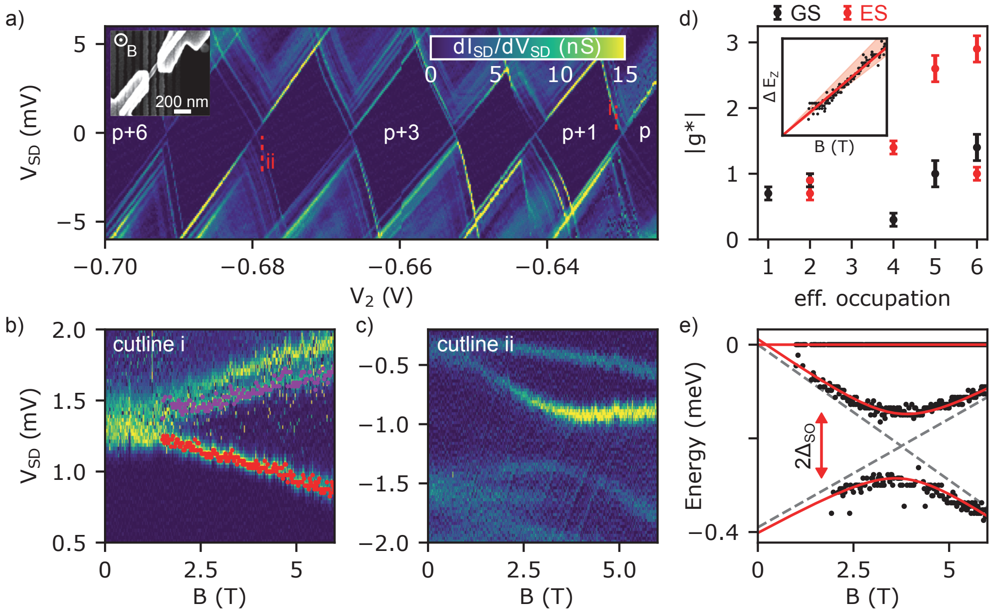

Figure 22: g factors and spin-orbit energy in GaSb QDs. a) QD charge stability diagram. Inset: Schottky contacted GaSb nanowire with one gate stripe enclosed by the contacts (device B). b) Ground state (GS) Zeeman splitting along cutline i. c) Zeeman splitting and avoided crossing along cutline ii. d) GS and excited state (ES) g-factors plotted against the effective occupancy p. Inset: Fit to the splitting extracted from (b). e) Fit to the states in (c). The differential conductance in (a-c) is limited for better visibility of all relevant features. Adapted from paper I.

Based on these findings we transition to a simplified device geometry (device B, see inset fig. 22(a)), which consists of only three gate-stripes underneath a Schottky-contacted GaSb:Zn nanowire. Again, g1 and g3 are placed underneath the contacts and a high positive voltage is applied to the backgate and $g1, 3$ which allows to form a clean single QD by application of a negative voltage to g2. The resulting charge stability diagram of the QD is shown in fig. 22(a). We then apply a magnetic field perpendicular to the sample plane and study the differential conductance along cutlines for different effective occupancies of the QD. We find Zeeman splitting (see fig. 22(b)) and in some cases identify avoided crossings as a result of spin-orbit coupling induced state mixing (see fig. 22(c)). This allows to extract g factors, which range from almost vanishing up to $|g^*| = 2.9 \pm 0.2$, see fig. 22(d), and a spin-orbit energy between $\Delta_{SO} = 70 \pm 10\,\mu\text{eV}$ and $\Delta_{SO} = 90 \pm 10\,\mu\text{eV}$ as illustrated in fig. 22(e).

8 Outlook: GaSb double quantum dot devices

The results of paper I pose the question *'How to build a working DQD device architecture based on GaSb and are p-type GaSb spin-orbit qubits a route worth pursuing?'*, which this outlook discusses.

One possible path towards the controlled definition of GaSb DQD devices is to study the impact of different surface treatments of GaSb nanowires on the low-temperature electrostatic gating behaviour. At room temperature, different surface treatments in combination with a successive oxide deposition have been used to enhance the properties of GaSb nanowire field-effect transistors [130]. A second approach is to adapt the gate design based on the findings in paper I. Here, the most simple adaption is shown in fig. 23(a) and makes use of what was a drawback in paper I: Gaps between neighbouring bottom-gate stripes act as barriers. A device design where only two gate stripes are enclosed by (and an additional two underneath) the Schottky contacts should then enable the formation of two conductive islands in the nanowire and thus a DQD. Although simple, this gate architecture yields no direct control over the interdot tunnel coupling while maintaining QD occupancies. To achieve complete control over barriers and QDs in GaSb nanowires, a gate architecture with the ability to obtain full segment-wise control over the nanowire is required. Here, stacking two shifted and electrically insulated layers of bottom-gates offers a promising solution. A prototype of this gate array was developed as part of the thesis work and a scanning electron micrograph is shown in fig. 23(b).

Figures 23(c) to (f) present the results of initial measurements on GaSb:Zn nanowires atop of the simple DQD gate architecture shown in fig. 23(a). To avoid the formation of conductive nanowire segments below the Schottky-contacts a positive voltage is applied to g1 and g4. Negative voltages are applied to the plunger gates, g2 and g3, to induce conductive QD islands to the nanowire. In contrast to the findings in paper I with a five-gate design, we are now able to tune the interdot tunnel coupling of the QD system by increasing the QD occupancies. This not only effectively reduces the barrier between the QDs but also, as a result of the more negative plunger gate voltages may expand the conductive regions within the nanowire, decreasing the barrier width. An exemplary charge stability diagram at the transition of the intermediate- to the strong interdot coupling regime is shown in fig. 23(c). When the plunger gate voltages are further increased (less negative), the charge stability diagram resembles the expectations for a weakly coupled DQD over a large range of occupancies, see fig. 23(d). In combination, this provides evidence for the formation of what is possibly the first pure DQD implementation in a GaSb nanowire.

Pauli spin blockade is an important tool for the initialization and readout of spin qubits in DQDs, and within the weak interdot coupling regime we find features that indicate the presence of PSB. One PSB blockaded charge state transition is shown in fig. 23 (e) and (f),

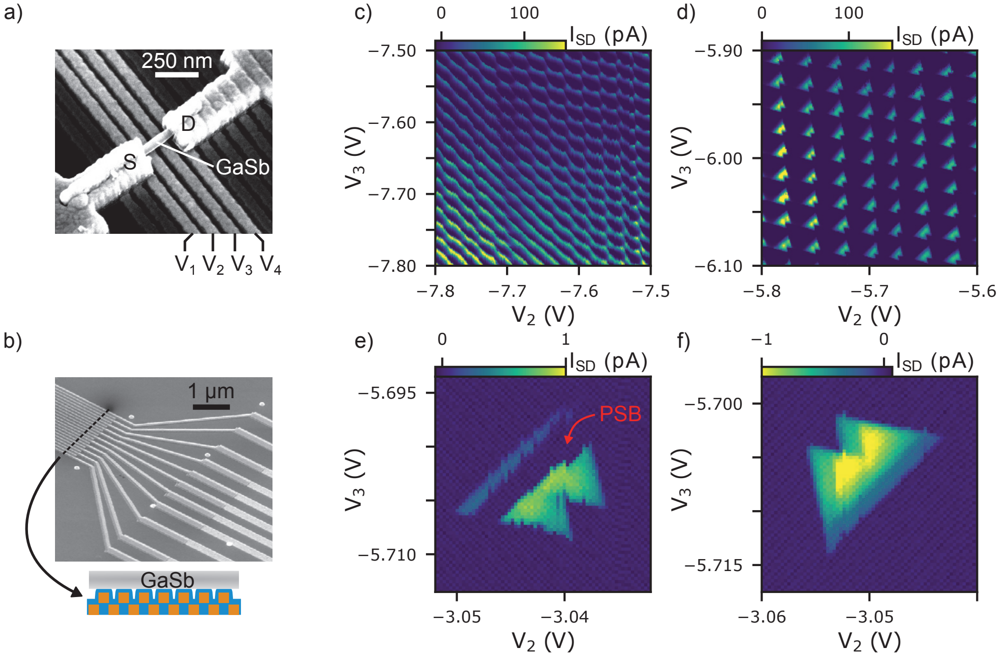

Figure 23: GaSb DQD devices. a) DQD device based on two bottom-gate stripes enclosed by Schottky contacts. b) Stacked bottom-gate design. c,d) Charge stability diagram with $V_{SD} = 2\,\mathrm{mV}$ at the transition between the intermediate and strong interdot coupling regime (c) and in the weak interdot coupling regime (d). The current is limited to $150\,\mathrm{pA}$. e,f) Finite bias triangles obtained at a charge state transition with Pauli spin blockade, measured at (e) $V_{SD} = 2\,\mathrm{mV}$ and (f) $V_{SD} = -2\,\mathrm{mV}$. The current is limited to $\pm 1\,\mathrm{pA}$. In (c-f) the barrier gates underneath the Schottky contacts are set to $V_1 = 1.4\,\mathrm{V}$ and $V_4 = 0.8\,\mathrm{V}$ and no voltage is applied to the backgate. To increase the measurement resolution, $V_{2,3}$ are fed through a $1 : 3$ voltage divider, which is not removed from the data.

where finite bias triangles are measured with a positive and negative bias. In the positive biased case in fig. 23(e) the current in the lower part of the finite bias triangles is clearly suppressed but becomes conductive if a negative bias is applied, see fig. 23(f).

It, however, remains to be noted that without access to the lowest DQD occupancies, the search for PSB equals the search for a needle in a haystack [168] and in GaSb remains a problem to be solved in future studies. Although, the example in fig. 23(e,f) features distinct currents along the finite bias triangle's baseline even in a PSB configuration, we find this feature to be significantly suppressed in other cases observed on our device. In a PSB configuration, spin blockade can be lifted for instance by hyperfine- [169] or spin-orbit interaction [170], which in turn introduce a finite current in the conventionally blockaded triangle regions, most notably for (close to) elastic transport along the triangle baseline. Consequently, the suppression of this current in GaSb devices may be a direct result of, and expected for, the reduced hyperfine interaction in p-type systems [11], but further complicates the search for spin blockaded features. Here, recent progress has been made by employing machine learning to identify PSB [168].

Finally, the author would like to comment on whether or not research on GaSb QD systems is a route worth pursuing. Given the fabrication-related challenges and so far the lack of a clear edge compared to other, already established qubit implementations, GaSb may not be the answer to the design of a future quantum computer. Here, for instance silicon-based p-type complementary metal-oxide-semiconductor technology based spin-qubit implementations seem highly promising. These CMOS qubits are built on industry-standard fabrication techniques [171], allow control over the spin-orbit interactions [172] and have recently been demonstrated to work at elevated temperatures of up to 5 K [142]. Consequently, the CMOS spin-qubit platform brings ideal preconditions for scalability, operation speed and qubit fidelity. Although, this may give a pessimistic outlook on the future of GaSb for qubits, the author still considers the exploration of novel material systems worthwhile and insightful. An interesting path forward would, however, likely entail to focus on the possibility of all-electrical gate control of the spin-orbit interaction with three-dimensional gate-architectures in III-V semiconductor nanowires.

Thermally driven transport in quantum dot systems

Thermoelectricity describes the conversion of temperature gradients within closed circuits to charge currents and vice versa. From an application point of view, the thermoelectric (TE) effect thus essentially enables active cooling or the generation of electrical power from heat by using the thermocurrent across a load resistor for instance to charge a battery. The allure of TE devices lies in the absence of macroscopic moving parts. Instead, such devices rely solely on charge and heat currents in TE materials — providing ideal conditions for low maintenance, lightweight and durable applications [173, 174]. For simplicity, in this chapter, only the concepts of energy harvesting, i.e. power generation are considered.

The underlying principle of the TE effect is that of energy filtering [175] and is illustrated in fig. 24 by considering a conductor coupled to two electron reservoirs at different temperatures in the absence of an external voltage bias. The thermocurrent I_{th}, for clarity in the remainder of this chapter defined as a current purely driven by heating effects, through this system can be described by the Landauer formula

$$\mathrm{I}_{\mathrm{th}} \propto \int \mathrm{T}(\mathrm{E})\,[f_{\mathrm{R}}(\mathrm{E}) - f_{\mathrm{L}}(\mathrm{E})]\,\mathrm{dE} \tag{40}$$

where $\mathrm{T}(\mathrm{E})$ is the conductor's transmission function [176]. Differences in the electron occupations between the reservoirs $f_{\mathrm{R}}(\mathrm{E}) - f_{\mathrm{L}}(\mathrm{E})$, in close analogy to the discussions in section 4 and as shown for a thermal bias in fig. 24, define a transport window within which currents can flow. For an energy-independent transmission function, however, the thermocurrent contributions of electrons travelling from the hot to the cold reservoir above- and from the cold to the hot reservoir below the electro-chemical potential of the reservoirs negate one another exactly and no net thermocurrent flows. Consequently, an energy-dependent transmission function with an asymmetry with respect to the Fermi-energy is a stringent requirement for the TE effect to occur and TE materials essentially act as an energy selective filter for charge transport.

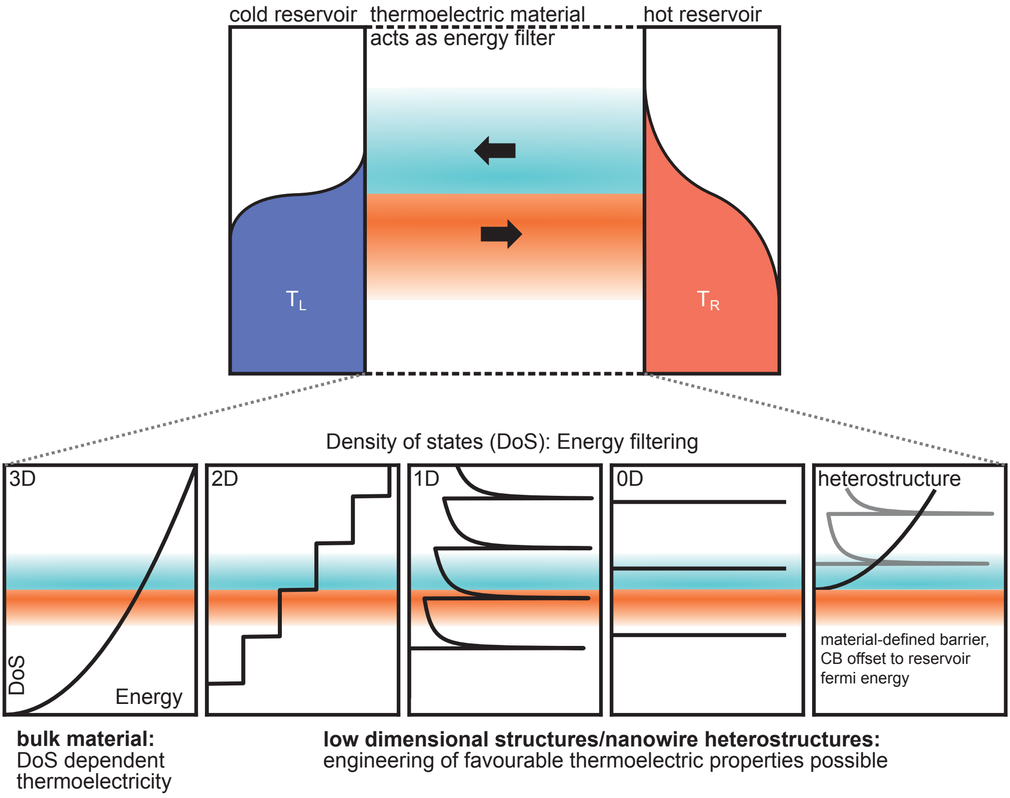

Figure 24: Principles of thermoelectricity and the advantage of nanoscale structures.

This asymmetry in the charge transport behavior of a given system is captured by its thermopower

$$S = \left(\frac{V_{th}}{\Delta T}\right)_{I=0} \tag{41}$$

defined by the open-circuit thermovoltage V_{th} which is generated as a result of the temperature difference between the hot- and cold reservoir ΔT [175]. In a linear response regime, valid only if the temperature difference on the length-scale of the mean free path of the system is small compared to the average temperature $\widetilde{T}$ [13], the thermocurrent $I_{th} = GS\Delta T$ is a function of the thermopower and the electrical conductance G of the system [175, 177]. Although this equation may not capture the relevant non-linear effects arising in mesoscopic TE devices [177], it is sufficient to illustrate a key challenge for TE applications: For the operation of a thermal energy harvester, the relevant quantity to maximize is its output power $P = R_{load} {I_{th}}^2$ over a load resistor R_{load}, which scales with the thermocurrent. Accordingly, good TE materials combine a large thermopower and electrical conductance with the ability to achieve and maintain large temperature differences between the thermal reservoirs, i.e. a low thermal conductance K.

The perfomance of TE generators can thus be quantified by various metrics, most notably the dimensionless figure of merit [174]

$$Z\widetilde{T} = \frac{G}{K} S^2 \widetilde{T} \tag{42}$$

or the efficiency

$$\eta = \frac{P}{J_h} \tag{43}$$

defined as the ratio of the generated power P to the heat flow J_h out of the hot reservoir [175]. The efficiency of heat-to-work conversion processes is bound by the Carnot limit, $\eta_c = 1 - (T_C/T_H)$ where T_H and T_C are the temperatures of the hot and cold reservoir [173]. The Carnot efficiency translates to an infinite figure-of-merit $Z\widetilde{T} = \infty$ [175], but in general the relation between $Z\widetilde{T}$ and η is complex [178] and both metrics come with drawbacks: The figure-of-merit's validity is limited to the linear response regime, requires temperature independent S, G, K and may thus not be a meaningful metric for the mesoscopic systems discussed later in this chapter [175, 177, 179]. In contrast, the efficiency is more generally applicable but requires knowledge of the heat flow, a quantity not easily accessible in experiments [122], and is thus complex to evaluate.

The figure-of-merit directly highlights the fundamental flaw of bulk TE materials. Because the density of states (DoS) of bulk materials possesses only a weak energy dependence (see fig. 24, 3D panel) [180] net thermocurrents in bulk systems remain small and the bulk thermopower is limited in magnitude. Additionally, efforts to increase P by enhancing G are futile in improving the device performance as the ratio G/K remains constant according to the Wiedemann-Franz law [181], which links the electronic to the thermal conductance [173]. Consequently, the development of bulk TE devices is widely limited to the hunt for materials that provide a favourable bandstructure to optimize S while maintaining a high ratio of G/K [174]. Inevitably, for bulk TE materials the figure-of-merit is found limited to $Z\widetilde{T} \leq 1$ [173, 174] (which corresponds to $0.17 \cdot \eta_c$ [175]) while efficiencies of around $0.33 \cdot \eta_c$ or $Z\widetilde{T} = 3$ are considered necessary for the widespread success of TE applications [173, 175].

In nanostructures, on the other hand, clever device design enables the engineering of favourable material properties to improve the performance of TE devices. This fundamentally different approach dates back to 1993, when Hicks and Dresselhaus studied the TE properties of 2D [182] and 1D [183] systems. Their findings indicate that at the nanoscale, as a consequence of the altered DoS, considerable improvements to the TE performance are possible [174]. The underlying principle is again illustrated in the bottom panels of fig. 24.

When compared to bulk, the DoS of low dimensional systems exhibits a stronger energy dependence, thus provides a better energy-filter and results in a higher thermopower [77]. An additional advantage of nanoscale systems lies in the increased phonon scattering on interfaces [64]. Because the thermal conductance $\mathrm{K} = \mathrm{K}_e + \mathrm{K}_{\mathrm{ph}}$ consists of an electronic- and a phononic contribution, engineering the shape and size of nanostructures can artificially enhance the ratio of G/K by reducing phonon-mediated heat leaks between the hot and cold reservoir. Furthermore, violations of the Wiedemann-Franz law are possible for mesoscopic conductors [184], and heterostructures, which can be designed with great flexibility in nanostructures, enable the design of material-defined energy filters [185]. In nanowires for instance, K_{ph} is reduced [186, 187] and various heterostructures are readily available [185]. Indeed, by engineering the electronic and phononic properties of materials with superstructures on the nanometer scale, $\widetilde{\mathrm{ZT}}$ of up to almost 2.5 have been achieved [174].

To maximize the TE efficiency Mahan and Sofo predicted in 1996 [188] that an ideal energy filter, characterized by a sharp and infinitely narrow transmission function is required. With such an ideal energy filter, in the absence of phonon heat leaks, charge and heat flow become strongly coupled and TE devices can in theory operate fully reversibly with efficiencies reaching the Carnot limit [189, 190]. Consequently, QDs coupled weakly to two electron reservoirs naturally provide ideal conditions and an experimentally available system for the realization of heat engines that can operate close to Carnot efficiency [179]. For QD heat engines, operation at the Curzon-Ahlborn efficiency, the approximate limit for the efficiency of an ideal heat engine that is operated at maximum output power, has further been theoretically predicted [63, 179]. Thermocurrents across QDs have been extensively studied since the mid 1990s and a summary of the early efforts can be found in the reviews in refs. [13, 191] and the references therein. Only in recent years, however, studies on InAs/InP nanowire based QDs with one heated contact have experimentally demonstrated QD heat engine operation at high efficiencies, exceeding $0.7 \cdot \eta_{\mathrm{c}}$ [77] as well as close to the Curzon-Ahlborn limit when the output power is maximized [65, 77, 192].

Up until this point, only so-called two-terminal devices were discussed, where the terminals refer to the number of thermal reservoirs to be considered for the relevant charge and heat transport processes. Although relatively simple and capable of high efficiencies, a major drawback of two-terminal heat engines is the inherently present link between charge and heat transport. As a result of this link, a temperature gradient is required within the electronic circuit of the heat engine, which is difficult to maximize and maintain for mesoscopic systems where the thermal reservoirs are closely spaced [13]. Three-terminal energy harvesters, on the other hand operate in a ratchet type configuration, where random fluctuations in the energy harvester's local environment are rectified and translated to a directional charge current [193]. This third terminal can thus be decoupled from the electronic circuit of the energy harvester such that only energy- but no charge exchange between the third terminal and the electronic circuit can occur. Consequently, the hot reservoir can be spatially separated from the cold reservoirs. Here, nanostructures again offer promising systems as they are highly sensitive to and interact with their local environment. Consequently, a variety of theoretical proposals for such three-terminal energy harvesters exist based on gated QD systems, where resonances serve as precisely controllable and near-ideal energy filters. A summary of theoretical proposals is given in the review in ref. [13] and many of the systems therein are predicted to reach the Carnot limit. In recent years, several such nanoscale energy harvesters have been experimentally demonstrated by rectification of thermal fluctuations in Coulomb-coupled quantum point contacts [194] or QDs [195] as well as by rectification of voltage fluctuations with Coulomb-coupled QDs [196]. A different implementation of a three-terminal thermal energy harvester makes use of a hot cavity sandwiched by two QDs, which mediate the charge transport to two cold electron reservoirs [197]. Interestingly, experimental implementations of nanoscale three-terminal energy harvesters, however, remain rare as compared to the large amount of theoretical proposals [177].

This disconnect between the theoretical and experimental efforts may in part be owed to the limited applicability for commercial devices. Mesoscopic energy harvesters to date require low operation temperatures and only produce tiny output powers in the femto- to pico Watt order of magnitude. Consequently, for viable applications significant parallelization and likely operation at room temperature would be required. For illustrative purposes, let us consider the case of a QD heat engine. Here, theoretical predictions suggest that output powers on the order of several Watts can be achieved by parallelization [198]. Further, Coulomb oscillations are detectable at room temperature in metallic nanoparticles [199], however the operation of a QD heat engine at the Cuzon-Ahlborn efficiency has yet to be demonstrated at temperatures beyond 30 K [192]. An imaginary commercial energy harvester based on a large amount of QDs defined in metallic nanoparticles would, however,still face significant technological challenges: To achieve ideal operation conditions either all QDs need highly homogeneous electrostatic properties, or electrostatic control over each individual QD is required. Further, Coulomb interactions between the QDs reduce the overall efficiency. In combination, these challenges show that the realization of a viable device seems far fetched given the current state of the field. A second reason for the lack of experiments on thermal energy harvesters may be rooted in the fundamental difficulty associated with measuring the performance of nanoscale energy harvesters. While the output power is easily detectable, quantifying the heat currents, which determine the device efficiency, is challenging. To date, efficiency estimates require either complex experimental techniques [200] or exact modelling of the device with excellent quantitative agreement to the experiment [77, 177].

With the authors lack of faith in widespread commercial viability of complex nanoscale thermoelectric power generators, the question *"Why should we study thermocurrents in QD* *systems?"* inevitably arises. First, it is noteworthy that with the increasing miniaturization of electronics and the development of quantum information applications, nanoscale systems are highly relevant in modern day information technology. For both, conventional electronics and quantum electronic circuits, heat dissipation becomes increasingly challenging and the concepts developed based on nanoscale TE devices may in the future be applied for the active cooling of hot spots. On a more fundamental level and in the author's opinion most interestingly, QD-based nanoscale thermal energy harvesters operate in an intriguing regime where (1) high efficiencies are accessible and the efficiency and power output of energy harvesters can be tuned with relative ease by e.g. using QD gates to vary the energetic position of the energy filters, (2) not only large ensembles but also single particles play an important role [64], (3) fluctuations in the environment play a crucial role, are rectified in three-terminal devices and the input and output energy of the device fluctuates [201, 202] and (4) quantum effects are present. Consequently, such systems offer a promising platform to study and probe fundamental thermodynamic concepts away from equilibrium and in the presence of quantum effects.

To probe that regime, in recent years a new class of inequalities, the so-called thermodynamic uncertainty relations (TURs) have gained significant attention from the theory community [14]. At their essence, TURs predict a cost-precision trade-off relationship between different thermodynamic quantities [203]. In transport systems the TURs bind the ratio of the current fluctuations $\langle\langle \mathrm{I}^2 \rangle\rangle$ to the average current $\langle \mathrm{I} \rangle^2$

$$\frac{\langle\langle \mathrm{I}^2 \rangle\rangle}{\langle \mathrm{I} \rangle^2} \geq \frac{2k_\mathrm{B}}{\Sigma} \tag{44}$$

by the entropy production Σ [14]. For thermal energy harvesters specifically, the TUR describes a trade-off between the output power, the power fluctuations and the efficiency [204]. This trade-off for instance illustrates that against intuition (Carnot efficiency requires reversible operation of the heat engine), in the presence of strong fluctuations, a thermal energy harvester can be operated at Carnot efficiency with finite output power [205]. Consequently, this highlights the relevance of characterizing nanoscale systems not only by average quantities but also fluctuations [206]. From experimental studies of TURs in QD-based thermal energy harvesters various intriguing insights can be gained: First, fluctuation measurements become a spectroscopic tool and help to experimentally identify bounds for otherwise hard to access quantities such as the efficiency or entropy production of the device. Second, as TURs are often derived solely from classical physics, violations in experiments can help to identify the presence of quantum effects on charge transport. Ultimately, the search for TUR violations in QD-based devices may thus provide a pathway to define a *"quantum advantage"* arising from actively using and controlling quantum-effects in thermal energy harvesters, beyond the progress made by going from bulk to nano, and lead to the development of new concepts for energy harvesters.

Here, this thesis contributes by providing a platform and developing the means to study

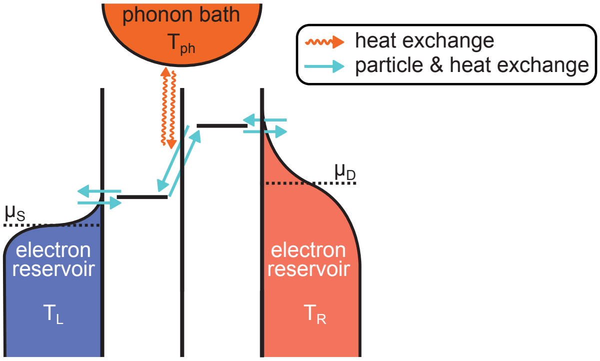

Figure 25: Illustration of a DQD coupled to three thermal reservoirs. The DQD is coupled to the phonon bath of its host material as well as the electron reservoirs serving as source- and drain contacts.

TURs in nanoscale energy harvesters. Existing three-terminal energy harvesters are realized in highly specialized systems with often complex and uncommon device architectures. In papers II and III we experimentally explore the possibility of operating conventional DQDs as versatile energy harvesters by studying thermocurrents across DQDs. As discussed in section 3, DQDs not only interact with the contact electron reservoirs but also emit phonons to the surrounding lattice during inelastic transport processes across detuned levels on the two QDs. Consequently, as illustrated in fig. 25, DQDs are naturally coupled to three thermal reservoirs: The contact electron reservoirs and the phonon bath with the phonon temperature T_{ph}, where the latter is purely coupled to the DQD via heat exchange. In paper II, we pick up on an old proposal for the realization of a three-terminal energy harvester by Entin-Wohlman et al. [12] where heat stored in the local phonon bath of a DQD is converted to a net thermocurrent via phonon-assisted transport (PAT). This PAT process is the exact inverse of conventional inelastic transport via phonon emission which occurs within the finite bias triangles in the DQD's charge stability diagram. Conceptually, using PAT for energy harvesting has been theoretically studied for a variety of DQD-related systems [207–210] and DQDs were proposed as platforms to realize phonon TE rectifiers and transistors [211]. Because of the presence of quantum coherences and possible cotunneling effects, it is finally noteworthy that TUR violations are predicted by theory in DQD-based energy harvesters [203, 212].

In paper II we begin by reviewing the literature and identify two distinct effects, the TE effect and PAT, that result in thermocurrent in a DQD. Figure 26(a) outlines regions in a DQD's charge stability diagram, close to a set of TPs, in which thermocurrents can be observed. To describe the TE effect and PAT, a DQD with a single energy level E_L and E_R on the left and right QD, respectively, is considered. In addition, for clarity the local coordinates $\epsilon = \mu_{SD} - (E_L + E_R)/2$ and $\Delta = E_L - E_R$ are defined. Here, μ_{SD} is the electro-chemical potential of the contacts in the absence of a voltage bias, ϵ energetically shifts the energy levels of the two QDs up or downwards with respect to μ_{SD} and Δ

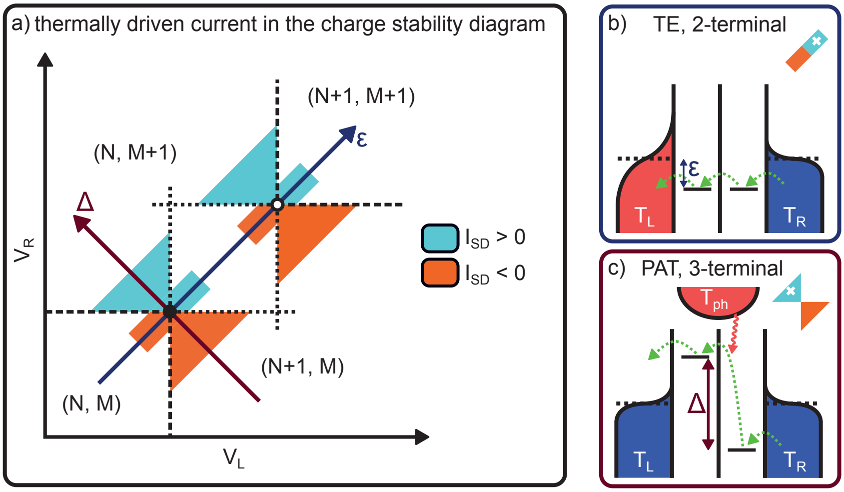

Figure 26: Thermally driven current in the DQD charge stability diagram. a) Thermocurrent regions in the DQD charge stability diagram near a set of TPs. b) Schematic illustration of the thermoelectric (TE) effect across a DQD. c) Schematic illustration of phonon-assisted transport (PAT) across a DQD. Figure adapted from paper II.

describes the level detuning.

The TE effect, as extensively discussed in section 4, occurs if the temperatures in the electron reservoirs differ, $T_L \neq T_R$ and is illustrated in fig. 26(b). In full analogy to the single QD case, the TE effect requires the DQD to act as an energy filter, is thus an elastic transport process and occurs only if levels across the two QDs are aligned, $\Delta = 0$. Then, along ϵ, the levels are pulled from above to below μ_{SD} and the DQD probes the heat induced electron population imbalance between the contact reservoirs. As a result, the characteristic TE thermocurrent signal occurs and reverses polarity wherever a TP is crossed in the charge stability diagram and is confined to small Δ only. In literature, the TE effect has been observed in a DQD tuned to the strong interdot coupling regime [213].

On the other hand, PAT is an inelastic transport process where energy is supplied by a hot phonon bath via phonon absorption. Consequently, PAT requires non-zero level detuning and is found along Δ in the charge stability diagram. The PAT process is illustrated in fig. 26(c) and requires the phonon temperature to exceed the electron temperatures in the contacts, $T_{ph} > T_{L,R}$ [75]. During the PAT process, an electron absorbs a phonon and is lifted from an occupied, energetically lower to an unoccupied, energetically higher state in the DQD, which in turn results in a directional net current. Within the charge stability diagram various constraints exist, which limit the regions in which PAT can be found: First and foremost, the PAT process requires an occupied initial- and an unoccupied final state between the two QDs and thus in the absence of a voltage bias E_L and E_R must be on opposite sides of the Fermi-surface [75]. Furthermore, the directionality of the electron transport during the PAT process is dependent on the sign of Δ. In combination, this limits the PAT thermocurrents to triangular shaped regions in close vicinity of TPs and the PAT thermocurrent vanishes and reverts polarity as the charge transfer line (where $\Delta = 0$) in the charge stability diagram is crossed. Finally, since phonons need to supply sufficient energy for an electron to overcome the level detuning, the extent of PAT along Δ is limited by the available phonon energies such that $E_{ph} \geq |\Delta|$ is fulfilled. This condition no longer holds true if $|\Delta| \gg k_B T_{ph}$. In literature, the PAT process has been experimentally observed in the form of phonon-mediated back action of charge sensors on transport through DQDs tuned to the weak interdot coupling regime [214–217].

9 Summary: Paper II and III

Based on the principles discussed above, we aim to establish nanowire-based DQDs as a viable and versatile platform to study nanoscale two- and three-terminal thermal energy harvesters as well as fundamental thermodynamic concepts in papers II and III. We therefore characterize thermally driven currents across a DQD in paper II and demonstrate a versatile device design with the ability to engineer the temperature profile along a gated nanowire in paper III.

Summary: Paper II

Here, paper II lays the foundation by presenting a comprehensive description of heat driven currents across a DQD which is coupled to three thermal reservoirs (source, drain electron reservoirs & phonon bath). We then combine finite bias spectroscopy with heated measurements and detailed modelling of the system and demonstrate how tuning of the interdot tunnel coupling provides tools to disentangle the TE and PAT contributions to the thermocurrent and show that PAT is sensitive to the excited-state spectrum of the DQD.

Figure 27(a) shows the experimental device where the DQD is epitaxially defined by three InP tunnel barriers incorporated in an InAs nanowire. A thermal bias can be introduced by running a current through a local Joule-heater electrode, aligned to the approximate position of the DQD structure within the nanowire, by application of a heating bias $dV_H = |V_{H1} - V_{H2}|$. This design enables heating of the lattice near the DQD such that the local phonon temperature exceeds those of the electron reservoirs of the DQD. We further find a small misalignment of the Joule-heater electrode with the DQD to result in asymmetric heating of the source- and drain electron reservoirs. Consequently, thermal biasing leads to a temperature difference $T_{ph} > T_L > T_R$ between the reservoirs coupled to the DQD.

By variation of the DQD occupation and gating-bias $(V_{H1} + V_{H2})/2$ on the heater-electrode, we tune the device between the intermediate and weak interdot coupling regime.

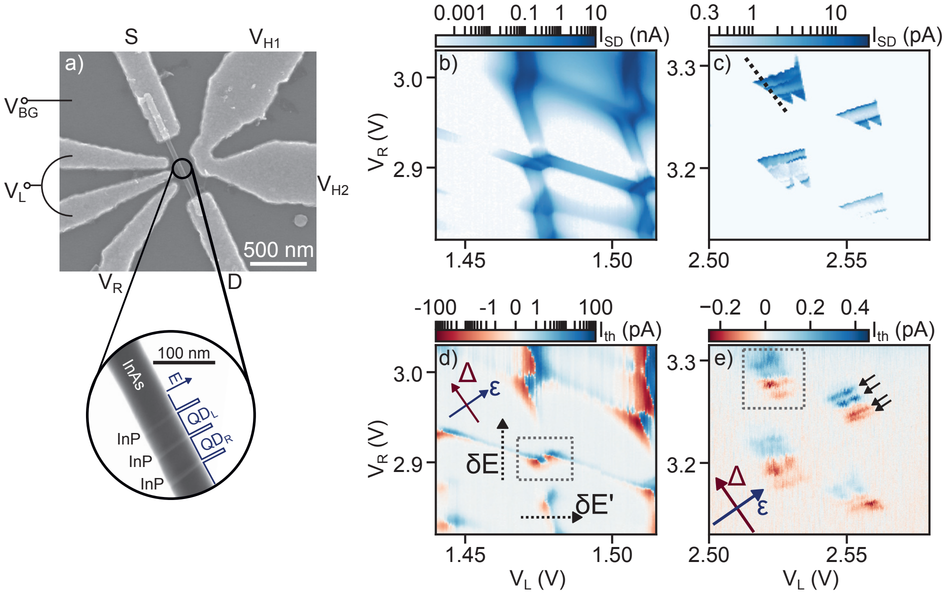

Figure 27: Heat driven currents in a DQD. a) Scanning electron micrograph of the device, consisting of an epitaxially defined DQD in a nanowire, a side-heater electrode and side-gates. b,c) Voltage bias driven currents in the intermediate (b) and weak (c) interdot coupling regime at $V_{SD} = 1\,\mathrm{mV}$ and $V_{SD} = 3\,\mathrm{mV}$, respectively. d,e) Thermocurrents in the intermediate (d) and weak (e) interdot coupling regime at $dV_H = 1\,\mathrm{V}$ and $dV_H = 4\,\mathrm{V}$, respectively. The current in (d) is plotted logarithmic with a linear range between $\pm 1\,\mathrm{pA}$. Adapted from paper II.

The results of finite bias spectroscopy in both regimes are shown in figs. 27(b) and (c). The corresponding heated measurements in figs. 27(d) and (e), where the grey dashed box labels a range comparable to fig. 26(a), illustrate a key finding of the study: In the intermediate interdot coupling regime we identify the TE effect as the predominant contribution to the thermocurrents while in the weak interdot coupling regime thermocurrents are dominated by PAT. This apparent shift of the main transport mechanism is explained with the presence of a finite tunnel coupling Ω between the two QDs. In the intermediate interdot coupling regime $\Delta \sim \Omega$ in vicinity of the TPs and thus molecular bonding and antibonding states form in the DQD. For the PAT process, this comes at considerable drawbacks. First, since molecular states extend across both QDs, the directionality of the PAT process is reduced. Second, as a result of eq. (30) phonons now have to supply a minimum energy of $E_{ph} > 2\Omega$ to overcome the spacing between the bonding and antibonding molecular state. The TE effect, on the other hand profits from the enhanced transmission across the DQD as a result of states extending across both QDs. The situation reverts when the DQD is tuned to the weak interdot coupling regime, where mixing between states on the left and right QD is suppressed. Here, PAT has a high directionality, while the TE effect is confined to the purely elastic transport regime at $\Delta = 0$ with a reduced magnitude due to the lower overall transmission.

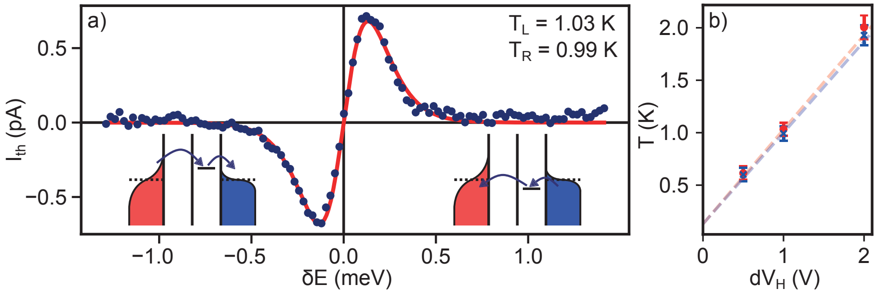

Figure 28: Electron temperature estimate in the intermetiate interdot coupling regime. a) Thermocurrent along a cutline comparable to $\delta \mathrm{E}$ in fig. 27(d) at $\mathrm{dV_H} = 1\,\mathrm{V}$. Here the DQD acts like a thermally biased single QD and the solid red line is a fit to the data to extract the contact electron temperatures. b) Contact electron temperature estimate as a function of the side-heater bias $\mathrm{dV_H}$. Each data point represents the median of several fits as shown in (a). Adapted from the supplemental material of paper II.

In the intermediate interdot coupling regime thermocurrents are further detected along the charging lines, see δE and δE′ in fig. 27(d). Here, the DQD behaves like a thermally biased single QD and thus the thermocurrents are the result of the TE effect only. With this observation, it becomes evident that the in general complex superposition of PAT and the TE effect can be separated for thermometry purposes. We therefore fit cutlines, as shown in fig. 28(a), with a simple rate equation based model for a spinless QD [63] and obtain an estimate for the contact electron temperatures (independent of $\mathrm{T_{ph}}$) as a function of $\mathrm{dV_H}$, see fig. 28(b).

Finally, we return to the PAT signal in the weak interdot coupling regime in fig. 27(e). The maximum extent of the PAT signal along Δ relates to the phonon energy and with knowledge of the phonon spectral function enables a contact temperature independent estimate of the phonon temperature. Additionally, pronounced resonances emerge within the PAT signal and are labelled by black arrows in fig. 27(e). To investigate the origin of these resonances further and gain insight into the relation between the phonon energy and $\mathrm{dV_H}$, we measure the voltage and thermal bias driven currents along the black dotted cutline indicated in fig. 27(c) as a function of $\mathrm{V_{SD}}$ and $\mathrm{dV_H}$. The results are shown in figs. 29(a) and (b), respectively, and we discover that the resonances in the PAT signal to approximately correspond to the excited-state spectrum observed in voltage biased measurements. By combining the experimental data with QmeQ simulations where we observe the same resonances, see figs. 29(c) and (d), we show that PAT through specific level configurations results in enhanced thermocurrents.

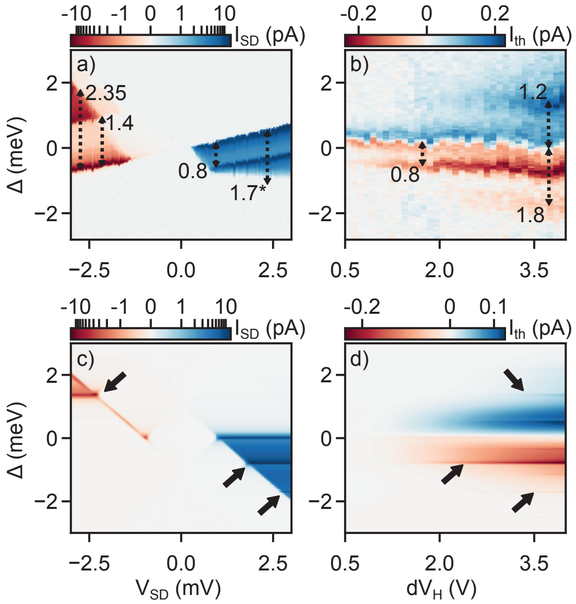

Figure 29: PAT and excited states. Experimental (a,b) and calculated (c,d) voltage bias (a,c) and PAT (b,d) driven currents along the black dotted cutline in fig. 27(c). The simulation temperatures are set according to the temperature estimates given in paper II. Resonances in the PAT currents are attributed to signatures of excited states in the voltage biased currents. Figure adapted from paper II.

Summary: Paper III

Paper III aims to overcome the shortcomings of the device studied in paper II: The capacitive coupling between the Joule-heater electrode and the DQD introduced significant complications for tuning the device and in combination with the epitaxial barriers resulted in only limited control over the DQD occupancies, tunnel couplings and the interdot coupling regime. In addition, the temperature gradient could only be controlled in magnitude but by design remained fixed otherwise and asymmetric with respect to the DQD. In paper III we present a proof-of-concept study of a more versatile device design, shown in fig. 30(a), where a bottom-gate architecture (7 gates, g1-7 from source to drain) is capacitively coupled to an InAs nanowire and selected gates (g1, g4, g7) double function as local Joule-heaters when a current is sent through the gate stripe. This device design enables the electrostatic definition of various barrier- and QD systems with in principle precise control over tunnel couplings, and introduces the ability to heat at different locations to engineer the temperature difference between the thermal reservoirs coupled to the device. Paper III demonstrates the device functionality by presenting thermocurrent measurements in various device configurations. The results are summarized in figs. 30, 31 and 32.

As a first device configuration we measure the TE effect across a barrier-free nanowire to

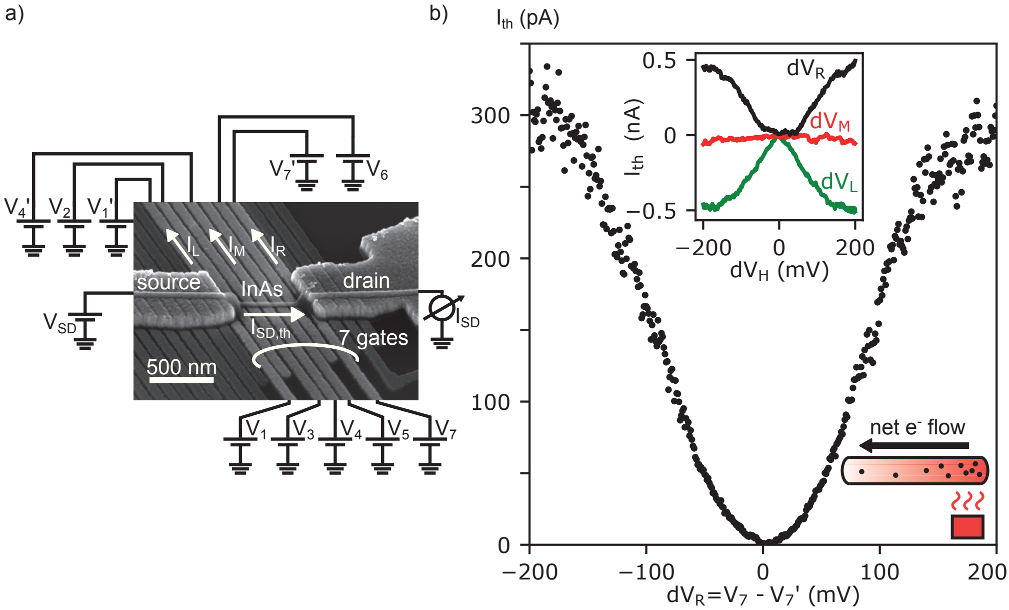

Figure 30: Bottom-heated nanowire device and heater characterization. a) Scanning electron micrograph of the device and illustration of the experimental setup. b) Thermocurrent across a conductive, barrier-free nanowire configuration as a function of the heating bias $\mathrm{dV_R} = \mathrm{V_7} - \mathrm{V'_7}$ on the rightmost active bottom-gate. Inset: Thermocurrent as a function of $\mathrm{dV_L}$, $\mathrm{dV_M}$ and $\mathrm{dV_R}$. Adapted from paper III.

demonstrate the heater functionality and symmetric heating of the contacted nanowire segment. The results are presented in fig. 30(b) where it is evident that the direction of current flow through the gate stripe has no impact on the thermocurrent. A comparison of the thermocurrents induced by different bottom-heaters (see inset) verifies a symmetric heating effect if heated on the left or right side of the nanowire segment. In contrast, if heat is applied in the middle of the device only small $\mathrm{I_{th}}$ are observed which suggests that a near symmetric temperature profile along the device is maintained.

For the second device configuration, a QD is electrostatically formed by inducing tunnel barriers with g2 and g4 or g4, as illustrated in fig. 31(b) , and g6. Figure 31(a) shows an exemplary charge stability diagram of a QD formed on the left side of the nanowire segment. We then measure the thermocurrents along the red dashed cutline in fig. 31(a) as a function of the heater bias applied to g1 and g7. From the symmetries of the thermocurrent, as illustrated in figs. 31(c-e) effective $0 \rightarrow 1$ and $1 \rightarrow 2$ charge state transitions are identified and we fit the TE signals with eq. (36) and eq. (37). The QD thermometry results reveal that the average temperature of the reservoirs, $\widetilde{\mathrm{T}}$, remains independent of the heater location while the temperature difference between the left and right electron reservoir $\Delta\mathrm{T}$ shows indications of a dependence on the distance between the QD and the heater. We believe this behaviour to be the result of a phononic heat flow contribution across the QD in com-

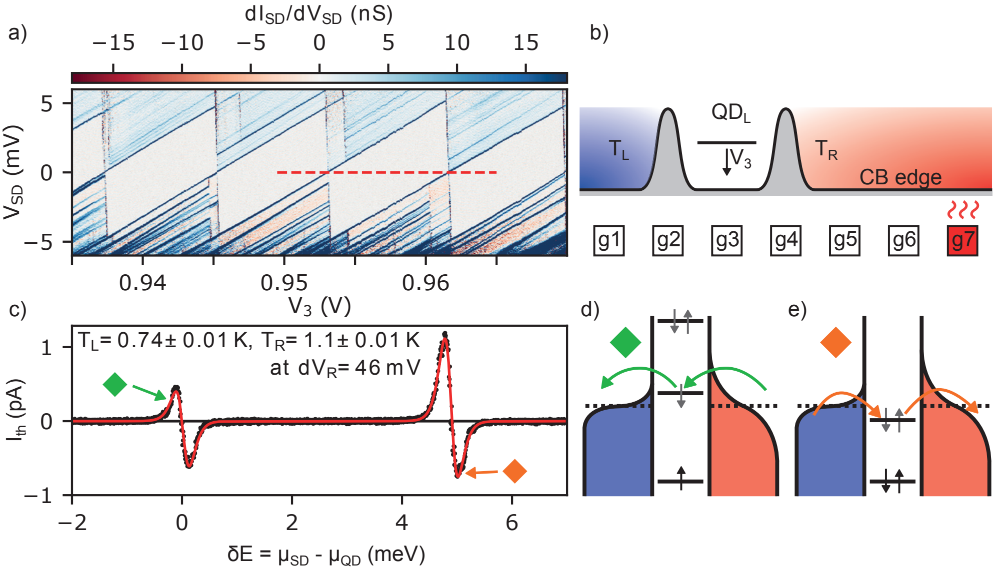

Figure 31: TE effect in an electrostatic defined QD. a) Charge stability diagram of a QD formed between g2 and g4 as indicated in (b). c) Thermocurrent along the red cutline in (a). The solid red line is a fit to the data for thermometry. d) TE effect across a QD level situated above μ_{SD} for an effective $1 \rightarrow 2$ charge state transition. e) TE effect across a QD level situated below μ_{SD} for an effective $0 \rightarrow 1$ charge state transition. Black arrows in (d) and (e) indicate electrons with a set spin confined to the QD and grey arrows indicate available states. Adapted from paper III.

bination with a phonon mean free path (PMFP) shorter than the nanowire segment. In that case, phonon-mediated heat flow across the QD reduces ΔT if the QD is formed close to the heater, while the phononic contribution to the heat flow across the QD is suppressed for a larger QD-to-heater distance and larger ΔT values are achievable.

As a final exemplary device configuration, we electrostatically define a DQD in the intermediate interdot coupling regime in the nanowire segment. Gate g4 forms the middle barrier and serves as middle heater and the resulting charge stability diagram is shown in fig.32(a). The thermocurrent measurements on this device configuration with heat supplied to the middle, left or right side of the DQD, presented in figs.32(b-d), illustrate key results of this study: First, PAT contributes significantly to the thermocurrents across the DQD, indicating that all three heaters efficiently elevate the temperature of the phonon bath beyond that of the electron reservoirs. A comparison of the extent of the PAT signal along Δ, see fig. 32(e), demonstrates a reduction of the available phonon energy for PAT if the device is heated at a distance from the DQD center and we estimate a PMFP of the order of the gate electrode spacing. Second, we find that if heat is supplied in the DQD center the TE effect is suppressed and can be introduced in a controlled manner by heating on either of the sides, on g1 or g7, instead. This becomes obvious in the thermocurrent on cutlines along ϵ in fig. 32(f). Consequently, the results prove that the combined bottom-gate and heater device architecture overcomes the shortcomings of the more simple design used in

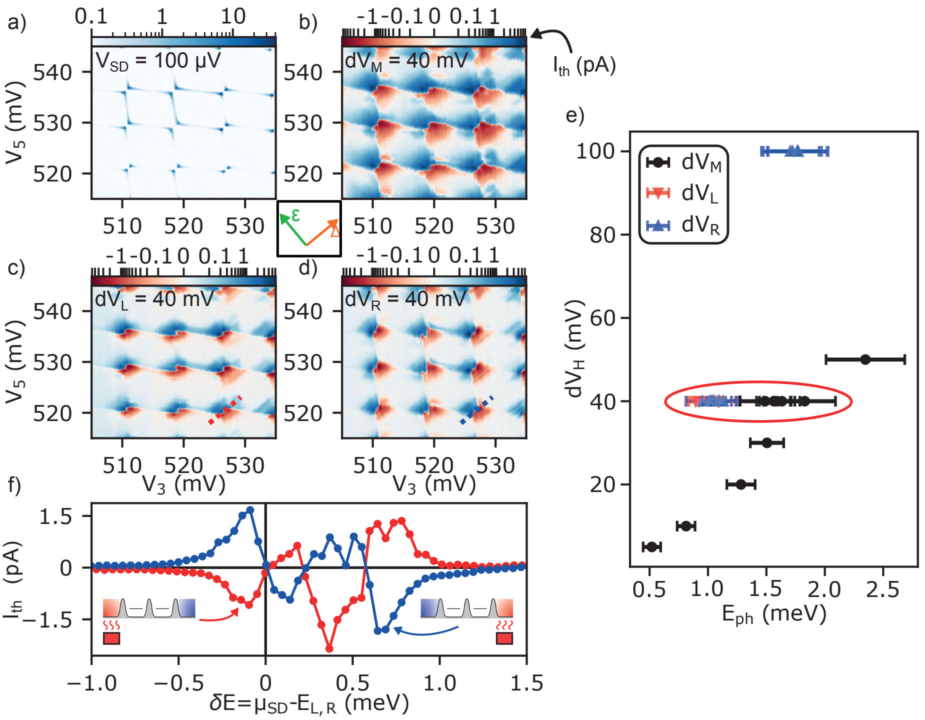

Figure 32: Thermucurrents in a bottom-heated DQD. a) Voltage biased charge stability diagram. b-d) Thermocurrents in the thermally biased charge stability diagram for different heater locations. e) Lower bound for the maximum phonon energy E_{ph} as a function of heating bias and heater location. f) TE current along the red and blue dotted cutlines in (c) and (d). Adapted from paper III.

paper II and is ideally suited to study DQD based thermal energy harvesters in a controlled environment.

10 Outlook: Probing thermodynamic uncertainty relations

A motivation for the studies presented in papers II and III is to provide viable platforms and generate the relevant understanding of thermally induced transport to study fundamental nanoscale thermodynamics by experimentally probing, and possibly violating, TURs in QD-based thermal energy harvesters. As is often the case with the underlying motivation of research work, details have so far remained rather vague and what steps such studies would entail is not immediately obvious. This outlook sets out to sketch how experiments probing TURs in QD systems could be designed and what challenges are to be overcome. Therefore, preliminary results of initial experiments on a simple system, a QD heat engine designed in full analogy to ref. [77], are presented. The QD heat engine consists of a quantum dot coupled to one cold and one hot electron reservoir and is operated in the absence of an external voltage bias, converting heat to current. Even such relatively simple devices are theoretically expected to violate classical TURs in the presence of cotunneling effects [203] and are thus interesting study objects.

For a QD heat engine, the general TUR in eq. (44) can be rewritten to

$$\frac{\langle P \rangle}{\langle\langle P^2 \rangle\rangle} = \frac{\eta}{\eta_c - \eta} k_B T_c \leq \frac{1}{2} \tag{45}$$

where T_c is the temperature of the cold electron reservoir, and describes a trade-off between the average output power $\langle P \rangle$, the power fluctuations $\langle\langle P^2 \rangle\rangle$ and the efficiency η of the heat engine [204]. Equation (45) defines the requirements for studying TURs in a QD heat engine: Because the TUR trade-off depends on the efficiency and power of the heat engine, ideally the operation regime should be continuously tunable to vary both the output power and the efficiency at which the heat engine operates. Further, in order to gain insight into the efficiency a detailed performance analysis of the device should be available. Efficiencies, however, depend on the heat current, which is not easily accessible in experiments and thus quantitative modelling of the system is required [77]. Finally, in addition to a traditional performance analysis, measurements of the heat engine's output power or current fluctuations are needed. In the following, all requirements are discussed and we show (1) how a QD heat engine can be characterized, create a digital twin of the device to analyze its performance and (2) demonstrate one possible path to measure the fluctuations in the system. The device design and heat engine performance analysis follows the study in ref. [77].

The experimental device and measurement circuit is shown in fig. 33(a). The QD is formed in an InAs/InP nanowire heterostructure where a $20\,\mathrm{nm}$ long InAs QD segment is enclosed by two $7\,\mathrm{nm}$ InP tunnel barriers and the substrate acts as a global backgate. Top Joule-heater electrodes are deposited atop the electrical contacts to the nanowire and various load resistors connected in series with the QD, of which in the following only a $1\,\mathrm{M\Omega}$ resistor is used, are cooled down to a base temperature of $15\,\mathrm{mK}$ with the device. Each measurement line has an additional low-pass cold-filter with a $1\,\mathrm{nF}$ capacitor shunt to ground and a $1\,\mathrm{k\Omega}$ resistance. For purposes of the later discussed fluctuation or noise measurements, instead of relying on conventional current measurements we detect the voltage drop over the load resistor $\Delta V = R_{\mathrm{load}} I_{\mathrm{th/SD}}$, which directly relates to the constant current through the circuit and thus also the current through the heat engine, $I_{\mathrm{th/SD}}$.

Figure 33(b) shows the operation region for the following experiments in the charge stability diagram of the QD. For the purposes of TUR experiments, where quantitative modelling will be relevant, we limit our study to a region where clear odd-even spin filling is observed. We further pick transitions where excited states are spaced several meV apart from the ground state and can thus be neglected in a theoretical model in the absence of a large external bias and for moderate heating. It should be noted that, as a direct drawback of

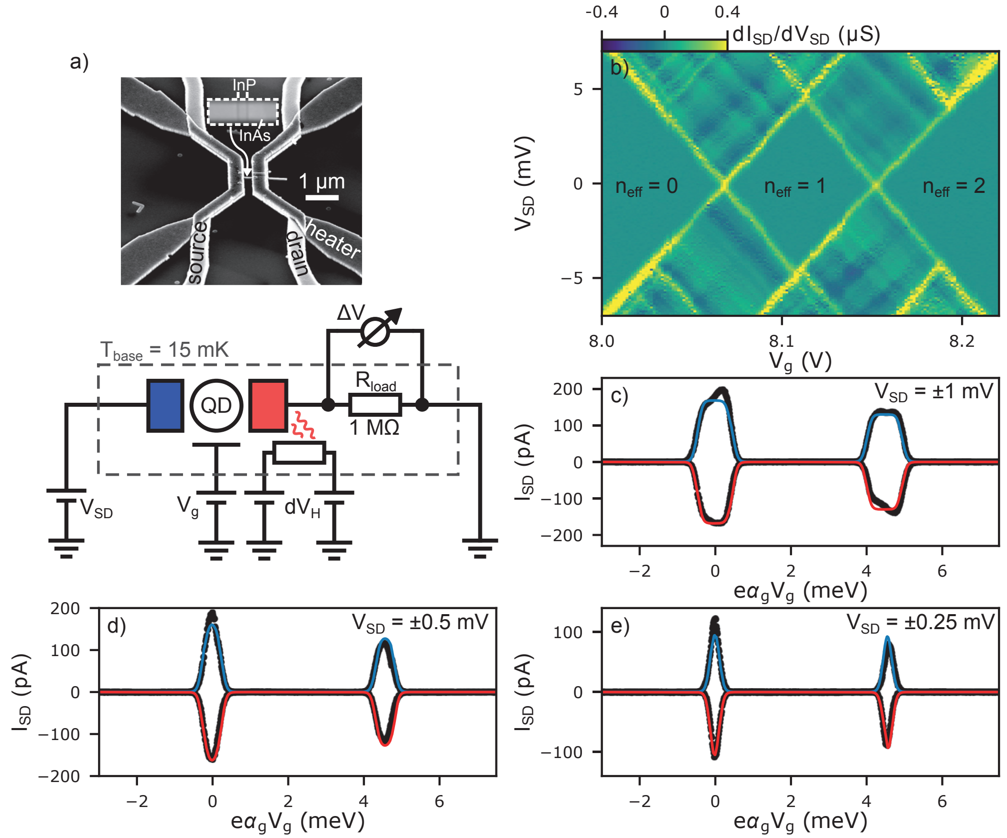

Figure 33: **Finite bias characterization of a QD heat engine.** a) Device and measurement setup. b) Charge stability diagram. The colorbar does not represent accurate values as the load resistor in the circuit is not considered in the calcualtion of dI_{SD}/dV_{SD}. c-e) Experimentally detected current $I_{SD} = \Delta V / R_{load}$ (black dots) through the circuit, measured at $V_{SD} = \pm 1\,mV$ (c), $V_{SD} = \pm 0.5\,mV$ (d) and $V_{SD} = \pm 0.25\,mV$ (e). Solid blue/red lines represent the current calculated with QmeQ and RTD with $\Gamma_{L/R} = 1.58\,GHz$ for the effective $0 \to 1$ as well as $\Gamma_{L/R} = 1.22\,GHz$ for the effective $1 \to 2$ charge state transition and $T_{L/R} = 540\,mK$. The (experimentally quantified) voltage drop over the load resistor is subtracted from the applied external bias at every gate voltage value.

the load resistor in the experimental circuit, because in the QDs most conductive state the load resistor accounts for around 20% of the total circuit resistance, only a part of the external bias V_{SD} drops over the heat engine. Since this is not accounted for in fig. 33(b) the differential conductance mapped on the colorbar does not represent accurate values.

In order to create a digital twin of the QD device, we implement a QD with a single spin degenerate resonance in QmeQ and use RTD to calculate all relevant quantities including second-order effects. For a quantitative description, knowledge of the tunnel couplings and charging energy of the QD is required as inputs for the model. The charging energy $E_c = 4.54 \pm 0.05\,meV$ is directly read out from fig. 33(b). To access tunnel couplings, we measure $I_{SD} = \Delta V / R_{load}$ for different values of the external bias $V_{SD} = \pm 1\,mV$,

$V_{SD} = \pm 0.5\,\mathrm{mV}$ and $V_{SD} = \pm 0.25\,\mathrm{mV}$ and the results are shown in figs. 33(c), (d) and (e), respectively. For $V_{SD} = 1\,\mathrm{mV}$ we expect the current through the QD to saturate, according to eq. (38), which allows to determine the tunnel couplings. We, however, find variations in the saturation current plateaus. Similar observations have recently been discussed as signatures of dark states, decoupled from either the source- or drain contact, [218] but in nanowires are more commonly attributed to DoS effects arising from the quasi-1D leads coupled to the QD which are affected by the global backgate [82]. Because these DoS variations make it difficult to independently determine the tunnel couplings across the left- and the right tunnel barrier, we in the following assume the tunnel couplings to be symmetric. From the saturation currents, a first estimate for the tunnel couplings is obtained. By further removing the experimentally detected voltage drop over the load resistor from the external bias V_{SD}, the real bias experienced by the heat engine is obtained and we fit fig. 33(d) and (e) for the electron temperature of the system. With the electron temperature, the data in fig. 33(c) is again compared to the model to increase the accuracy of the extracted tunnel couplings and the process is iteratively repeated. This fitting process yields $\widetilde{T} = 540\,\mathrm{mK}$ and $\Gamma_{L/R} = 1.58\,\mathrm{GHz}$ for the effective $0 \rightarrow 1$ as well as $\Gamma_{L/R} = 1.22\,\mathrm{GHz}$ for the effective $1 \rightarrow 2$ charge state transition. Deviations between the model and the experimental data in fig. 33 as well as the relatively high electron temperatures may be the result of asymmetric tunnel couplings and lifetime broadening of the QD levels, which is not accounted for in the model.

With the QD heat engine now prepared, we next turn our attention to quantifying fluctuations and test the noise measurement capabilities of our experimental setup. In order to quantify the output power fluctuations of the heat engine we detect fluctuations in the voltage drop ΔV across R_{load}. These noise measurement will contain contributions originating from fluctuations of the current through the QD as well as the Johnson-Nyquist thermal noise of the load resistor itself and the voltage preamplifier noise [219]. Consequently, because the latter contributions remain constant for any given temperature, tracking the change of the fluctuations of ΔV as a function of the the gate voltage V_g gives direct insight into the output current noise of the QD heat engine. Under moderate heating conditions, we expect the heat engine to operate around average temperatures of $\widetilde{T} \approx 1.5\,\mathrm{K}$. In a first estimate this sets the sensitivity requirement for noise measurements to the Johnson-Nyquist noise of a $1\,\mathrm{M\Omega}$ resistor at sub $1.5\,\mathrm{K}$ temperatures in order to resolve effects arising from fluctuations in the thermocurrent I_{th}.

In figure 34, we demonstrate the noise measurement capabilities by characterizing the Johnson-Nyquist noise of the load resistor in the absence of a QD in the electronic circuit as a function of the temperature. We therefore measure ΔV time traces with a $40\,\mathrm{kHz}$ sampling rate for $5\,\mathrm{s}$ using a Femto DLPVA voltage preamplifier, and an exemplary time trace at $T = 1\,\mathrm{K}$ is shown in fig. 34(a). From these time traces, the voltage noise power

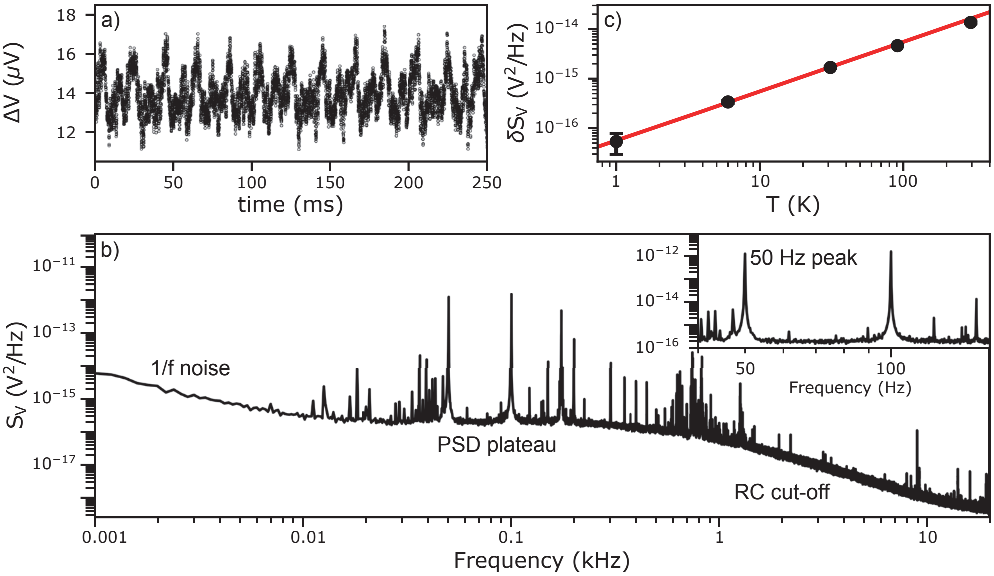

Figure 34: Noise measurements and thermometry. a) Voltage drop (ΔV) time trace over a load resistor $R_{\text{load}} = 1\,\text{M}\Omega$ at $T = 1\,\text{K}$ without a QD in the measurement circuit. The sampling rate is set to $40\,\text{kHz}$ and each time trace is measured for $5\,\text{s}$. b) Power spectral density (PSD) of the voltage fluctuations S_V. The PSD is obtained from time traces as shown in (a) and averaged 50 times. Inset: Plateau in S_V between the $50\,\text{Hz}$ and $100\,\text{Hz}$ peak. c) Black dots represent the median PSD plateau value, with a reference PSD removed to account for the amplifier noise, referred to as δS_V. Solid red line: Expected Johnson-Nyquist noise of a $1\,\text{M}\Omega$ resistor as a function of the temperature.

spectral density (PSD)

$$S_V = \frac{2}{\text{sr} \cdot N} \left| \text{FFT}\left(\Delta V(t)\right) \right|^2 \tag{46}$$

is computed by taking only the positive frequency contribution of the fast Fourier transform (FFT) of the time trace [219]. Here, sr is the sampling rate and N the number of data points per time trace. A 50-times averaged PSD at $T = 1\,\text{K}$ is plotted in fig. 34(b). For low frequencies, common $1/f$ noise is observed and for high frequencies S_V rolls off as a result of the low-pass filtering effect arising from the capacitances and resistances in the measurement lines (RC cut-off). Between around 20 Hz and 200 Hz the PSD plateaus. The various peaks observed in the PSD may originate from vibrations in the cryostat and characteristic peaks appearing at integer multiples of 50 Hz are attributed to the power mains.

Between 55 Hz and 95 Hz, see inset fig. 34(b), we identify a flat region in the PSD where no distinct peaks are present. Thus, this region is ideally suited and used in the following to quantify the noise of the system. To account for the voltage preamplifier noise, we substract a reference PSD signal, obtained at $T = 15\,\text{mK}$, where the Johnson-Nyquist noise is below the detection limit of the voltage preamplifier, and obtain the median value of the adjusted PSD between 55 Hz and 95 Hz, referred to as δS_V in the following. In fig. 34(c), δS_V is

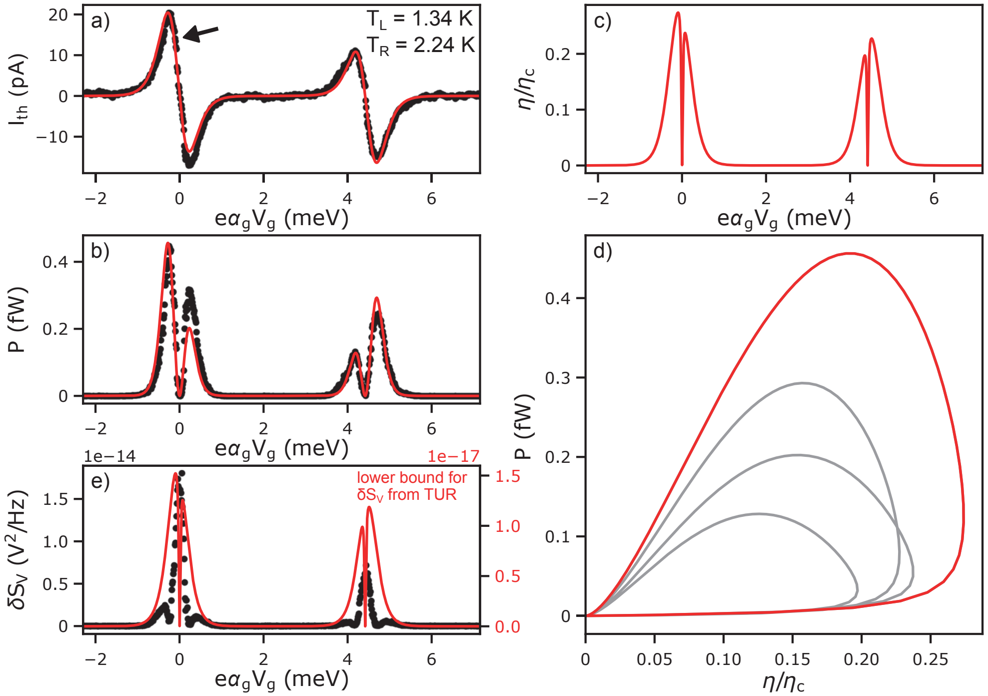

Figure 35: QD heat engine performance. a) Thermocurrent measurement. The solid red line represents a fit of a QmeQ and RTD based model for thermometry using the tunnel couplings obtained from fig. 33(c-e). b) Experimental output power (black dots) and calculated output power (solid red line). c) Calculated efficiency. d) Power-efficiency loops. The highlighted red loop corresponds to the I_{th} peak labelled with a black arrow in (a) where good agreement between the experiment and calculations is found in (a) and (b). e) Experimentally detected ΔPSD values (black dots) compared to the lower bound for the voltage fluctuations given by the TUR for the QmeQ calculated output power and efficiencies.

plotted as a function of the temperature and compared to the expected Johnson-Nyquist noise $S_V = 4k_B T R_{load}$ [219] of R_{load} (solid red line). The good agreement indicates sufficient sensitivity of the employed noise characterization technique.

Next, we combine the above outlined noise measurements with a characterization of the QD heat engine. We therefore, in the absence of an external voltage bias, heat the right contact of the QD and vary the voltage on the global backgate. For each gate voltage value, we record time traces for ΔV and obtain the current through the circuit from the average of the time traces. The experimental results (black dots) for the thermocurrent and output power of the QD heat engine $P = R_{load} {I_{th}}^2$ are shown in fig. 35(a) and (b), respectively. To characterize the temperatures of the source- and drain electron reservoir, the experimental results are compared to the QmeQ and RTD based model, where the voltage build-up V_{qd} across the QD as a result of the load resistor in the circuit is accounted for by self-consistently solving $I_{th}(V_{qd}) + V_{qd}/R_{load} = 0$ for each value of V_g [77]. We find best agreement between the model (solid red line in fig. 35) and the experiment for $T_L = 1.34\,K$ and $T_R = 2.24\,K$. Deviations between the model and experiment may again be the result of asymmetric tunnel couplings, and a comparison of the output power in fig. 35(b) shows that the quantitative agreement is not ideal for this particular dataset.

Nevertheless, based on the QmeQ model, it is possible to estimate the performance of the device by computing the efficiency η as a function of V_g in fig. 35(c) and we find the efficiency to reach up to 27% of η_c. Figure 35(d) illustrates the trade-off between P and η in our device through power-efficiency loops. Here, each loop is obtained by following one peak or dip in the thermocurrent and the highlighted red loop corresponds to the highest thermocurrent peak, marked by a black arrow in fig. 35(a), where agreement between the experiment and model is good.

Finally, fig. 35(e) compares δS_V to the lower bound for the fluctuations according to eq. (45). The lower bound for δS_V is computed with the power and efficiency obtained from the QmeQ model. While both the experimental δS_V and the corresponding calculated bound show a distinct increase surrounding the charge transition points, the experimental data exhibits a maximum where its bound has a minimum at the exact location of the charge transition point. Furthermore, we find δS_V to be several orders of magnitudes above the theoretical bound provided by the TUR. Although it should be noted that eq. (45) is an inequality and thus the bound does not explicitly translate to an expectation value for the experimental data, the singificant difference in magnitude suggests a problem with the sensitivity of the noise measurement technique toward the signal contribution of interest.

A problem with the sensitivity of noise measurements in the here presented dataset becomes more evident in fig. 36(a). Here, δS_V is plotted against V_g (black dots) for the first resonance only and the data is overlayed with the slope of S_V (red dots), extracted in the frequency range used to determine δS_V. The result clearly indicates that plateaus in the PSD cease to exist, which in turn makes it difficult to draw meaningful insights from δS_V. Figure 36(b) shows a time trace at the point where the highest δS_V is detected in (a). Unlike the time trace presented in fig. 34(a), the data in fig. 36(b) shows switching-type variations of the average ΔV on a ms time scale. In the resulting PSD, see fig. 36(c), this noise signature results in a $1/f^a$ behaviour where a approaches 2 [220], and the absence of a plateau renders the here employed analysis technique futile.

We further find, that δS_V as well as the slope of S_V is increased exactly for values of V_g where dI_{th}/dV_g is large. We thus attribute the switching-type noise in the time traces to instabilities of the gate voltage source, which can drastically alter the current through the device and thus also ΔV in a regime where the current depends strongly on V_g. For future studies, this presents a challenge to be overcome. Possible solutions range from employing a more stable, battery powered voltage source to introducing voltage dividers and filters to the output of the gate voltage source. Indeed, we observe a decrease in the switching-type noise of the time traces if a voltage divider is used on the gate. Another possible approach evolves around data processing. Since noise contributions are of additive nature in the

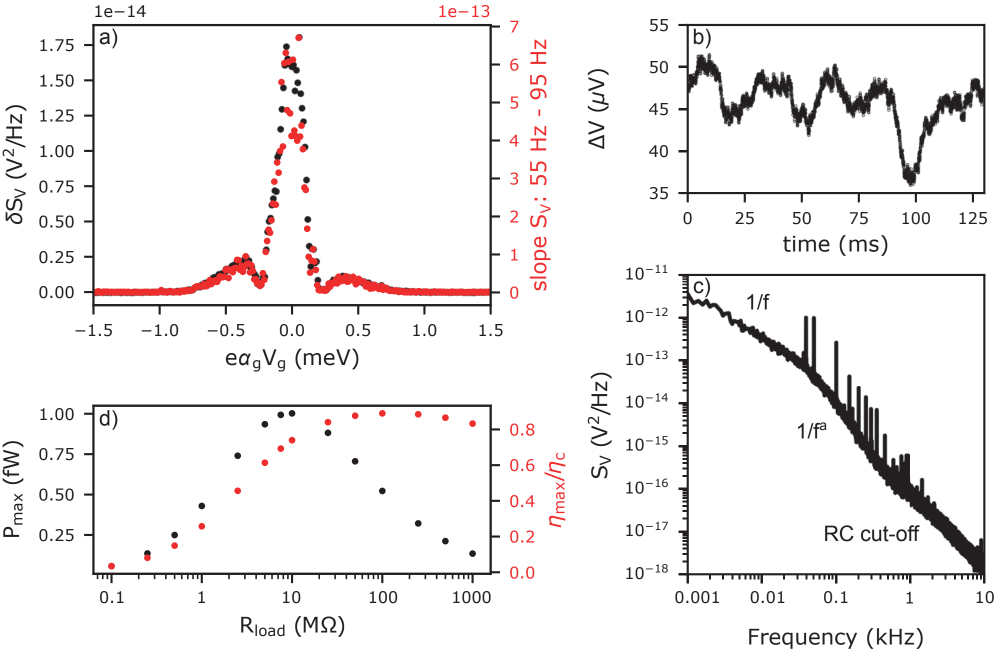

Figure 36: Challenges for probing the TUR in experiments. a) Comparison of the measurement result for δS_V to the slope of the S_V between 55 Hz and 95 Hz. b) ΔV time trace obtained at the point of maximum δV_g in (a). c) 50-times average PSD, measured at $e\alpha_g V_g = 0$. d) Maximum expected output power and efficiency of the here studied QD heat engine as a function of R_{load}, calculated with QmeQ using RTD.

PSD [220], the gate voltage induced noise contribution could be removed from the data by subtracting the $1/f^a$-type slope from the S_V. Other possibilities include analyzing the time traces in histogram form, or directly processing the time trace data before the conversion to a PSD, all of which however come at the risk of accidental modifications to the signal under investigation. Only once these obstacles are overcome an assessment on whether or not the sensitivity of the here discussed noise measurement technique is sufficient can be made.

Another challenge that these experiments may face in the future is the dependence of the achievable maximum power and efficiency of individual QD heat engines on the choice of R_{load}. The lower bound for the power fluctuations scales directly on P and η and thus operating the device under conditions where a beneficial power-efficiency trade-off can be reached is important for TUR experiments. For the particular device characterized in this outlook, the maximum power P_{max} and efficiency η_{max} is calculated as a function of R_{load} in fig. 36(d) using QmeQ. Although, for any given R_{load}, P_{max} and η_{max} can not be achieved in the same gate voltage configuration (see: fig. 35(d)) [221], the data in fig. 36 suggests that $R_{\mathrm{load}} \approx 10\,\mathrm{M\Omega}$ may be better suited to push the TUR bound for the fluctuations of the here discussed device into a detectable regime. On the other hand, the choice of R_{load} will directly impact the RC cut-off and thus large resistive loads can introduce challenges to maintain a sufficient bandwidth for measurements.

Despite the obstacles encountered during the here presented initial attempt to probe TURs via noise measurements in a QD heat engine, the author is optimistic that the challenges identified in this outlook can be overcome. Further optimization of the measurement setup in combination with more advanced data analysis approaches, as sketched in this outline, provide a promising path forward. In the future, one could boldly envision a combination of the device architecture presented in paper III with noise measurement techniques. In the author's opinion the concepts developed in this thesis set the stage to systematically study TUR boundaries in a variety QD systems with the goal to identify TUR violations in the future. This research direction offers the intriguing possibility to combine experimental and theoretical efforts and ultimately could help to quantify a quantum advantage for nanoscale thermal energy harvesters, operated in a regime where quantum effects matter.

References

[1] Boris Zhitkov. *Translated from Microhands: A fantastic essay*. 1931.

[2] C. P. Poole Jr and F. J. Owens. *Introduction to nanotechnology*. John Wiley & Sons, 2003.

[3] J. P. Dowling and G. J. Milburn. Quantum technology: the second quantum revolution. *Philos. Trans. Royal Soc. A*, 361(1809):1655–1674, 2003.

[4] S. M. Reimann and M. Manninen. Electronic structure of quantum dots. *Rev. Mod. Phys.*, 74:1283, 2002.

[5] W. G. Van der Wiel, S. De Franceschi, J. M. Elzerman, T. Fujisawa, S. Tarucha, and L. P. Kouwenhoven. Electron transport through double quantum dots. *Rev. Mod. Phys.*, 75(1):1, 2002.

[6] R. Hanson, L. P. Kouwenhoven, J. R. Petta, S. Tarucha, and L. M. K. Vandersypen. Spins in few-electron quantum dots. *Rev. Mod. Phys.*, 79(4):1217, 2007.

[7] D. P. DiVincenzo. Quantum computation. *Science*, 270(5234):255–261, 1995.

[8] C. H. Bennett and David P. DiVincenzo. Quantum information and computation. *Nature*, 404(6775):247–255, 2000.

[9] D. Loss and D. P. DiVincenzo. Quantum computation with quantum dots. *Phys. Rev. A*, 57(1):120, 1998.

[10] S. M. Frolov, S. R. Plissard, S. Nadj-Perge, L. P. Kouwenhoven, and E. P. A. M. Bakkers. Quantum computing based on semiconductor nanowires. *MRS Bull.*, 38 (10):809–815, 2013.

[11] D. Brunner, B. D. Gerardot, P. A. Dalgarno, G. Wüst, K. Karrai, N. G. Stoltz, P. M. Petroff, and R. J. Warburton. A coherent single-hole spin in a semiconductor. *Science*, 325(5936):70–72, 2009.

[12] O. Entin-Wohlman, Y. Imry, and A. Aharony. Three-terminal thermoelectric transport through a molecular junction. *Phys. Rev. B*, 82:115314, 2010.

[13] B. Sothmann, R. Sánchez, and A. N. Jordan. Thermoelectric energy harvesting with quantum dots. *Nanotechnology*, 26(3):032001, 2014.

[14] J. M. Horowitz and T. R. Gingrich. Thermodynamic uncertainty relations constrain non-equilibrium fluctuations. *Nat. Phys.*, 16:15–20, 2020.

[15] F. Rossi. *Theory of Semiconductor Quantum Devices: Microscopic Modeling and Simulation Strategies.* NanoScience and Technology. Springer Berlin Heidelberg, 2011.

[16] J. H. Davies. *The Physics of Low-dimensional Semiconductors: An Introduction*. Cambridge University Press, 1997.

[17] T. Ihn. *Semiconductor nanostructures: quantum states and electronic transport.* Oxford University Press, 2010.

[18] W. J. Parak, L. Manna, and T. Nann. *Fundamental Principles of Quantum Dots*. American Cancer Society, 2010.

[19] L. P. Kouwenhoven, C. M. Marcus, P. L. McEuen, S. Tarucha, R. M. Westervelt, and N. S. Wingreen. Electron transport in quantum dots. In *Mesoscopic electron transport*, pages 105–214. Springer, 1997.

[20] M. Born and R. Oppenheimer. Zur Quantentheorie der Molekeln. *Ann. Phys.*, 389 (20):457–484, 1927.

[21] F. Bloch. Über die Quantenmechanik der Elektronen in Kristallgittern. *Z. Phys.*, 52 (7):555–600, 1929.

[22] M. A. Kastner. Artificial atoms. *Phys. Today*, 46:24, 1993.

[23] C. J. Gorter. A possible explanation of the increase of the electrical resistance of thin metal films at low temperatures and small field strengths. *Physica*, 17(8):777–780, 1951.

[24] C. A. Neugebauer and M. B. Webb. Electrical conduction mechanism in ultrathin, evaporated metal films. *J. Appl. Phys.*, 33(1):74–82, 1962.

[25] C. W. J. Beenakker. Theory of coulomb-blockade oscillations in the conductance of a quantum dot. *Phys. Rev. B*, 44:1646, 1991.

[26] E. B. Foxman, P. L. McEuen, U. Meirav, N. S. Wingreen, Y. Meir, P. A. Belk, N. R. Belk, M. A. Kastner, and S. J. Wind. Effects of quantum levels on transport through a coulomb island. *Phys. Rev. B*, 47:10020, 1993.

[27] H. Van Houten, C. W. J. Beenakker, and A. A. M. Staring. Coulomb-blockade oscillations in semiconductor nanostructures. In *Single charge tunneling*, pages 167–216. Springer, 1992.

[28] P. L. McEuen, Ned S. Wingreen, E. B. Foxman, Jari Kinaret, U. Meirav, M. A. Kastner, Y. Meir, and S. J. Wind. Coulomb interactions and energy-level spectrum of a small electron gas. *Physica B Condens. Matter*, 189(1):70–79, 1993.

[29] H. Grabert. Single charge tunneling: A brief introduction. *Z. Phys. B*, 85(3):319–325, 1991.

[30] P. Werner and M. Troyer. Effective charging energy of the single-electron box. *J. Stat. Mech. Theory Exp.*, 2005:P01003, 2005.

[31] T. Dittrich, P. Hänggi, B. Kramer, G. Schön, G. L. Ingold, and W. Zwerger. *Quantum Transport and Dissipation*. Wiley, 1998.

[32] H. Grabert and M. H. Devoret. *Single Charge Tunneling: Coulomb Blockade Phenomena In Nanostructures*. Advances in Experimental Medicine & Biology. Springer US, 1992.

[33] C. C. Escott, F. A. Zwanenburg, and A. Morello. Resonant tunnelling features in quantum dots. *Nanotechnology*, 21(27):274018, 2010.

[34] T. Fujisawa, T. H. Oosterkamp, W. G. van der Wiel, B. W. Broer, R. Aguado, S. Tarucha, and L. P. Kouwenhoven. Spontaneous emission spectrum in double quantum dot devices. *Science*, 282(5390):932–935, 1998.

[35] N. C. van der Vaart, S. F. Godijn, Y. V. Nazarov, C. J. P. M. Harmans, J. E. Mooij, L. W. Molenkamp, and C. T. Foxon. Resonant tunneling through two discrete energy states. *Phys. Rev. Lett.*, 74:4702, 1995.

[36] C. Weber, A. Fuhrer, C. Fasth, G. Lindwall, L. Samuelson, and A. Wacker. Probing confined phonon modes by transport through a nanowire double quantum dot. *Phys. Rev. Lett.*, 104:036801, 2010.

[37] P. Roulleau, S. Baer, T. Choi, F. Molitor, J. Güttinger, T. Müller, S. Dröscher, K. Ensslin, and T. Ihn. Coherent electron–phonon coupling in tailored quantum systems. *Nat. Commun.*, 2(1):1–6, 2011.

[38] T. R. Hartke, Y.-Y. Liu, M. J. Gullans, and J. R. Petta. Microwave detection of electron-phonon interactions in a cavity-coupled double quantum dot. *Phys. Rev. Lett.*, 120:097701, 2018.

[39] K. Ono, D. G. Austing, Y. Tokura, and S. Tarucha. Current rectification by pauli exclusion in a weakly coupled double quantum dot system. *Science*, 297(5585):1313–1317, 2002.

[40] J. Ridderbos. *Quantum Dots and Superconductivity in Ge-Si Nanowires*. PhD thesis, University of Twente, 2018.

[41] A. C. Johnson, J. R. Petta, C. M. Marcus, M. P. Hanson, and A. C. Gossard. Singlet-triplet spin blockade and charge sensing in a few-electron double quantum dot. *Phys. Rev. B*, 72:165308, 2005.

[42] R. Li, F. E. Hudson, A. S. Dzurak, and A. R. Hamilton. Pauli spin blockade of heavy holes in a silicon double quantum dot. *Nano Lett.*, 15(11):7314–7318, 2015.

[43] H. W. Liu, T. Fujisawa, T. Hayashi, and Y. Hirayama. Pauli spin blockade in co-tunneling transport through a double quantum dot. *Phys. Rev. B*, 72:161305, 2005.

[44] J. K. Perron, M. D. Stewart, and N. M. Zimmerman. A new regime of pauli-spin blockade. *J. Appl. Phys.*, 119(13):134307, 2016.

[45] T. H. Oosterkamp, T. Fujisawa, W. G. van der Wiel, K. Ishibashi, R. V. Hijman, S. Tarucha, and L. P. Kouwenhoven. Microwave spectroscopy of a quantum-dot molecule. *Nature*, 395(6705):873–876, 1998.

[46] R. H. Blick, D. Pfannkuche, R. J. Haug, K. von Klitzing, and K. Eberl. Formation of a coherent mode in a double quantum dot. *Phys. Rev. Lett.*, 80:4032, 1998.

[47] G. Klimeck, G. Chen, and S. Datta. Conductance spectroscopy in coupled quantum dots. *Phys. Rev. B*, 50:2316, 1994.

[48] S. Gustavsson, M. Studer, R. Leturcq, T. Ihn, K. Ensslin, D. C. Driscoll, and A. C. Gossard. Detecting single-electron tunneling involving virtual processes in real time. *Phys. Rev. B*, 78:155309, 2008.

[49] D. V. Averin, A. N. Korotkov, and K. K. Likharev. Theory of single-electron charging of quantum wells and dots. *Phys. Rev. B*, 44(12):6199, 1991.

[50] C. W. J. Beenakker and A. A. M. Staring. Theory of the thermopower of a quantum dot. *Phys. Rev. B*, 46(15):9667, 1992.

[51] T. A. Fulton and G. J. Dolan. Observation of single-electron charging effects in small tunnel junctions. *Phys. Rev. Lett.*, 59(1):109, 1987.

[52] J. H. F. Scott-Thomas, S. B. Field, M. A. Kastner, H. I. Smith, and D. A. Antoniadis. Conductance oscillations periodic in the density of a one-dimensional electron gas. *Phys. Rev. Lett.*, 62(5):583, 1989.

[53] S. B. Field, M. A. Kastner, U. Meirav, J. H. F. Scott-Thomas, D. A. Antoniadis, H. I. Smith, and S. J. Wind. Conductance oscillations periodic in the density of one-dimensional electron gases. *Phys. Rev. B*, 42(6):3523, 1990.

[54] P. L. McEuen, E. B. Foxman, U. Meirav, M. A. Kastner, Yigal Meir, N. S. Wingreen, and S. J. Wind. Transport spectroscopy of a coulomb island in the quantum hall regime. *Phys. Rev. Lett.*, 66(14):1926, 1991.

[55] A. T. Johnson, L. P. Kouwenhoven, W. De Jong, N. C. Van der Vaart, C. J. P. M. Harmans, and C. T. Foxon. Zero-dimensional states and single electron charging in quantum dots. *Phys. Rev. Lett.*, 69(10):1592, 1992.

[56] M. A. Kastner. The single-electron transistor. *Rev. Mod. Phys.*, 64(3):849, 1992.

[57] M. A. Kastner. The single electron transistor and artificial atoms. *Ann. Phys.*, 9(11-12): 885–894, 2000.

[58] E. Bonet, M. M. Deshmukh, and D. C. Ralph. Solving rate equations for electron tunneling via discrete quantum states. *Phys. Rev. B*, 65(4):045317, 2002.

[59] A. Svilans, A. M. Burke, S. Svensson, M. Leijnse, and H. Linke. Nonlinear thermoelectric response due to energy-dependent transport properties of a quantum dot. *Physica E Low Dimens. Syst. Nanostruct.*, 82:34–38, 2016.

[60] K. Walczak. Coulomb blockade in molecular quantum dots. *Open Phys.*, 4(1):8–19, 2006.

[61] J. Koch, F. Von Oppen, Y. Oreg, and E. Sela. Thermopower of single-molecule devices. *Phys. Rev. B*, 70(19):195107, 2004.

[62] M. Josefsson. Thermoelectric transport and thermometry of quantum dots. Master's thesis, Lund University, 2015.

[63] M. Esposito, K. Lindenberg, and C. Van den Broeck. Thermoelectric efficiency at maximum power in a quantum dot. *Europhys. Lett.*, 85(6):60010, 2009.

[64] H. Thierschmann. *Heat conversion in quantum dot systems*. PhD thesis, Universität Würzburg, 2014.

[65] M. Josefsson, A. Svilans, H. Linke, and M. Leijnse. Optimal power and efficiency of single quantum dot heat engines: Theory and experiment. *Phys. Rev. B*, 99(23): 235432, 2019.

[66] I. G. Medvedev. Effect of interdot coulomb repulsion on tunneling current through a double quantum dot system in the weak tunneling limit: Strong electron-phonon coupling. *Phys. Rev. B*, 80(3):035312, 2009.

[67] H.-P. Breuer and F. Petruccione. *The Theory of Open Quantum Systems.* Oxford University Press, Oxford, 2007. ISBN 9780199213900.

[68] J. N. Pedersen and A. Wacker. Modeling of cotunneling in quantum dot systems. *Physica E Low Dimens. Syst. Nanostruct.*, 42(3):595–599, 2010.

[69] S. Koller, M. Grifoni, M. Leijnse, and M. R. Wegewijs. Density-operator approaches to transport through interacting quantum dots: Simplifications in fourth-order perturbation theory. *Phys. Rev. B*, 82(23):235307, 2010.

[70] C. Timm. Tunneling through molecules and quantum dots: Master-equation approaches. *Phys. Rev. B*, 77(19):195416, 2008.

[71] M. Leijnse and M. R. Wegewijs. Kinetic equations for transport through single-molecule transistors. *Phys. Rev. B*, 78(23):235424, 2008.

[72] J. König, H. Schoeller, and G. Schön. Cotunneling at resonance for the single-electron transistor. *Phys. Rev. Lett.*, 78(23):4482, 1997.

[73] B. Goldozian, F. A. Damtie, G. Kiršanskas, and A. Wacker. Transport in serial spinful multiple-dot systems: The role of electron-electron interactions and coherences. *Sci. Rep.*, 6(1):1–10, 2016.

[74] G. Kiršanskas, J. N. Pedersen, O. Karlström, M. Leijnse, and A. Wacker. Qmeq 1.0: An open-source python package for calculations of transport through quantum dot devices. *Comput. Phys. Commun.*, 221:317–342, 2017.

[75] B. Goldozian, G. Kiršanskas, F. A. Damtie, and A. Wacker. Quantifying the impact of phonon scattering on electrical and thermal transport in quantum dots. *Eur. Phys. J. Spec. Top.*, 227(15):1959–1967, 2019.

[76] N. M. Gergs, C. B. M. Hörig, M. R. Wegewijs, and D. Schuricht. Charge fluctuations in nonlinear heat transport. *Phys. Rev. B*, 91(20):201107, 2015.

[77] M. Josefsson, A. Svilans, A. M. Burke, E. A. Hoffmann, S. Fahlvik, C. Thelander, M. Leijnse, and H. Linke. A quantum-dot heat engine operating close to the thermodynamic efficiency limits. *Nat. Nanotechnol.*, 13(10):920–924, 2018.

[78] I. Žutić, J. Fabian, and S. Das Sarma. Spintronics: Fundamentals and applications. *Rev. Mod. Phys.*, 76(2):323, 2004.

[79] B. Bhushan. *Springer handbook of nanotechnology*, volume 2. Springer, 2007.

[80] M. Ciorga, A. S. Sachrajda, P. Hawrylak, C. Gould, P. Zawadzki, S. Jullian, Y. Feng, and Z. Wasilewski. Addition spectrum of a lateral dot from coulomb and spin-blockade spectroscopy. *Phys. Rev. B*, 61(24):R16315, 2000.

[81] J. M. Elzerman, R. Hanson, J. S. Greidanus, L. H. Willems Van Beveren, S. De Franceschi, L. M. K. Vandersypen, S. Tarucha, and L. P. Kouwenhoven. Few-electron quantum dot circuit with integrated charge read out. *Phys. Rev. B*, 67(16): 161308, 2003.

[82] M. T. Björk, C. Thelander, A. E. Hansen, L. E. Jensen, M. W. Larsson, L. R. Wallenberg, and L. Samuelson. Few-electron quantum dots in nanowires. *Nano Lett.*, 4 (9):1621–1625, 2004.

[83] A. Fuhrer, L. E. Fröberg, J. N. Pedersen, M. W. Larsson, A. Wacker, M.-E. Pistol, and L. Samuelson. Few electron double quantum dots in inas/inp nanowire heterostructures. *Nano Lett.*, 7(2):243–246, 2007.

[84] M. Nilsson, L. Namazi, S. Lehmann, M. Leijnse, K. A. Dick, and C. Thelander. Single-electron transport in InAs nanowire quantum dots formed by crystal phase engineering. *Phys. Rev. B*, 93(19):195422, 2016.

[85] D. Barker, S. Lehmann, L. Namazi, M. Nilsson, C. Thelander, K. A. Dick, and V. F. Maisi. Individually addressable double quantum dots formed with nanowire polytypes and identified by epitaxial markers. *Appl. Phys. Lett.*, 114(18):183502, 2019.

[86] C. Fasth, A. Fuhrer, M. T. Björk, and L. Samuelson. Tunable double quantum dots in InAs nanowires defined by local gate electrodes. *Nano Lett.*, 5(7):1487–1490, 2005.

[87] M. Fuechsle, J. A. Miwa, S. Mahapatra, H. Ryu, S. Lee, O. Warschkow, L. C. L. Hollenberg, G. Klimeck, and M. Y. Simmons. A single-atom transistor. *Nat. nanotechnol.*, 7(4):242–246, 2012.

[88] J. J. Pla, K. Y. Tan, J. P. Dehollain, W. H. Lim, J. J. L. Morton, D. N. Jamieson, A. S. Dzurak, and A. Morello. A single-atom electron spin qubit in silicon. *Nature*, 489 (7417):541–545, 2012.

[89] D. L. Klein, P. L. McEuen, J. E. B. Katari, R. Roth, and A. P. Alivisatos. An approach to electrical studies of single nanocrystals. *Appl. Phys. Lett.*, 68(18):2574–2576, 1996.

[90] M. Fricke, A. Lorke, J. P. Kotthaus, G. Medeiros-Ribeiro, and P. M. Petroff. Shell structure and electron-electron interaction in self-assembled InAs quantum dots. *Europhys. Lett.*, 36(3):197, 1996.

[91] Y. Kanai, R. S. Deacon, A. Oiwa, K. Yoshida, K. Shibata, K. Hirakawa, and S. Tarucha. Electrical control of Kondo effect and superconducting transport in a side-gated InAs quantum dot josephson junction. *Phys. Rev. B*, 82(5):054512, 2010.

[92] G. Katsaros, V. N. Golovach, P. Spathis, N. Ares, M. Stoffel, F. Fournel, O. G. Schmidt, L. I. Glazman, and S. De Franceschi. Observation of spin-selective tunneling in sige nanocrystals. *Phys. Rev. Lett.*, 107(24):246601, 2011.

[93] L. P. Kouwenhoven, D. G. Austing, and S. Tarucha. Few-electron quantum dots. *Rep. Prog. Phys.*, 64(6):701, 2001.

[94] J. Park, A. N. Pasupathy, J. I. Goldsmith, C. Chang, Y. Yaish, J. R. Petta, M. Rinkoski, J. P. Sethna, H. D. Abruña, P. L. McEuen, and D. C. Ralph. Coulomb blockade and the Kondo effect in single-atom transistors. *Nature*, 417(6890): 722–725, 2002.

[95] P. Gehring, J. M. Thijssen, and H. S. J. van der Zant. Single-molecule quantum-transport phenomena in break junctions. *Nat. Rev. Phys.*, 1(6):381–396, 2019.

[96] P. Gehring, J. K. Sowa, C. Hsu, J. de Bruijckere, M. van der Star, J. J. Le Roy, L. Bogani, E. M. Gauger, and H. S. J. van der Zant. Complete mapping of the thermoelectric properties of a single molecule. *Nat. Nanotechnol.*, 16(4):426–430, 2021.

[97] A. Fuhrer, M. Fuechsle, T. C. G. Reusch, B. Weber, and M. Y. Simmons. Atomic-scale, all epitaxial in-plane gated donor quantum dot in silicon. *Nano Lett.*, 9(2): 707–710, 2009.

[98] M. Fuechsle, S. Mahapatra, F. A. Zwanenburg, M. Friesen, M. A. Eriksson, and M. Y. Simmons. Spectroscopy of few-electron single-crystal silicon quantum dots. *Nat. Nanotechnol.*, 5(7):502–505, 2010.

[99] J. Salfi, S. Roddaro, D. Ercolani, L. Sorba, I. Savelyev, M. Blumin, H. E. Ruda, and F. Beltram. Electronic properties of quantum dot systems realized in semiconductor nanowires. *Semicond. Sci. Technol.*, 25(2):024007, 2010.

[100] F. A. Zwanenburg, A. S. Dzurak, A. Morello, M. Y. Simmons, L. C. L. Hollenberg, G. Klimeck, S. Rogge, S. N. Coppersmith, and M. A. Eriksson. Silicon quantum electronics. *Rev. Mod. Phys.*, 85(3):961, 2013.

[101] G. Scappucci, C. Kloeffel, F. A. Zwanenburg, D. Loss, M. Myronov, J.-J. Zhang, S. De Franceschi, G. Katsaros, and M. Veldhorst. The germanium quantum information route. *Nat. Rev. Mater.*, 6(10):926–943, 2021.

[102] L. Gaudreau, S. A. Studenikin, A. S. Sachrajda, P. Zawadzki, A. Kam, J. Lapointe, M. Korkusinski, and P. Hawrylak. Stability diagram of a few-electron triple dot. *Phys. Rev. Lett.*, 97(3):036807, 2006.

[103] F. N. M. Froning, M. K. Rehmann, J. Ridderbos, M. Brauns, F. A. Zwanenburg, A. Li, E. P. A. M. Bakkers, D. M. Zumbühl, and F. R. Braakman. Single, double, and triple quantum dots in ge/si nanowires. *Appl. Phys. Lett.*, 113(7):073102, 2018.

[104] H. Thierschmann, R. Sánchez, B. Sothmann, H. Buhmann, and L. W. Molenkamp. Thermoelectrics with coulomb-coupled quantum dots. *C. R. Phys.*, 17(10):1109–1122, 2016.

[105] A. W. Holleitner, C. R. Decker, H. Qin, K. Eberl, and R. H. Blick. Coherent coupling of two quantum dots embedded in an aharonov-bohm interferometer. *Phys. Rev. Lett.*, 87(25):256802, 2001.

[106] M. Nilsson, I. Chen, S. Lehmann, V. Maulerova, K. A. Dick, and C. Thelander. Parallel-coupled quantum dots in inas nanowires. *Nano Lett.*, 17(12):7847–7852, 2017.

[107] H. Bohuslavskyi, F. Ansaloni, A. Chatterjee, F. Fedele, T. Rasmussen, B. Brovang, J. Li, L. Hutin, B. Venitucci, B. Bertrand, M. Vinet, Y.-M. Niquet, and F. Kuemmeth. Reflectometry of charge transitions in a silicon quadruple dot. *arXiv preprint arXiv:2012.04791*, 2020.

[108] K. A. Dick. A review of nanowire growth promoted by alloys and non-alloying elements with emphasis on Au-assisted III–V nanowires. *Prog. Cryst. Growth Charact. Mater.*, 54(3-4):138–173, 2008.

[109] R. S. Wagner and W. C. Ellis. Vapor-liquid-solid mechanism of single crystal growth. *Appl. Phys. Lett.*, 4(5):89–90, 1964.

[110] P. Krogstrup, H. I. Jørgensen, E. Johnson, M. H. Madsen, C. B. Sørensen, A. F. i Morral, M. Aagesen, J. Nygård, and F. Glas. Advances in the theory of III–V nanowire growth dynamics. *J. Phys. D*, 46(31):313001, 2013.

[111] M. Hocevar, G. Immink, M. Verheijen, N. Akopian, V. Zwiller, L. P. Kouwenhoven, and E. Bakkers. Growth and optical properties of axial hybrid III–V/silicon nanowires. *Nat. commun.*, 3(1):1–6, 2012.

[112] M. T . Björk, B. J. Ohlsson, T. Sass, A. I. Persson, C. Thelander, M. H. Magnusson, K. Deppert, L. R. Wallenberg, and L. Samuelson. One-dimensional heterostructures in semiconductor nanowhiskers. *Appl. Phys. Lett.*, 80(6):1058–1060, 2002.

[113] V. Zannier, F. Rossi, D. Ercolani, and L. Sorba. Growth dynamics of InAs/InP nanowire heterostructures by au-assisted chemical beam epitaxy. *Nanotechnology*, 30 (9):094003, 2019.

[114] F. S. Thomas, A. Baumgartner, L. Gubser, C. Jünger, G. Fülöp, M. Nilsson, F. Rossi, V. Zannier, L. Sorba, and C. Schönenberger. Highly symmetric and tunable tunnel couplings in InAs/InP nanowire heterostructure quantum dots. *Nanotechnology*, 31 (13):135003, 2020.

[115] Z. Sadre Momtaz, S. Servino, V. Demontis, V. Zannier, D. Ercolani, F. Rossi, F. Rossella, L. Sorba, F. Beltram, and S. Roddaro. Orbital tuning of tunnel coupling in InAs/InP nanowire quantum dots. *Nano Lett.*, 20(3):1693–1699, 2020.

[116] M. J. Biercuk, S. Garaj, N. Mason, J. M. Chow, and C. M. Marcus. Gate-defined quantum dots on carbon nanotubes. *Nano Lett.*, 5(7):1267–1271, 2005.

[117] B. Ganjipour, H. A. Nilsson, B. Mattias B., L.-E. Wernersson, L. Samuelson, H. Q. Xu, and C. Thelander. GaSb nanowire single-hole transistor. *Appl. Phys. Lett.*, 99 (26):262104, 2011.

[118] K. Storm, G. Nylund, L. Samuelson, and A. P. Micolich. Realizing lateral wrap-gated nanowire FETs: controlling gate length with chemistry rather than lithography. *Nano Lett.*, 12(1):1–6, 2012.

[119] A. M. Burke, D. J. Carrad, J. G. Gluschke, K. Storm, S. Fahlvik Svensson, H. Linke, L. Samuelson, and A. P. Micolich. InAs nanowire transistors with multiple, independent wrap-gate segments. *Nano Lett.*, 15(5):2836–2843, 2015.

[120] J. G. Gluschke, J. Seidl, A. M. Burke, R. W. Lyttleton, D. J. Carrad, A. R. Ullah, S. Fahlvik, S. Lehmann, H. Linke, and A. P. Micolich. Achieving short high-quality gate-all-around structures for horizontal nanowire field-effect transistors. *Nanotechnology*, 30(6):064001, 2018.

[121] J. Gluschke, S. Svensson, and H. Thelander, C.and Linke. Fully tunable, non-invasive thermal biasing of gated nanostructures suitable for low-temperature studies. *Nanotechnology*, 25(38):385704, 2014.

[122] A. Svilans. *Thermoelectric experiments on nanowire-based quantum dots*. PhD thesis, Lund university, 2018.

[123] S. Svensson, A. I. Persson, E. A. Hoffmann, N. Nakpathomkun, H. A. Nilsson, H. Q. Xu, L. Samuelson, and H. Linke. Lineshape of the thermopower of quantum dots. *New J. Phys.*, 14(3):033041, 2012.

[124] S. Svensson, E. A. Hoffmann, N. Nakpathomkun, P. M. Wu, H. Q. Xu, H. A. Nilsson, D. Sánchez, V. Kashcheyevs, and H. Linke. Nonlinear thermovoltage and thermocurrent in quantum dots. *New J. Phys.*, 15(10):105011, 2013.

[125] J. P. Small, L. Shi, and P. Kim. Mesoscopic thermal and thermoelectric measurements of individual carbon nanotubes. *Solid State Commun.*, 127(2):181–186, 2003.

[126] S. Roddaro, D. Ercolani, M. A. Safeen, S. Suomalainen, F. Rossella, F. Giazotto, L. Sorba, and F. Beltram. Giant thermovoltage in single InAs nanowire field-effect transistors. *Nano Lett.*, 13(8):3638–3642, 2013.

[127] Z. Cui. *Nanofabrication: principles, capabilities and limits*. Springer, 2016.

[128] D. B. Suyatin, C. Thelander, M. T. Björk, I. Maximov, and L. Samuelson. Sulfur passivation for ohmic contact formation to InAs nanowires. *Nanotechnology*, 18(10): 105307, 2007.

[129] W. Lu, X. Zhao, D. Choi, S. El Kazzi, and J. A. del Alamo. Alcohol-based digital etch for III–V vertical nanowires with sub-10 nm diameter. *IEEE Electron Device Lett.*, 38(5):548–551, 2017.

[130] Z. Zhu, A. Jönsson, Y.-P. Liu, J. Svensson, R. Timm, and L.-E. Wernersson. Improved electrostatics through digital etch schemes in vertical GaSb nanowire p-MOSFETs on Si. *ACS Appl. Electron. Mater.*, 2022.

[131] A. Vogt, A. Simon, J. Weber, H. L. Hartnagel, J. Schikora, V. Buschmann, and H. Fuess. Non-annealed ohmic contacts to p-GaSb grown by molecular beam epitaxy. *Mater. Sci. Eng. B*, 66(1-3):199–202, 1999.

[132] T. F. Moerstedt. Fabrication and electrical characterization of GaSb p-type nanowire transistors, 2018.

[133] T. Gotow, S. Fujikawa, H. I. Fujishiro, M. Ogura, W. H. Chang, T. Yasuda, and T. Maeda. Surface cleaning and pure nitridation of GaSb by in-situ plasma processing. *AIP Adv.*, 7(10):105117, 2017.

[134] Ö. Gül, D. J. Van Woerkom, I. van Weperen, D. Car, S. R. Plissard, E. P. A. M. Bakkers, and L. P. Kouwenhoven. Towards high mobility InSb nanowire devices. *Nanotechnology*, 26(21):215202, 2015.

[135] G. Brassard, I. Chuang, S. Lloyd, and C. Monroe. Quantum computing. *Proc. Natl. Acad. Sci. USA*, 95(19):11032–11033, 1998.

[136] D. Deutsch. Quantum theory, the Church–Turing principle and the universal quantum computer. *Proc. R. Soc. London Ser. A*, 400(1818):97–117, 1985.

[137] D. P. DiVincenzo. Topics in quantum computers. In *Mesoscopic electron transport*, pages 657–677. Springer, 1997.

[138] A. Chatterjee, P. Stevenson, S. De Franceschi, A. Morello, N. P. de Leon, and F. Kuemmeth. Semiconductor qubits in practice. *Nat. Rev. Phys.*, 3(3):157–177, 2021.

[139] J. Gorman, D. G. Hasko, and D. A. Williams. Charge-qubit operation of an isolated double quantum dot. *Phys. Rev. Lett.*, 95(9):090502, 2005.

[140] J. M. Elzerman, R. Hanson, L. H. Willems van Beveren, B. Witkamp, L. M. K. Vandersypen, and L. P. Kouwenhoven. Single-shot read-out of an individual electron spin in a quantum dot. *Nature*, 430(6998):431–435, 2004.

[141] J. R. Petta, A. C. Johnson, J. M. Taylor, E. A. Laird, A. Yacoby, M. D. Lukin, C. M. Marcus, M. P. Hanson, and A. C. Gossard. Coherent manipulation of coupled electron spins in semiconductor quantum dots. *Science*, 309(5744):2180–2184, 2005.

[142] L. C. Camenzind, S. Geyer, A. Fuhrer, R. J. Warburton, D. M. Zumbühl, and A. V. Kuhlmann. A hole spin qubit in a fin field-effect transistor above 4 kelvin. *Nat. Electron.*, pages 1–6, 2022.

[143] G. Burkard, T. D. Ladd, J. M. Nichol, A. Pan, and J. R. Petta. Semiconductor spin qubits. *arXiv preprint arXiv:2112.08863*, 2021.

[144] K. C. Nowack, F. H. L. Koppens, Y. V. Nazarov, and L. M. K. Vandersypen. Coherent control of a single electron spin with electric fields. *Science*, 318(5855):1430–1433, 2007.

[145] S. Nadj-Perge, S. M. Frolov, E. P. A. M. Bakkers, and L. P. Kouwenhoven. Spin–orbit qubit in a semiconductor nanowire. *Nature*, 468(7327):1084–1087, 2010.

[146] F. H. L. Koppens, C. Buizert, K. Tielrooij, I. T. Vink, K. C. Nowack, T. Meunier, L. P. Kouwenhoven, and L. M. K. Vandersypen. Driven coherent oscillations of a single electron spin in a quantum dot. *Nature*, 442(7104):766–771, 2006.

[147] E. I. Rashba and A. L. Efros. Orbital mechanisms of electron-spin manipulation by an electric field. *Phys. Rev. Lett.*, 91(12):126405, 2003.

[148] C. Flindt, A. S. Sørensen, and K. Flensberg. Spin-orbit mediated control of spin qubits. *Phys. Rev. Lett.*, 97(24):240501, 2006.

[149] Y. Tokura, W. G. van der Wiel, T. Obata, and S. Tarucha. Coherent single electron spin control in a slanting Zeeman field. *Phys. Rev. Lett.*, 96(4):047202, 2006.

[150] J. Danon. Spin-flip phonon-mediated charge relaxation in double quantum dots. *Phys. Rev. B*, 88(7):075306, 2013.

[151] G. Burkard, D. Loss, and D. P. DiVincenzo. Coupled quantum dots as quantum gates. *Phys. Rev. B*, 59(3):2070, 1999.

[152] M. H. Kolodrubetz and J. R. Petta. Coherent holes in a semiconductor quantum dot. *Science*, 325(5936):42–43, 2009.

[153] J. W. G. Van den Berg, S. Nadj-Perge, V. S. Pribiag, S. R. Plissard, E. P. A. M. Bakkers, S. M. Frolov, and L. P. Kouwenhoven. Fast spin-orbit qubit in an indium antimonide nanowire. *Phys. Rev. Lett.*, 110(6):066806, 2013.

[154] S. Csonka, L. Hofstetter, F. Freitag, S. Oberholzer, C. Schonenberger, T. S. Jespersen, M. Aagesen, and J. Nygård. Giant fluctuations and gate control of the g-factor in InAs nanowire quantum dots. *Nano Lett.*, 8(11):3932–3935, 2008.

[155] H. A. Nilsson, P. Caroff, C. Thelander, M. Larsson, J. B. Wagner, L.-E. Wernersson, L. Samuelson, and H. Q. Xu. Giant, level-dependent g factors in InSb nanowire quantum dots. *Nano Lett.*, 9(9):3151–3156, 2009.

[156] S. Nadj-Perge, V. S. Pribiag, J. W. G. Van den Berg, K. Zuo, S. R. Plissard, E. P. A. M. Bakkers, S. M. Frolov, and L. P. Kouwenhoven. Spectroscopy of spin-orbit quantum bits in indium antimonide nanowires. *Phys. Rev. Lett.*, 108(16):166801, 2012.

[157] J. Wang, G. Huang, S. Huang, J. Xue, D. Pan, J. Zhao, and H. Xu. Anisotropic Pauli spin-blockade effect and spin–orbit interaction field in an InAs nanowire double quantum dot. *Nano Lett.*, 18(8):4741–4747, 2018.

[158] T. Campos, P. E. F. Junior, M. Gmitra, G. M. Sipahi, and J. Fabian. Spin-orbit coupling effects in zinc-blende InSb and wurtzite InAs nanowires: Realistic calculations with multiband k· p method. *Phys. Rev. B*, 97(24):245402, 2018.

[159] S. Roddaro, A. Pescaglini, D. Ercolani, L. Sorba, and F. Beltram. Manipulation of electron orbitals in hard-wall InAs/InP nanowire quantum dots. *Nano Lett.*, 11(4): 1695–1699, 2011.

[160] S. Dorsch, B. Dalelkhan, S. Fahlvik, and A. M. Burke. Side-gated, enhancement mode, InAs nanowire double quantum dot devices—toward controlling transverse electric fields in spin-transport measurements. *Nanotechnology*, 30(14):144002, 2019.

[161] L. Han, M. Chan, D. de Jong, C. Prosko, G. Badawy, S. Gazibegovic, E. P. A. M. Bakkers, L. P. Kouwenhoven, F. K. Malinowski, and W. Pfaff. Variable and orbital-dependent spin-orbit field orientations in a InSb double quantum dot characterized via dispersive gate sensing. *arXiv preprint arXiv:2203.06047*, 2022.

[162] V. S. Pribiag, S. Nadj-Perge, S. M. Frolov, J. W. G. Van Den Berg, I. Van Weperen, S. R. Plissard, E. P. A. M. Bakkers, and L. P. Kouwenhoven. Electrical control of single hole spins in nanowire quantum dots. *Nature Nanotechnol.*, 8(3):170–174, 2013.

[163] M. Jeppsson, K. A. Dick, J. B. Wagner, P. Caroff, K. Deppert, L. Samuelson, and L.-E. Wernersson. GaAs/GaSb nanowire heterostructures grown by MOVPE. *J. Cryst. Growth*, 310(18):4115–4121, 2008.

[164] J. Sun, M. Peng, Y. Zhang, L. Zhang, R. Peng, C. Miao, D. Liu, M. Han, R. Feng, Y. Ma, Y. Dai, L. He, C. Shan, A. Pan, W. Hu, and Z. Yang. Ultrahigh hole mobility of sn-catalyzed GaSb nanowires for high speed infrared photodetectors. *Nano Lett.*, 19(9):5920–5929, 2019.

[165] M. Karalic, C. Mittag, M. Hug, T. Tschirky, W. Wegscheider, K. Ensslin, T. Ihn, K. Shibata, and R. Winkler. Gate-tunable electronic transport in p-type GaSb quantum wells. *Phys. Rev. B*, 99(11):115435, 2019.

[166] B. Ganjipour, M. Leijnse, L. Samuelson, H. Q. Xu, and C. Thelander. Transport studies of electron-hole and spin-orbit interaction in GaSb/InAsSb core-shell nanowire quantum dots. *Phys. Rev. B*, 91(16):161301, 2015.

[167] B. Ganjipour, M. Ek, M. Borg, K. A. Dick, M.-E. Pistol, L.-E. Wernersson, and C. Thelander. Carrier control and transport modulation in GaSb/InAsSb core/shell nanowires. *Appl. Phys. Lett.*, 101(10):103501, 2012.

[168] J. Schuff, D. T. Lennon, S. Geyer, D. L. Craig, F. Fedele, F. Vigneau, L. C. Camenzind, A. V. Kuhlmann, G. A. D. Briggs, D. M. Zumbühl, D. Sejdinovic, and N. Ares. Identifying Pauli spin blockade using deep learning. *arXiv preprint arXiv:2202.00574*, 2022.

[169] F. H. L. Koppens, J. A. Folk, J. M. Elzerman, R. Hanson, L. H. W. Van Beveren, I. T. Vink, H.-P. Tranitz, W. Wegscheider, L. P. Kouwenhoven, and L. M. K. Vandersypen. Control and detection of singlet-triplet mixing in a random nuclear field. *Science*, 309(5739):1346–1350, 2005.

[170] M. Brauns, J. Ridderbos, A. Li, E. P. A. M. Bakkers, W. G. Van Der Wiel, and F. A. Zwanenburg. Anisotropic pauli spin blockade in hole quantum dots. *Phys. Rev. B*, 94(4):041411, 2016.

[171] R. Maurand, X. Jehl, D. Kotekar-Patil, A. Corna, H. Bohuslavskyi, R. Laviéville, L. Hutin, S. Barraud, M. Vinet, M. Sanquer, and S. De Franceschi. A CMOS silicon spin qubit. *Nat. Commun.*, 7(1):1–6, 2016.

[172] F. N. M. Froning, L. C. Camenzind, O. A. H. van der Molen, A. Li, E. P. A. M. Bakkers, D. M. Zumbühl, and F. R. Braakman. Ultrafast hole spin qubit with gate-tunable spin–orbit switch functionality. *Nat. Nanotechnol.*, 16(3):308–312, 2021.

[173] F. J. DiSalvo. Thermoelectric cooling and power generation. *Science*, 285(5428):703–706, 1999.

[174] J. P. Heremans, M. S. Dresselhaus, L. E. Bell, and D. T. Morelli. When thermoelectrics reached the nanoscale. *Nat. Nanotechnol.*, 8(7):471–473, 2013.

[175] G. Benenti, G. Casati, K. Saito, and R. S. Whitney. Fundamental aspects of steady-state conversion of heat to work at the nanoscale. *Phys. Rep.*, 694:1–124, 2017.

[176] S. Datta. *Electronic transport in mesoscopic systems*. Cambridge university press, 1997.

[177] M. Josefsson. *Quantum-dot heat engines*. PhD thesis, Lund University, 2020.

[178] H. S. Kim, W. Liu, G. Chen, C. Chu, and Z. Ren. Relationship between thermoelectric figure of merit and energy conversion efficiency. *Proc. Natl. Acad. Sci. U.S.A.*, 112(27):8205–8210, 2015.

[179] B. Muralidharan and M. Grifoni. Performance analysis of an interacting quantum dot thermoelectric setup. *Phys. Rev. B*, 85(15):155423, 2012.

[180] S. Fahlvik Svensson. *Thermoelectric Phenomena in Quantum Dots*. PhD thesis, Lund University, 2014.

[181] G. Wiedemann and R. Franz. Ueber die Waerme-Leitungsfähigkeit der Metalle. *Ann. Physik*, 89(2):497–531, 1853.

[182] L. D. Hicks and M. S. Dresselhaus. Effect of quantum-well structures on the thermoelectric figure of merit. *Phys. Rev. B*, 47(19):12727, 1993.

[183] L. D. Hicks and M. S. Dresselhaus. Thermoelectric figure of merit of a one-dimensional conductor. *Phys. Rev. B*, 47(24):16631, 1993.

[184] M. G. Vavilov and A. D. Stone. Failure of the Wiedemann-Franz law in mesoscopic conductors. *Phys. Rev. B*, 72(20):205107, 2005.

[185] J. Fast, U. Aeberhard, S. P. Bremner, and H. Linke. Hot-carrier optoelectronic devices based on semiconductor nanowires. *Appl. Phys. Rev.*, 8(2):021309, 2021.

[186] A. I. Boukai, Y. Bunimovich, J. Tahir-Kheli, J. Yu, W. A. Goddard Iii, and J. R. Heath. Silicon nanowires as efficient thermoelectric materials. *Nature*, 451(7175): 168–171, 2008.

[187] A. Ali, Y. Chen, V. Vasiraju, and S. Vaddiraju. Nanowire-based thermoelectrics. *Nanotechnology*, 28(28):282001, 2017.

[188] G. D. Mahan and J. O. Sofo. The best thermoelectric. *Proc. Natl. Acad. Sci.*, 93(15): 7436–7439, 1996.

[189] T. E. Humphrey, R. Newbury, R. P. Taylor, and H. Linke. Reversible quantum brownian heat engines for electrons. *Physical review letters*, 89(11):116801, 2002.

[190] T. E. Humphrey and H. Linke. Reversible thermoelectric nanomaterials. *Phys. Rev. Lett.*, 94:096601, 2005.

[191] A. Svilans, M. Leijnse, and H. Linke. Experiments on the thermoelectric properties of quantum dots. *C. R. Phys.*, 17(10):1096–1108, 2016.

[192] D. Prete, P. A. Erdman, V. Demontis, V. Zannier, D. Ercolani, L. Sorba, F. Beltram, F. Rossella, F. Taddei, and S. Roddaro. Thermoelectric conversion at 30 k in inas/inp nanowire quantum dots. *Nano Lett.*, 19(5):3033–3039, 2019.

[193] T. E. Humphrey. *Mesoscopic Quantum Ratchets and the Thermodynamics of Energy Selective Electron Heat Engines*. PhD thesis, University of New South Wales, 2003.

[194] B. Roche, P. Roulleau, T. Jullien, Y. Jompol, I. Farrer, D. A. Ritchie, and D. C. Glattli. Harvesting dissipated energy with a mesoscopic ratchet. *Nat. Commun.*, 6 (1):1–5, 2015.

[195] H. Thierschmann, R. Sánchez, B. Sothmann, F. Arnold, C. Heyn, W. Hansen, H. Buhmann, and L. W. Molenkamp. Three-terminal energy harvester with coupled quantum dots. *Nat. Nanotechnol.*, 10(10):854–858, 2015.

[196] F. Hartmann, P. Pfeffer, S. Höfling, M. Kamp, and L. Worschech. Voltage fluctuation to current converter with coulomb-coupled quantum dots. *Phys. Rev. Lett.*, 114(14): 146805, 2015.

[197] G. Jaliel, R. K. Puddy, R. Sánchez, A. N. Jordan, B. Sothmann, I. Farrer, J. P. Griffiths, D. A. Ritchie, and C. G. Smith. Experimental realization of a quantum dot energy harvester. *Phys. Rev. Lett.*, 123(11):117701, 2019.

[198] A. N. Jordan, B. Sothmann, R. Sánchez, and M. Büttiker. Powerful and efficient energy harvester with resonant-tunneling quantum dots. *Phys. Rev. B*, 87(7):075312, 2013.

[199] S. Willing, H. Lehmann, M. Volkmann, and C. Klinke. Metal nanoparticle film–based room temperature coulomb transistor. *Sci. Adv.*, 3(7):e1603191, 2017.

[200] B. Dutta, D. Majidi, N. W. Talarico, N. L. Gullo, H. Courtois, and C. B. Winkelmann. Single-quantum-dot heat valve. *Physical Review Letters*, 125(23):237701, 2020.

[201] G. Verley, M. Esposito, T. Willaert, and C. Van den Broeck. The unlikely Carnot efficiency. *Nat. Commun.*, 5(1):1–5, 2014.

[202] F. Brange. *Quantum Correlations and Temperature Fluctuations in Nanoscale Systems*. PhD thesis, Lund University, 2019.

[203] B. K. Agarwalla and D. Segal. Assessing the validity of the thermodynamic uncertainty relation in quantum systems. *Phys. Rev. B*, 98(15):155438, 2018.

[204] P. Pietzonka and U. Seifert. Universal trade-off between power, efficiency, and constancy in steady-state heat engines. *Phys. Rev. Lett.*, 120:190602, 2018.

[205] M. L. Bera, S. Julià-Farré, M. Lewenstein, and M. N. Bera. Quantum heat engines with Carnot efficiency at maximum power. *Phys. Rev. Res.*, 4(1):013157, 2022.

[206] S. Saryal, M. Gerry, I. Khait, D. Segal, and B. K. Agarwalla. Universal bounds on fluctuations in continuous thermal machines. *Phys. Rev. Lett.*, 127(19):190603, 2021.

[207] J.-H. Jiang, O. Entin-Wohlman, and Y. Imry. Thermoelectric three-terminal hopping transport through one-dimensional nanosystems. *Phys. Rev. B*, 85(7):075412, 2012.

[208] J.-H. Jiang, O. Entin-Wohlman, and Y. Imry. Three-terminal semiconductor junction thermoelectric devices: improving performance. *New J. Phys.*, 15(7):075021, 2013.

[209] J.-H. Jiang. Enhancing efficiency and power of quantum-dots resonant tunneling thermoelectrics in three-terminal geometry by cooperative effects. *J. Appl. Phys.*, 116 (19):194303, 2014.

[210] R. Bosisio, G. Fleury, J.-L. Pichard, and C. Gorini. Nanowire-based thermoelectric ratchet in the hopping regime. *Phys. Rev. B*, 93(16):165404, 2016.

[211] J.-H. Jiang, M. Kulkarni, D. Segal, and Y. Imry. Phonon thermoelectric transistors and rectifiers. *Phys. Rev. B*, 92(4):045309, 2015.

[212] J. Liu and D. Segal. Thermodynamic uncertainty relation in quantum thermoelectric junctions. *Phys. Rev. E*, 99(6):062141, 2019.

[213] H. Thierschmann, M. Henke, J. Knorr, L. Maier, C. Heyn, W. Hansen, H. Buhmann, and L. W. Molenkamp. Diffusion thermopower of a serial double quantum dot. *New J. Phys.*, 15(12):123010, 2013.

[214] V. S. Khrapai, S. Ludwig, J. P. Kotthaus, H.-P. Tranitz, and W. Wegscheider. Double-dot quantum ratchet driven by an independently biased quantum point contact. *Phys. Rev. Lett.*, 97(17):176803, 2006.

[215] V. S. Khrapai, S. Ludwig, J. P. Kotthaus, H.-P. Tranitz, and W. Wegscheider. Nonequilibrium interactions between two quantum circuits. *J. Phys. Condens. Matter.*, 20(45):454205, 2008.

[216] V. S. Khrapai, S. Ludwig, J. P. Kotthaus, H.-P. Tranitz, and W. Wegscheider. Nonequilibrium phenomena in adjacent electrically isolated nanostructures. *Physica E Low. Dimens. Syst. Nanostruct.*, 40(5):995–998, 2008.

[217] G. Granger, D. Taubert, C. E. Young, L. Gaudreau, A. Kam, S. A. Studenikin, P. Zawadzki, D. Harbusch, D. Schuh, W. Wegscheider, Z. R. Wasilewski, A. A. Clerk,

S. Ludwig, and A. S. Sachrajda. Quantum interference and phonon-mediated back-action in lateral quantum-dot circuits. *Nat. Phys.*, 8(7):522–527, 2012.

[218] A. Donarini, M. Niklas, M. Schafberger, N. Paradiso, C. Strunk, and M. Grifoni. Coherent population trapping by dark state formation in a carbon nanotube quantum dot. *Nat. Commun.*, 10(1):1–8, 2019.

[219] A. A. Clerk, M. H. Devoret, S. M. Girvin, F. Marquardt, and R. J. Schoelkopf. Introduction to quantum noise, measurement, and amplification. *Rev. Mod. Phys.*, 82(2):1155, 2010.

[220] Y. Kim and H. Song. Noise spectroscopy of molecular electronic junctions. *Appl. Phys. Rev.*, 8(1):011303, 2021.

[221] N. Nakpathomkun, H. Q. Xu, and H. Linke. Thermoelectric efficiency at maximum power in low-dimensional systems. *Phys. Rev. B*, 82(23):235428, 2010.

Appendix

The appendix to this thesis is only available in digital form and can be accessed at
https://github.com/SvenDorsch/PhD-thesis-appendix
or by scanning the QR code below:

The appendix contains details of device fabrication and the QmeQ setup for all simulations shown in this thesis. Further additions, such as data analysis functions and details, may be provided in the future.

Scientific publications

Printed by Media-Tryck, Lund 2022 NORDIC SWAN ECOLABEL 3041 0903

LUND
UNIVERSITY

Division of Solid State Physics
Department of Physics
Faculty of Engineering
Lund University

ISBN 978-91-8039-197-9

9 789180 391979